An in-cell integrated system for the real-time monitoring of Lithium-ion battery cells

Von der Fakultät Informatik, Elektrotechnik und Informationstechnik der Universität Stuttgart zur Erlangung der Würde eines Doktor-Ingenieurs (Dr.-Ing.) genehmigte Abhandlung

Vorgelegt von:
Fida Saidani, M.Sc.
aus Bizerte, Tunesien

Hauptberichter: Prof. Dr.-Ing. Joachim Burghartz
Mitberichter: Prof. Dr.-Ing. Kai Peter Birke
Tag der mündlichen Prüfung: 14.10.2021

Institut für Mikroelektronik Stuttgart (IMS CHIPS)
Universität Stuttgart
2021

Fida Saidani
An in-cell integrated system for the real-time monitoring of Lithium-ion battery cells
Institut für Mikroelektronik Stuttgart (IMS CHIPS)
Universität Stuttgart
2021

Abstract

The Lithium-ion battery technology has been dominating the Electric Vehicles market thanks to its high energy density, its compactness, and its long-time cycle stability. However, the quality of the cells is sensitive to the statistical variations of the manufacturing process parameters. Important discrepancies in capacities as well as different resilience levels to risky situations and possible abuse scenarios are seen between theoretically identical cells. This compromises the safety of the system and, consequently, of the user during the operational lifetime of the battery.

This work attempts to address this issue on cell level and to enhance the State-of-the-Art intrinsic safety of Lithium-ion battery cells by integrating a monitoring circuit inside every battery cell. This Cell Supervisory Circuit (CSC) is a compact system containing sensor elements (voltage and temperature), local memory blocks, a microcontroller, and an optical communication interface. It communicates with the Battery Management System, sends real-time measurement data and answers to inquiries. A successful proof-of-concept for a system, which contains the mentioned components and performs the described tasks, is presented.

The mechanical feasibility and the integration of the circuit inside the cells is tested and proved. Cell-internal data were successfully measured and saved during the manufacturing phase, and extracted during the operational life phase.

Moreover, several improvements towards the complete integration of the CSC on a thin and flexible monolithic solution (electronic chip) are proposed and tested. A Bandgap temperature sensor is designed and tested as an alternative to the temperature measuring resistors. In addition, a sensor of the battery cell internal resistance is implemented and tested to evaluate the State of Health of the cell. Last, the chemical compatibility of a packaging solution of thin electronic chips with the battery electrolyte is tested. A packaging process version showing a good resilience with the used electrolyte is presented.

Kurzfassung

Die Lithium-Ionen Batterietechnologie dominiert heutzutage den Markt aufgrund ihrer hohen Energiedichte, ihrer Kompaktheit und ihrer hohen Zyklenfestigkeit. Die Qualität der Zellen ist jedoch empfindlich gegenüber statistischen Variationen der Herstellungsprozessparameter. Es werden zwischen theoretisch identisch hergestellten Zellen wichtige Diskrepanzen in der nutzbaren Zellkapazitäten festgestellt, sowie unterschiedliche Resilienzen in Risikosituationen und möglichen Missbrauchsszenarien. Dies kann die Sicherheit des Systems und, folglich, des Benutzers während der aktiven Lebensdauer der Batterie gefährden.

Die vorliegende Arbeit geht diese Thematik auf Zellebene an. Der Stand der Technik der Eigensicherheit von Zellen wird weiterentwickelt, indem in jede Zelle eine Überwachungsschaltung integriert wird. Diese Zellenüberwachungsschaltung (in Englisch Cell Supervisory Circuit, CSC) ist ein kompaktes System, das Sensorelemente (für Zellspannung und Temperatur), lokale Speicherelemente, einen Mikrocontroller und eine optische Kommunikationsschnittstelle beinhaltet. Die Schaltung kommuniziert mit dem Batteriemanagementsystem, sendet Echtzeitmessdaten und beantwortet Anfragen. Es wird ein erfolgreicher Demonstrator für ein System vorgestellt, der die genannten Komponenten enthält und die beschriebenen Aufgaben ausführt.

Die mechanische Machbarkeit und die Integration der Schaltung in die Zellen wurden getestet und bewiesen. Zellinterne Daten wurden während der Herstellungsphase erfolgreich gemessen und gespeichert, und im Nachhinein durch die Kommunikationsschnittstelle während der Betriebslebensdauer extrahiert.

Darüber hinaus wurden verschiedene Verbesserungsmöglichkeiten hinsichtlich der vollständigen Integration der Schaltung in eine dünne und flexible monolithische Lösung (einen elektronischen Chip) vorgeschlagen. Als Alternative zu den Temperaturmesswiderständen wurde ein Bandgap-Temperatursensor entwickelt und getestet. Zusätzlich wurde ein Sensor für den Innenwiderstand der Batteriezelle implementiert und getestet, um den Gesundheitszustand der Zelle (in Englisch State of Health, SoH) zu bewerten. Zuletzt wurde die chemische Verträglichkeit einer Packaging-Lösung aus dünnen elektronischen Chips auf Beständigkeit mit dem Batterieelektrolyten getestet.

Table of Contents

List of Figures

List of Tables

Glossary

Acronyms

2-polymer Two-polymer.

AC Alternating Current.

ADC Analog-to-digital Converter.

AN Analog channel.

BCB Benzocyclobutene.

BEV Battery Electric Vehicle.

BG Bandgap.

BiCMOS Bipolar Complementary Metal-Oxide-Semiconductor.

BJT Bipolar Junction Transistor.

BMS Battery Management System.

BoL Begin of Life.

CAN Controller Area Network.

CC Constant Current.

CDIP Ceramic Dual in-Line Package.

CFP Chip Film Patch.

CMOS Complementary Metal-Oxide-Semiconductor.

CoB Chip on Board.

CSC Cell Supervisory Circuit.

CTAT Complementary to Absolute Temperature.

CTE Coefficient of Thermal Expansion.

CV Constant Voltage.

DC Direct Current.

DCR Direct Current Resistance.

DD Data Direction.

DEC Diethyl carbonate.

DIN Deutsches Institut für Normung, in English, the German Institute for Standardization.

DIP Dual in-Line Package.

DMC Dimethyl Carbonate.

DMM digital multimeter.

DoD Depth of Discharge.

DUT Device Under Test.

EC Ethylene Carbonate.

EEPROM Electrically Erasable Programmable Read-Only Memory.

EIS Electroimpedance Spectroscopy.

EMC Ethyl Methyl Carbonate.

EN European Norm.

ENDEC Encoder/Decoder.

ENEPIG Electroless Nickel Electroless Palladium Immersion Gold.

EUCAR European Council for Automotive R&D.

EV Electric Vehicle.

FoM Figure of Merit.

FSM Finite-state machine.

GUI Graphical User Interface.

HASL Hot Air Solder Leveling.

HEV Hybrid Electric Vehicle.

HF Hydrogen fluoride.

HPPC Hybrid pulse power characterization.

HT high temperature.

HV high voltage.

I2C Inter-Integrated Circuit.

IEC International Electrotechnical Commission.

IMS Institut für Mikroelektronik Stuttgart.

IntLiIon Intelligent Data Bus Concepts for Lithium-Ion Batteries in Electric and Hybrid Vehicles.

IPV Institute for Photovoltaics.

IR Infrared.

IrDA Infrared Data Association.

ISO International Organization for Standardization.

LabVIEW Laboratory Virtual Instrument Engineering Workbench.

LAN Local Area Network.

LCD Liquid-Crystal Display.

LED Light-emitting diode.

LiB Lithium-ion battery.

LiC Lithium-ion cell.

low-CTE low-Coefficient of Thermal Expansion.

LSB Least Significant Bit.

LTI Linear time-invariant.

MC Monte-Carlo.

MCC MPLAB® Code Configurator.

MOS Metal-Oxide-Semiconductor.

MOSFET Metal-Oxide-Semiconductor Field-Effect Transistor.

N-MOSFET n-type MOSFET.

NI National Instruments.

NPE National Platform for Electric Mobility.

OCV Open Circuit Voltage.

OEM Original Equipment Manufacturer.

Op-Amp operational amplifier.

OPA oriented Polyamid.

OTS Off-the-Shelf.

P-MOSFET p-type MOSFET.

PCB Printed Circuit Board.

PDK Process Design Kit.

PE Polyethylene.

PEV Plug-in Electric Vehicle.

PHEV Plug-in Hybrid Electric Vehicle.

PI Polyimide.

PIN Positive Intrinsic Negative.

PMOS p-type Metal-Oxide-Semiconductor.

PP Polypropylene.

PTAT Proportional to Absolute Temperature.

PTFE Polytetrafluoroethylene.

PU Polyurethane.

PVDF Polyvinylidene Difluoride.

R&D Research and Development.

Redox Oxidation-Reduction.

REEV Range Extended Electric Vehicle.

RTCC Real-Time Clock and Calendar.

SCB Slave Circuit Board.

SCL Serial Clock.

SDA Serial Data.

SEI Solid Electrolyte Interface.

SHE Standard Hydrogen Electrode.

SIR Serial Infrared.

Smart-LiB Smart-Lithium-ion battery.

SMART-LIC Smart and Compact Battery Management System Module for Integration into Lithium-Ion Cell for Fully Electric Vehicles.

SMD Surface-mounted device.

SoA State-of-the-Art.

SoC State of Charge.

SoF State of Function.

SoH State of Health.

TC Temperature Coefficient.

UART Universal Asynchronous Receiver-Transmitter.

USB	Universal Serial Bus.
VBA	Visual Basic for Applications.
VDA	Verband der Automobilindustrie.
XH018	X-FAB 0.18 Micron Modular HT HV CMOS Technology.
ZIF	Zero Insertion Force.
ZSW-BW	Zentrum für Sonnenenergie- und Wasserstoff-Forschung Baden-Württemberg.

Terminology

Battery is an arrangement of several battery cells in series and/or in parallel, together with a management system as found in Electric Vehicles (Section 2.3) [11].

Battery cell Although sometimes used interchangeably in the literature, this work differentiates between the cell (also called monocell or battery cell), which is a single electrochemical device with a nominal voltage between 2.2 and 4.2 V for currently available Lithium-ion battery technologies (as described in Section 2.1), and the battery as a complete system of several cells and other components (as described in Section. 2.3) [11].

C-ratio is defined as the current intensity obtained by dividing the rated capacity by 1 h. For a cell with a given capacity of 20 A h, the C-ratio is $1\,\mathrm{C} = 20\,\mathrm{A\,h}/1\,\mathrm{h} = 20\,\mathrm{A}$ [97].

Capacity The (rated) capacity is the theoretical quantity of the electric charge which can be accumulated during the charge, stored during the open circuit stay, and released during the discharge until a given cut-off voltage in a reversible manner. It is generally expressed in mA h or in A h [70, 125].

Capacity fade is the decrease of the effective capacity compared to the nominal capacity value, mainly due to aging.

CC-CV The CC-CV is a battery cell charging technique which applies a medium accuracy Constant Current (CC) of several mA to the cell until it reaches a previously set voltage value, then transitions to applying a high accuracy Constant Voltage (CV). The current in the CV phase then decreases gradually. The cell is considered fully charged when the current in the CV phase reaches a given low percentage of its initial value during the CC phase (typically 1%) [118, 119].

Coulombic efficiency also faradaic efficiency, is the efficiency with which a given system transports charge.

Cycle stability is the number of cycles that a battery can endure without showing capacity fading and/or other signs of aging.

Electric vehicle The Electric Vehicle (EV) is a umbrella term that is used interchangeably and in different ways in the literature to describe either Battery Electric Vehicles, not including Plug-in Hybrid Electric Vehicles, or Plug-in Electric Vehicles, including Plug-in Hybrid Electric Vehicles [126].

It can also be used for the combination of Battery Electric Vehicles and Range Extended Electric Vehicles, sometimes even wrongly for the combination of Plug-in

Electric Vehicles and Hybrid Electric Vehicles.

In this work, the term Electric Vehicle is used to describe purely Battery Electric Vehicles. Hybrid Electric Vehicles are mentioned separately and include Plug-in Hybrid Electric Vehicles.

Energy density or volumetric energy density, is a measure of the energy stored in a battery per unit volume and is expressed in Wh/l [5, 118].

Nominal voltage is the characteristic operating voltage of the battery cell specified by the manufacturer.

Power density is the amount of power (time rate of energy flow) per unit volume deliverable by the battery and is expressed in W/l.

Primary cell is a non-rechargeable battery technology.

Secondary cell (also accumulator) is a rechargeable battery technology.

Specific energy or gravimetric energy density, is a measure of the energy stored in a battery per unit mass and is expressed in Wh/kg. It practically defines the weight of a battery [5, 118].

Specific power or gravimetric power density, also power-to-weight-ration, indicates the loading capability of a battery and is expressed in W/kg.

Symbols

$\kappa_{\mathbf{B}}$ is the Boltzmann constant, with κ_{B}=1.380649×10^{-23}J/K.

σ is the standard deviation, a measure for the dispersion of a given set of values from the mean or the expected value.

q is the elementary charge, q=1.602176634×10^{-19}C.

Chapter 1

Introduction

1.1 Motivation

1.1.1 Energy storage technologies

The needs for energy, energy storage and energy transport solutions are as old as humanity. Historically, fossil resources served as energy storage devices. By changing to other (e.g. renewable) electrical energy sources, the storing of the generated electrical energy has become an economical and technical challenge. Therefore, a large pallet of storage technologies has been researched and developed. Depending on the application and operational area, these technologies have a big market share.

Research to push the limits of current technologies towards further optimization or radical redesigns is on-going but limited by the material chemical properties and the laws of physics [1, 2].

Table 1.1 [1, 3] presents an overview of commonly used storage devices, organized according to their power and energy capabilities, the storage time duration and application areas.

Table 1.2 [1, 3] shows the color legend of Table 1.1 and, thereby, offers an alternative differentiation according to the physical form of the energy storage.

One important form is the electrochemical storage. An overview of electrochemical storage techniques is given in Table 1.3 [1, 4].

Secondary (or rechargeable) batteries, (opposed to primary or non-rechargeable batteries) are very common, well-established, and highly efficient electrochemical energy storage solutions [1]. Since battery technology research must address several, sometimes conflicting requirements, i.e. offering a high power as well as high energy density, and simultaneously guaranteeing a high robustness level, a high cycle stability (slow aging) as well as low cost, several technologies were developed. Table 1.4 [5] presents a comparison of the

Table 1.1: Overview of energy storage techniques [1, 3]

Requirements	← High power				High energy →
Storage time duration	Seconds		Minutes	Hours/days	
Application examples	- harmonic (flicker) compensation - voltage stabilization - frequency stabilization		- black start capacity - Uninterruptible power supply - mild hybrid systems	- Microgrid - electricity trading - load spikes smoothing - load balancing - purely battery powered vehicles	
Technology	Thermal energy storage	short-time storage	Local small accumulator	Decentralized large battery	Central Storage (reservoir) power station
Storage concept	Steam reservoir	Capacitors /super capacitors	Lead–acid battery	Lead–acid battery	pumped hydroelectric energy storage
	thermal oil	Superconducting Magnetic Energy	Lithium-ion battery	Lithium-ion battery	Compressed air energy storage
	Molten-salt technology	Flywheel	Nickel–cadmium battery	Sodium–sulfur battery	
	Phase-change storage		Nickel–metal hydride battery	redox flow battery	

Table 1.2: Color legend/ alternative classification for physical forms of energy storage [1, 3]

Color	**Storage type**	**Physical form**
🟦	Thermal storage	virtual
🟥	Electrical storage	electromagnetic fields or static electrical fields
🟩	Electrochemical storage	chemical energy
🟨	Mechanical storage	kinetic or potential energy

Table 1.3: Overview of electrochemical energy storage devices [1, 4]

Storage device	**Examples**
Molten-salt battery (also High temperature battery or thermal battery)	NaS, NaNiCl
Secondary cell (opposed to primary cell)	Li-ion, NiMH, NiCd, Lead–acid
Flow and gas battery	redox flow battery , Metal–air cells

characteristics of commonly used secondary (rechargeable) batteries.

As can be seen from Table 1.4, the Lithium-ion battery (LiB) technology stands out especially due to its low discharge rate, its high coulombic efficiency (efficiency of charge transfer) and its high cycle stability (low capacity fading throughout the charging and discharging cycles, i.e. slow aging).

The choice of the secondary battery technology to be used depends on the different applications and the diverse requirements they set besides the electrical performance. Whether the application is stationary or mobile, the weight factor can be relevant. If a direct tangency between a human user and the battery is expected, the risks related to the battery failure or abuse scenarios set higher safety requirements [1]. These requirements are becoming increasingly relevant with the rise of demand on the electrification of transport systems as will be presented in the next section (Section 1.1.2). This safety aspect is especially challenging with the LiB technology, as will be explained in Section 1.1.3.

Table 1.4: Characteristics of commonly used secondary batteries [5]

Specifications	**Lead-acid**	**NiCd**	**NiMH**	**LiB**
Overcharge tolerance	high	moderate	low	
Self-discharge rate [1]	5%	20%	30%	< 5%
Coulombic efficiency	∼ 90%	∼ 70% to ∼ 90%		∼ 99%
Cycle stability	200-300	∼ 1000	300-500	>1000
Nominal cell voltage	2 V	1.2 V	1.2 V	3.6 - 3.7 V
In use since	Late 1800s	1950	1990	1991
Toxicity	very high	very high	low	low

---

[1] Self-discharge rate is given per month at room temperature

1.1.2 The Lithium-ion battery technology relevance in the electric mobility context

The rise of environmental awareness in society and the leaning towards an ecological alternative to fossil-fuel based transport solutions was met by a political agenda to deviate towards electric mobility (Electric Vehicles). The National Platform for Electric Mobility (NPE) (*Nationale Plattform Elektromobilität* in Gr.), which serves as driving force and think tank, was established jointly by the German government and the German industry [6], and the governmental program for electric mobility [7] was launched. A frequently stated goal is "to position Germany as a lead market and as a lead technology provider for electric mobility" [8–11].

Secondary battery cells are the State-of-the-Art energy storage devices in the Electric Vehicle (EV) and the Hybrid Electric Vehicle (HEV). To achieve the stated goal, several high requirements on the battery technology in use need to be met. Most importantly, the battery should feature a high power density in order to deliver the high current necessary for a high load when required (Acceleration). Simultaneously, it should feature a high energy density in order to run at moderate load for a relatively long time (Driving Range) [5, 12, 13].

Figure 1.1 (adapted from [13–15]) is a chart comparing the specific power (in W/kg, enabler of the acceleration) to the specific energy (in Wh/kg, enabler of the driving range) of several conventional battery technologies (a Ragone diagram).

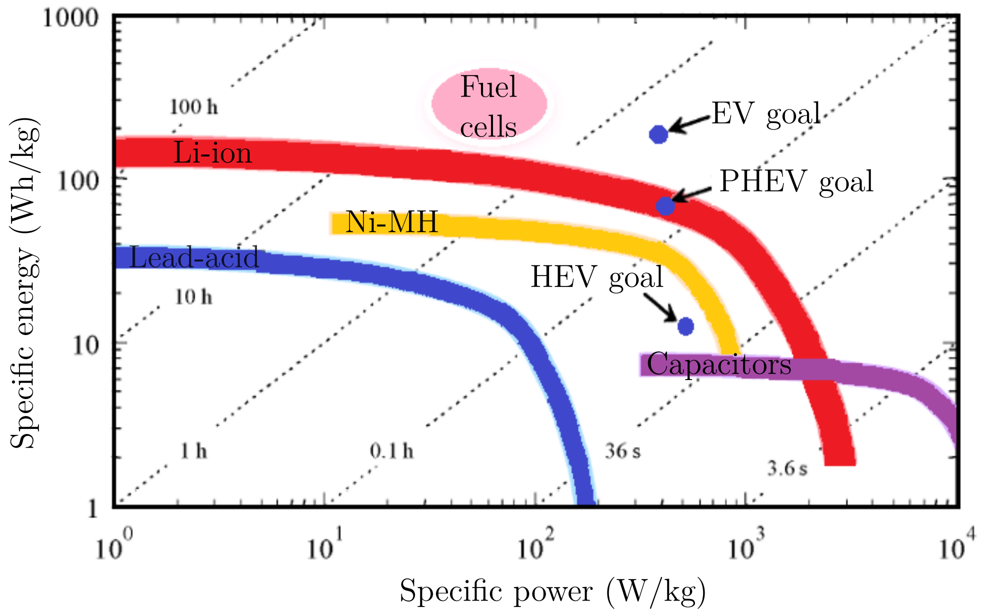

Figure 1.1: A Ragone plot for conventional battery technologies[2] (adapted from [13–15])

---

[2] EV = Electric Vehicle, PHEV = Plug-in Hybrid Electric Vehicle, HEV = Hybrid Electric Vehicle

As can be seen from Figure 1.1, the LiB technology represents the optimal combination in terms of energy density as well as power density compared to other commercial battery technologies, and is the most suitable candidate to answer to the stated requirements. Therefore, this technology is currently dominating the market of electric mobility and typically used in EV. Figure 1.2 [16] shows the historical increase of this market share.

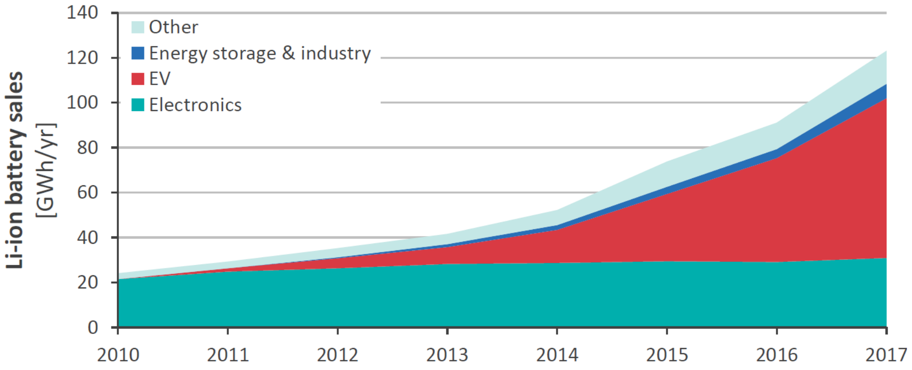

Figure 1.2: Global historical annual growth of the Lithium-ion battery technology in main market segments [16]

1.1.3 Safety concerns and risks related to the Lithium-ion battery technology

The measurable aim stated by the German government is to have one million electric vehicles licensed and running on german roads by 2020 and 6 million by 2030 [7, 11]. Under favorable conditions, with the right monetary and non-monetary incentive measures and the expansion of the charging infrastructure, the user acceptance of EVs would be enhanced and hence the goal would be achieved [17, 18]. However, several statistics and more recent prognoses indicated that even in a non-conservative pro-EV-scenario, it is highly unlikely to achieve this goal [19].

The reasons behind this slow spreading among potential customers are the relatively low driving range of EVs compared to combustion engine vehicles, the cost factor, as well as the safety issues related to the LiB technology [12]. In fact, the battery is still one of the most expensive components of an EV and contributes to the overall relatively high price [12]. In addition, the safety concerns around the LiB technology are still valid. Happenings such as overcharge, deep discharge, overtemperature, excess current and mechanical damage constitute risk situations with different severity and likelihood levels (more details in Section 2.4).

Therefore, an efficient Battery Management System (BMS) is not only beneficial but also critical to ensure the battery operation reliability and keep it within a safe working window during the stand-by as well as the operational modus [20, 21]. The BMS is an electrical/ electromechanical system with software and hardware components dedicated to monitor the battery functionality in order to protect it and extend its lifetime (more details in Chapter 2) [20, 22].

1.2 Thesis objectives

Theoretically identical LiB cells show in practice important differences in their capacity value. The quality of battery cells is dependent on the manufacturing process and its statistical variation. These discrepancies in cells become noticeable only during the active lifetime. Additionally, close and continuous monitoring of the LiB battery cell during the stand-by as well as the operational modus is necessary to ensure that it is working inside a safe operating window and to avoid dangerous scenarios.

Therefore, this work aims to address the architecture and to introduce smartness at the battery cell level with a new concept for individual cell monitoring in order to support the classical BMS. This new concept consists in the design of a Cell Supervisory Circuit (CSC) and its integration inside the battery cell. The CSC, conceptualized and designed in this work, does not consist of State-of-the-Art passive security mechanisms such as current interruption devices and overpressure valves. It rather consists of active elements such as sensors, local memory elements, a digital signal processing unit and a communication interface. All these components are integrated on one compact system (a circuit board), which can be inserted inside the single cell housing. The CSC is electrically supplied from the cell itself. It measures and locally saves battery related parameters during the fabrication stage, together with a time stamp. These measurements can immediately or later be retrieved by the BMS in order to assist with its cell monitoring tasks via the communication interface. The new CSC constitutes with the LiB cell a **Smart-LiB**.

Since a battery is only as strong as its weakest cell, an extreme increase or decrease of a Figure of Merit of the battery cell (or several) outside of the safe window thresholds should be warned for. The new Smart-LiB concept aims to send the necessary warning signals more efficiently and to trigger the necessary protection mechanism on time. The goal is to avoid reaching a point-of-no-return and an irreversible damage of the cell. This thesis presents the concept, the implementation, and the conducted tests to design, fabricate and integrate a CSC.

1.2.1 Overview of related research

Since the electric mobility and the therefore necessary battery technology has become economically and strategically relevant, several recent research efforts were dedicated to investigating innovative battery technologies as well as new battery behavior monitoring concepts and data communication techniques inside the battery system. Particularly, the following research projects present an intersection with the work presented in this thesis.

Project IntLiIon:

Within the framework of the project IntLiIon (Intelligent Data Bus Concepts for Lithium-Ion Batteries in Electric and Hybrid Vehicles) [23], several communication techniques within a Lithium-ion battery were tested. Publications [24–26] reported on the implementation of wireless as well as Powerline-based communication solutions. However, this work presents an optical communication solution, as will be shown in Chapter 3.

Project Smart-LiC:

The SMART-LIC (Smart and Compact Battery Management System Module for Integration into Lithium-Ion Cell for Fully Electric Vehicles) research project [27] is a European commission joint research project of several research institutions and industry partners that has set itself the following objectives:

1. New system architecture: by monitoring and balancing of single cells instead of using a centralized system
2. Determination of battery state: by using Electroimpedance Spectroscopy [21] as well as in-cell measurements for a more accurate determination of the State of Charge, the State of Health and the State of Function of the battery
3. Communication vs. Electromagnetic compatibility: by researching shielding and electromagnetic compatibility issues in order to enhance the wireless and wire-based communication solutions
4. Packaging and system integration: by studying the integration possibilities of the BMS modules inside the battery cells,
5. Reliability, safety and plagiarism: by incorporating safety devices in order to present cell identification and authentication solutions
6. Testing: by using packaged BMS modules to demonstrate the system feasibility and verification of time models

These objectives are very well aligned with the work intended here and a large intersection area is found. However, there are no publications reporting on the state of comprehensive systems. A comparison of the results with those presented in this work is therefore not possible.

Project SafeBatt

The project SafeBatt [28, 29] reports on researching active and passive measures for the intrinsic security of Lithium-ion batteries. The main intersection with the work presented here is the idea of integrated sensors [30] for accurate and real-time measurements, presented however as a single analog interface inside the cell whereas the rest of the processing is conducted outside the cell.

1.2.2 Thesis outline

This thesis follows the outline presented in Figure 1.3.
In Chapter 2, the basic structure of a Lithium-ion battery cell, its aging mechanisms, the complete battery system composition, and the manufacturing process are presented.
In Chapter 3, a successful demonstrator of the Smart-Lithium-ion battery concept is presented. It includes the necessary elements of a Cell Supervisory Circuit as well as a proof-of-concept conducted on a chemically active cell.
In Chaps. 4 and 5, the sensors that can be part of a CSC are enhanced. Chapter 4 presents the design and integration of a different temperature sensor than the one originally used in the demonstrator system of Chapter 3. Chapter 5 reports on the exploring of the realization possibility of a State of Health sensor for a LiB cell based on the measurement of its internal resistance. Design, measurements, and conclusions are presented.
Chapter 6 introduces the packaging and integration aspect of the system by presenting test results on the compatibility of a flexible system with the battery electrolyte solution.
The work's conclusions and outlook are presented in Chapter 7.

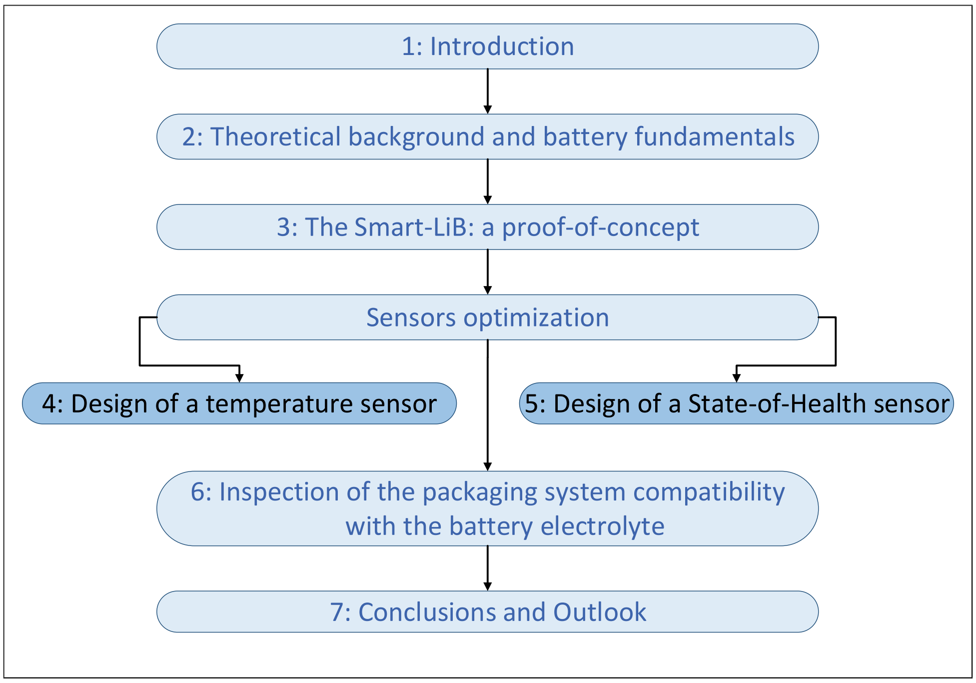

Figure 1.3: Thesis outline

Chapter 2

Theoretical background and Lithium-ion battery fundamentals

This chapter presents the electrochemistry and composition of a Lithium-ion battery cell as well as the fundamentals of the battery system necessary to understand the Smart-Lithium-ion battery concept.

2.1 The Lithium-ion battery cell structure

In its simplest form, a Lithium-ion battery (LiB) (mono-)cell consists necessarily of four components: two electrodes (an anode and a cathode), an electrolyte and a separator. Every specified configuration of given electrodes and electrolyte materials yields an intrinsic voltage, which is the reference voltage of the cell [31]. Figure 2.1 (adapted from [11]) shows the composition of a Lithium-ion cell (LiC).

Although sometimes used interchangeably in the literature, this work differentiates between the battery cell (also called monocell), which is a single electrochemical device with a nominal voltage between 2.2 and 4.2 V for currently available LiB technologies, and the battery as a complete system consisting i.a. of several cells (as described in Section 2.3).

2.1.1 Cell components

2.1.1.1 The electrodes

Each electrode consists of an active material and a current collector connected to it. The technical terms anode and cathode are borrowed from the chemical terminology. The designations of the electrodes as anode and cathode are relative and can be used alternately, depending on whether the respective electrode is being oxidized or reduced, i.e.

---

[1] SEI in Figure 2.1 = Solid Electrolyte Interface

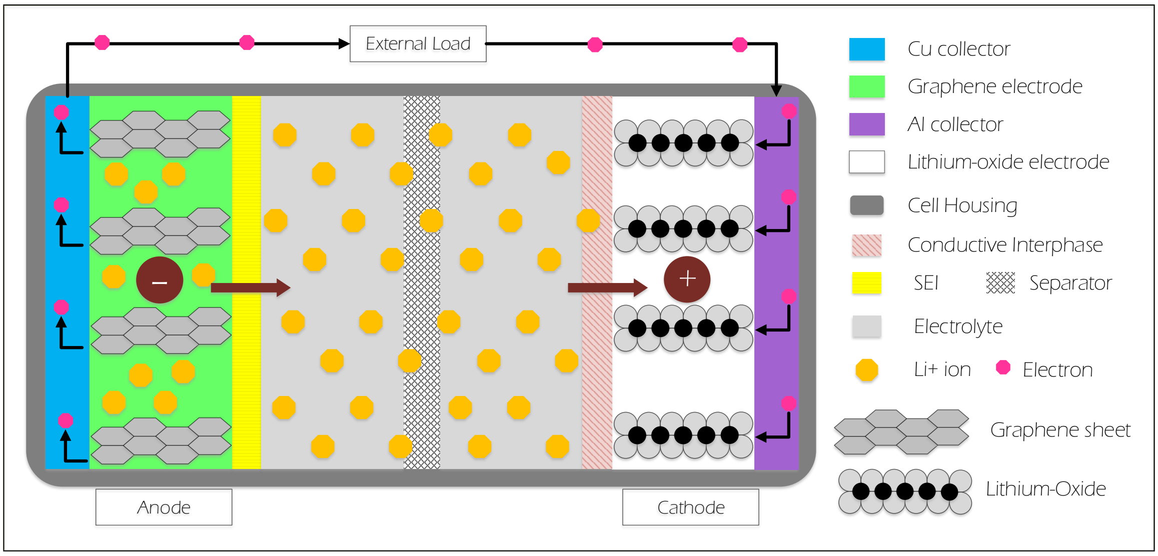

Figure 2.1: The structure of a LiB (mono-)cell[1] (adapted from [11])

the cell is in the charging or discharging cycle. In fact, the LiC is a thermo-electro-chemical system where an Oxidation-Reduction (Redox) reaction is responsible for the current flow [11]. However, it has become common practice in the battery context to use the designations relative to the discharge cycle, i.e. that the anode is the electrically negative electrode delivering electrons to the outside circuit, and the cathode is the electrically positive electrode [22, 32]. This definition will be adopted in this work.
The anode is typically made of Lithium metal [33, 34] or graphite (sheets of graphene) [35]. Graphite offers a high coulombic efficiency and a better cycle stability. The anode current collector is made from Copper (Cu) [11]. The cathode has an Aluminum (Al) current collector and is typically a Lithium (Li) oxide. Table 2.1 (adapted from [5, 36]) shows an overview of commonly used Lithium oxide materials for cathodes and the resulting cell voltage when used in combination with the graphite anode.

2.1.1.2 The electrolyte

The electrolyte plays the important role of intermediary between the electrodes for the electrochemical processes taking place inside the LiC. Electrolytes exist in solid, polymer and liquid forms.
Solid electrolytes can be organic or inorganic. The inorganic ones present a non-flammable safer option [37]. Solid electrolytes would, theoretically, be a better option in terms of mechanical and thermal stability [38]. However, no prototypes of solid electrolytes developed to date are competitive in economic terms compared to the other forms. Therefore, they are still rarely used [11, 38].
Polymer electrolytes are easier to manipulate and safer than liquid ones against leak-

Table 2.1: Common LiC variations with different cathode materials in combination with a graphite material (adapted from [5, 36])

Cell chemistry	**Name/ alternative designations**	**Cathode**	**Nominal voltage**	**Specific energy**	**In use since**
Lithium Cobalt Oxide	LCO, ICR, Li-cobalt	$LiCoO_2$	3.7 - 3.9 V	100 - 200 W h/kg	1991
Lithium Nickel Cobalt Aluminium Oxide	NCA, NCR, Li-aluminium	$LiNiCoAlO_2$	3.65 V	200 - 260 W h/kg	1999
Lithium Nickel Manganese Cobalt Oxide	NMC, INR, NCM	$LiNiMnCoO_2$	3.8 - 4 V	150 - 220 W h/kg	2008
Lithium Manganese Oxide	LMO, IMR, Li-manganese	$LiMn_2O_4$ / $LiMnO_2$	3.9 - 4 V	100 - 150 W h/kg	1999
Lithium Iron Phosphate	LFP, IFR, Li-phosphat	$LiFePO_4$	3.3 V	90 - 160 W h/kg	1996

age, but they suffer from low electrical conductivity. Consequently, **liquid electrolytes** are still the technological choice offering the most advantages and dominating the fabrication processes [11].
Liquid electrolytes are electrolyte solutions mostly made from a Li salt dissolved in an organic solvent. Lithium Hexafluorophosphate ($LiPF_6$) was one of the early researched and commercialized salts and is still widely used. Nevertheless, it has two main disadvantages: it is unstable and is reactive with H_2O: It forms HF as a hydrolysis product. Other examples of Lithium salts include Lithium Tetrafluoroborate ($LiBF_4$) and Lithium Hexafluoroarsenate ($LiAsF_6$). All of these salts are corrosive, toxic and/or harmful [39, 40].
Solvents can be ethers (e.g. Dimethyl Carbonate, Diethyl carbonate, Ethyl Methyl Carbonate, etc.), esthers (e.g. Dimethoxymethane, 1,2-Dimethoxyethane, 1,2-Diethoxyethane, etc.), or from another chemical family. All of these mentioned solvents are flammable, irritant and/or toxic [40].

2.1.1.3 The separator

The separator is a material in gel or in polymer form with a porous structure. It separates the anode and cathode spatially as well as electrically, preventing an electrical short [11]. It is ion-permeable so that only Li^+ ions (and not the electrons) can migrate inside the cell between electrodes [39, 41]. Typical polymer examples used in separators are Polypropylene (PP) and Polyethylene (PE) [42, 43].

2.1.2 Charge and discharge processes of the battery cell

When a load is externally connected to the cell, an electric current flows from the LiB cell terminals to the outside circuit. The anode hosts an oxidation reaction as described by Equation 2.1. A reduction reaction takes place at the cathode according to Equation 2.2, formulated with the example of $LiCoO_2$ as cathode oxide (See Table 2.1) [31, 39, 43].

$$\mathrm{Li_xC_6} \rightarrow x \cdot \mathrm{Li^+} \; + \; x \cdot \mathrm{e^-} + \mathrm{C_6} \tag{2.1}$$

$$\mathrm{Li_{1-x}CoO_2} + x \cdot \mathrm{Li^+} + x \cdot \mathrm{e^-} \rightarrow \mathrm{LiCoO_2} \tag{2.2}$$

The Li atoms are constituted by an Li^+ ion and an electron ($= 1\ e^-$), and are intercalated in the anode (graphene sheets). They diffuse (per solid-state diffusion) to the edge of the electrode active material because of the concentration gradient and go according to Equation 2.1 into their oxidized form. The hereby produced electrons flow from the anode active material (charge passing) through the current collector into the outside circuit (electronic conduction), and through it back to the cathode. The Li^+ ions produced in Equation 2.1 migrate in the electrolyte (ionic conduction) through the separator to the cathode and accumulate to form Li atoms, which then diffuse from the edge to the inside of the active material [39, 43].

These processes are sustained until the concentration of active species in the active material falls below a threshold (the cut-off voltage). The speed with which this threshold is reached depends on thermal and environmental conditions, as well as on the discharge rate [44]. Figure 2.2 (adapted from [43]) shows the processes of the discharge phase. In case of a charging cycle, the electrochemical reactions as well as the physical processes take place in an analogous way but in the opposite directions.

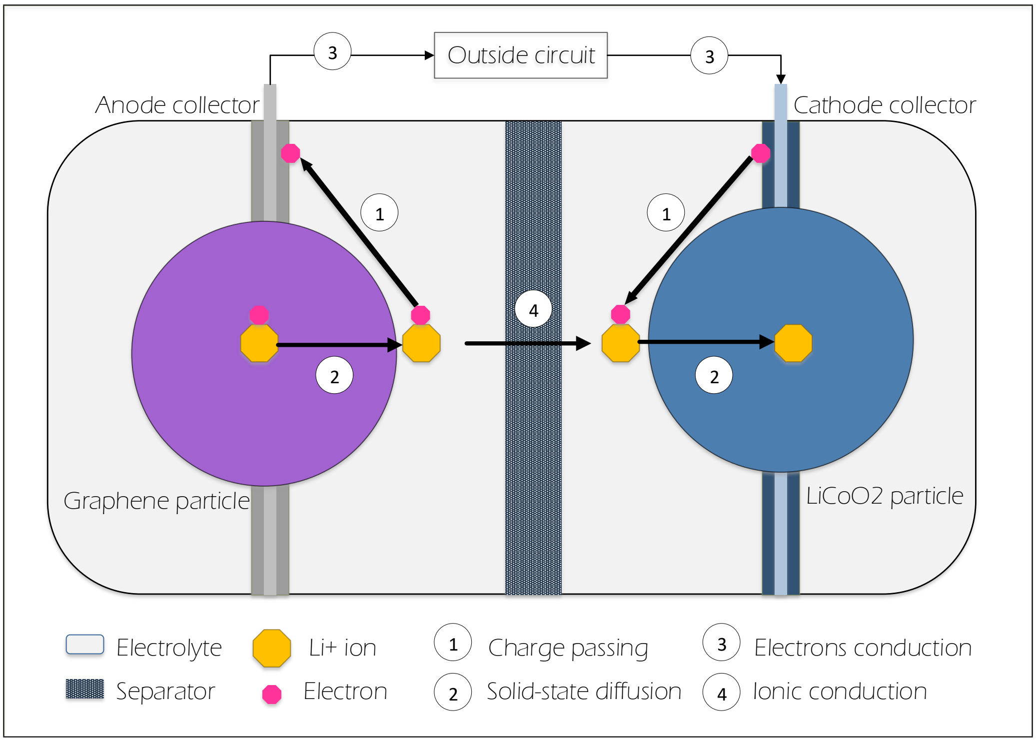

Figure 2.2: The Redox reactions during the discharge of a LiC (adapted from [43])

The Smart-LiB aims to measure several physical quantities (cell voltage, temperature, etc.), which are relevant to the charge and discharge cycles. It thereby monitors the battery cell during its operational life and signals happenings outside the thresholds of the safe operational window to the Battery Management System.

2.2 Battery cell manufacturing and packaging

Lithium-ion cells are commercialized in three main shapes: cylindric (or round) cells (Figure 2.3a), prismatic hard cells (Figure 2.3b) and pouch cells (Figure 2.3c) [11, 45, 46].

The Smart-LiB proof-of-concept (presented in Chapter 3) was tested on pouch cells. The design of the battery cell internal resistance sensor (part of the designed Cell Supervisory

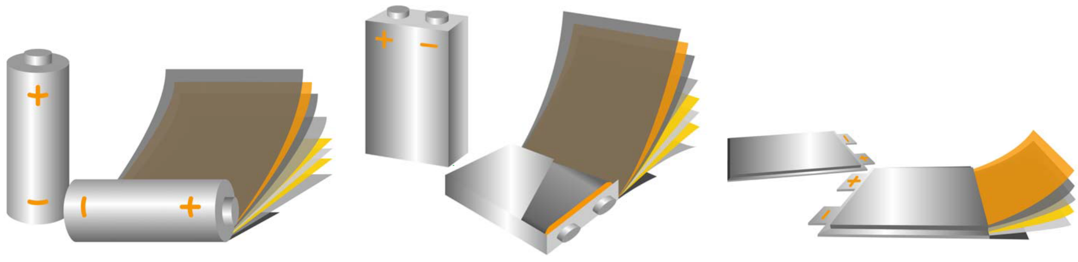

(a) cylindric cell (b) prismatic hard cell (c) pouch cell

Figure 2.3: Overview of LiB cell geometries [11, 45, 46]

Circuit, presented in Chapter 5) was tested on round cells.

The LiB standard manufacturing process consists of three main steps:

- the **electrodes manufacturing**,
- the **cell manufacturing**,
- and the **battery system manufacturing**.

The step of **electrode manufacturing** will not be discussed in detail in this theoretical overview, since there is no direct technical crossover between this step of electrode manufacturing and the Smart-Lithium-ion battery concept.

The steps of **cell manufacturing** and **battery system manufacturing** will be introduced in Sections 2.2 and 2.3, respectively, as shown in Figure 2.4 (adapted from [45, 46]).

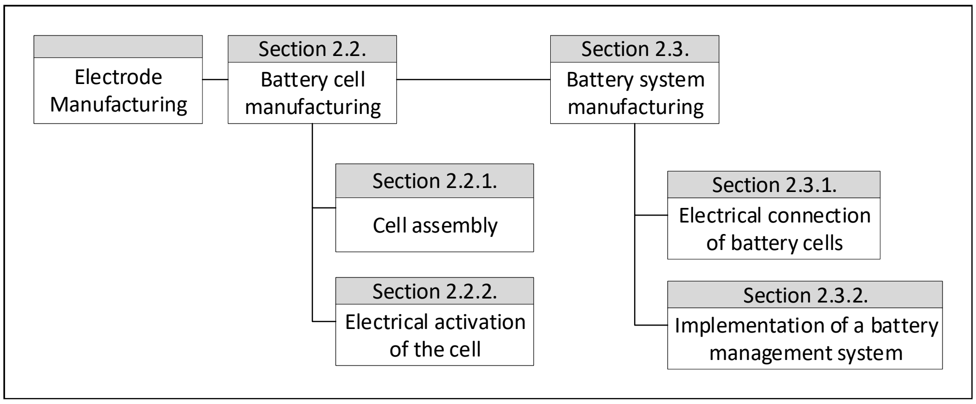

Figure 2.4: Manufacturing steps of a Lithium-ion battery (adapted from [45, 46])

2.2.1 Cell assembly

The intended Smart-LiB system will be integrated inside the cell housing. This integration needs to be carried out during the cell assembly process. The goal is to enable the monitoring of the cell electrical activation and its early life status, in addition to its operational life.

The cell assembly process consists of three steps:

(i) separation/cutting of the manufactured electrodes and of the separator
(ii) the compound assembly
(iii) the packaging inside a housing

The sequence order that the steps take and the used technique for the compound assembly depend on the cell outer shape geometry (See Figure 2.3).

2.2.1.1 Cell assembly for pouch cells

For pouch cells, and after the electrodes manufacturing, the cell assembly steps are carried out in the following order:

(i) the cutting of electrode and separator sheets: The first step is the separation of anode sheets, cathode sheets and separator sheets. Since the electrodes and separator materials are manufactured in rolls, their separation is carried out by laser or shearing cut (with a punching tool) [46].

(ii) the compound assembly by folding and stacking: The second step consists in the stacking of previously cut anode and cathode sheets together with the separator. Single sheets of electrodes and separator are stacked onto each other. Alternatively, single sheets of anode and cathode are alternately placed in the pockets of a previously prepared and in z-form folded separator structure [45, 46]. Figure 2.5 [46] shows the stacking operation.

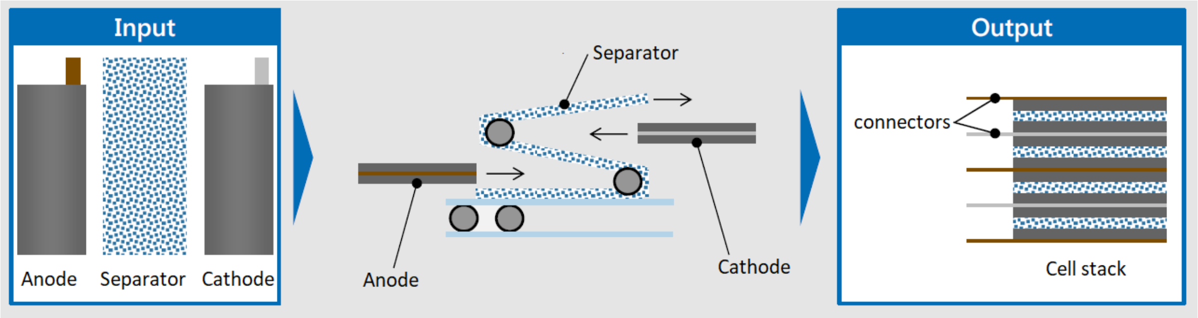

Figure 2.5: The stacking operation of pouch cells electrodes [46]

(iii) the packaging and (partial) sealing: In this step, the resulting stack from step (ii) is inserted into a housing. The housing in this case is a pouch foil with a prismatic form. This foil is an aluminum compound foil and must answer to several requirements: tensile strength, sealability, sealing strength, permeability for water vapor and electrolyte, electrolyte compatibility and integrity (also in contact with the electrolyte) [47]. The composition of materials used for the aluminum compound foil are a combination of oriented Polyamid (OPA), Polyethylene (PE), Aluminium (Al) and Polypropylene (PP). The current connectors of the stacked electrodes tabs are then welded (using an ultrasound or laser welding process) and the electrodes are connected to the corresponding Al or Cu terminal. The stack is by now a complete stack of folded and stacked electrodes with welded connectors and connected terminals. It is then inserted into a previously deep-drawn pouch foil and (partially) sealed. This sealing is partial because it is carried out at only three edges. In fact, the electrolyte filling (step (i) of Subsection 2.2.2: Electrical activation of the cell) is carried out through this last opening, after which the fourth edge is sealed. After the formation of the cell [2], gas is formed and fills up the gas bag, a reservoir within the housing of the pouch cell specifically designed for this purpose. Only then is the final sealing carried out [45, 46].

2.2.1.2 Cell assembly for cylindric and prismatic hard-case cells

Unlike for pouch cells, the cell assembly steps are carried out in a different order for cylindric and prismatic hard-case cells.

(i) the compound assembly by winding: The electrodes are manufactured in the form of foils. They are then passed as rolls to the next process step where they are vacuum cleaned before the winding (compound assembly). For round cells, the electrodes foils as well as 2 separator foils undergo a round winding process around a central pin (as shown in Figure 2.6a [46]). For prismatic hard-case cells, the foils undergo a flat winding around a winding mandrel (as shown in Figure 2.6b [46]).

(ii) the cutting of electrode and separator sheets: When the winding result (called jelly roll) has reached its intended dimension, the electrodes and separator foils undergo the cutting sequence and are fixed using an adhesive tape (as shown in Figure 2.7) [45, 46].

(iii) the insertion into housing and sealing: In this step, the terminals need to be welded, generally using ultrasound. Afterwards, the jelly rolls are inserted inside their corresponding housings. This process is delicate, and an insulating foil is needed to protect the jelly rolls during the insertion. A complete sealing of the housing can then be carried out, generally using a laser welding process [45, 46].

---

[2] The formation is an essential step during the electrical activation of the cell. It is described in step (ii) of Subsection 2.2.2: Electrical activation of the cell

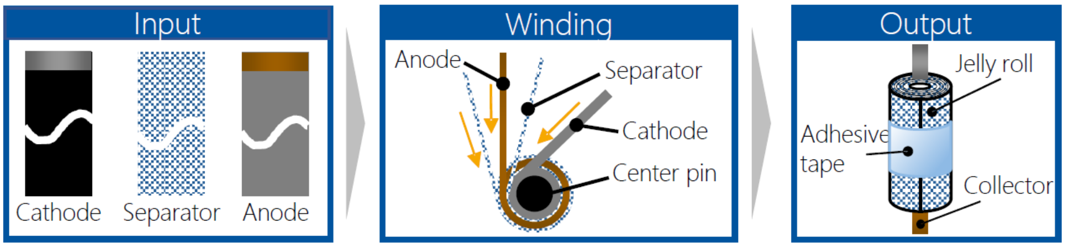

(a) Winding of a cylindric cell

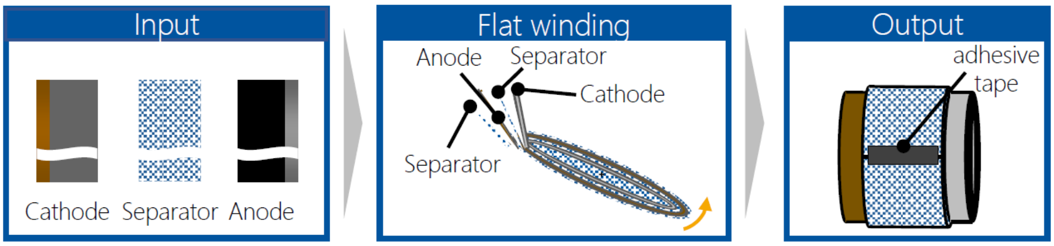

(b) Winding of a prismatic hard cell

Figure 2.6: The winding operation of cylindric and prismatic hard-case cells [46]

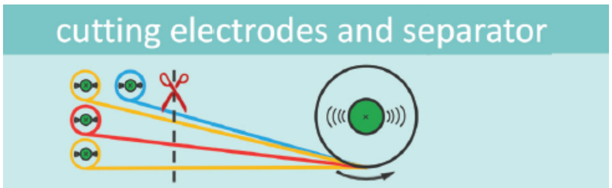

Figure 2.7: The cutting operation for cylindric and prismatic hard-case cells [45, 46]

2.2.2 Electrical activation of the cell

The electrical activation process of a LiB cell consists of three steps:

(i) Electrolyte filling
(ii) Formation
(iii) Aging

(i) Electrolyte filling: After the insertion into the housing (independently of the cell outer shape), a dosing needle is used to fill the liquid electrolyte. Several partial fillings and evacuation steps can be carried out. Afterwards the electrolyte filling valve is sealed. For pouch cells, this corresponds to the sealing of the fourth edge, the degassing, and the final sealing.

(ii) Formation: The formation constitutes the very first charge and discharge cycles of a LiC. During the charging phase of the formation, the Li ions, stored within the graphene sheets on the anode side, create an interface layer between the electrode and the electrolyte called Solid Electrolyte Interface (SEI). The analogous phenomenon on the cathode side is labeled Conductive Interphase [11, 48] (See SEI and Conductive Interphase in Figure 2.1).

The formation can last several hours or days. Figure 2.8 shows an example of a charging curve (single charging cycle) of a LiC stopped at the threshold of 3.5 V and the corresponding charging current [3]. Although it is a process with precisely defined parameters, the formation is subject to statistical variations. This leads to important quality discrepancies between cells. These discrepancies are unfortunately unpredictable and only visible during the active lifetime. As will be presented in Chapter 3, the Smart-Lithium-ion battery concept presents a work around to this shortcoming.

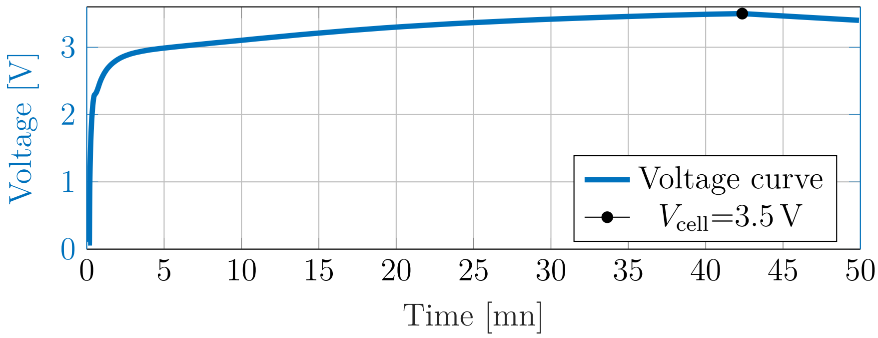

(a) The voltage curve

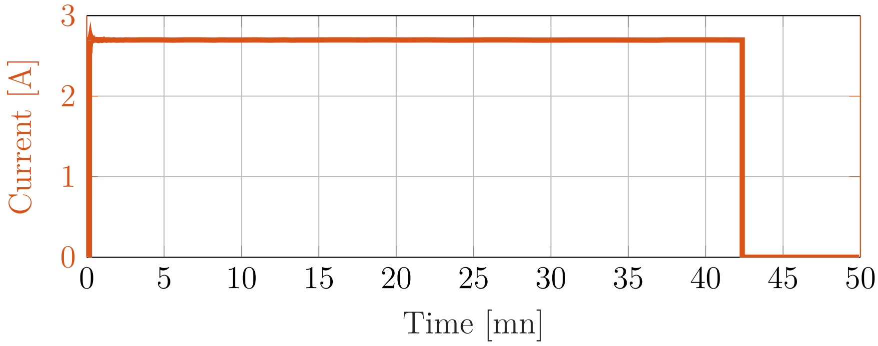

(b) The corresponding current curve

Figure 2.8: The typical LiB formation curve

(iii) Aging: The aging is the last step of the electrical activation of the cell. It is done by subjecting the battery cell to several charge and discharge cycles and ensures the manufacturing quality by identifying potential internal short circuits. It can last up to several weeks, during which cell parameters and characteristics (mainly the Open Circuit Voltage) are closely monitored. A good consistency in the parameters indicates that the cell is of high quality and can be delivered to the customer. Two different aging processes are

---

[3] Data of Figure 2.8 is a courtesy of the Smart-LiB project partner Zentrum für Sonnenenergie- und Wasserstoff-Forschung Baden-Württemberg (ZSW-BW), more details in Chapter 3

possible: the high temperature aging process and the normal temperature aging process. The cell typically undergoes the normal temperature aging process first. The aging processes do not differ according to the cell geometry shape, although a so-called pre-aging is carried out for round and prismatic cells, in order to avoid their deformation because of gas formation. For pouch cells, this is bypassed by the presence of the gas bag and its subsequent emptying before the final sealing [45, 46] (See previous Subsection 2.2.1.1).

2.3 Battery system composition

After the single cell production is finalized, the manufacturing process includes two final steps towards the complete battery system: the module assembly and the battery pack assembly.

2.3.1 Module assembly

The currently available Lithium-ion battery technologies produce cells with a nominal voltage between 2.2 and 4.2 V. This voltage is not enough to supply the intended EV/HEV applications. Therefore, several cells are connected in series to produce a so-called module, having a higher supply voltage. For example, 10 cells with a nominal voltage of 3.6 V produce a supply with a nominal voltage of 36 V.

A parallel arrangement of cells, on the other hand, would not increase the total voltage but rather the total available capacity (charge quantity in A h) [11]. The parallel configuration is used where higher currents are needed (e.g. acceleration scenario for EV).

Figure 2.9 [49] shows graphical examples of modules composed from the different LiB cell geometries.

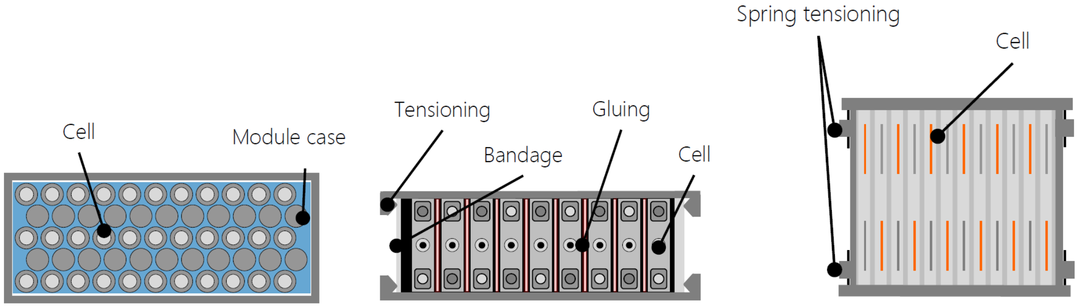

(a) Module of cylindric cells **(b)** Module of prismatic cells **(c)** Module of pouch cells

Figure 2.9: Overview of LiB modules with different cell geometries [49]

Depending on the geometry, the cells are placed in an adequate predefined stack and housing. After the exact positioning, the cells are either glued using adhesive material or adhesive foils (cylindric cells), or screwed in place (prismatic hard cells), or fixed using springs (pouch cells). All cells have a certain “breathing” behavior, i.e. during charge and discharge, they are subject to geometrical expansion and contraction, respectively. By enforcing a pressing stacking positioning, this effect is minimized.

The terminals/ current collectors need then to be electrically contacted in order to realize the series and/or parallel connection, using one of the techniques presented in Table 2.2 [49].

Table 2.2: Common welding techniques for LiB cells inside modules [49]

Technique	**Advantages**	**Disadvantages**
Laser	Fast/ Efficient	High heat input
Ultrasonic	Gentle	expensive
Current	Low investment	Material dependent
Screws	Detachable connection	Contact resistance

The cooling at module level is optional and can be realized, depending on the available interspace, using a cooling liquid. On top of the module, a Slave Circuit Board can be mounted and fixed. It is a slave to the Battery Management System (BMS) and contains sensors (Voltage and temperature sensors). Its supply and communication interface (CAN-Bus) to the BMS are connected as well [49].

2.3.2 Battery pack assembly and the Battery Management System

The complete battery pack (or battery system) consists of several modules together with other electrical and mechanical components. How many modules and which connections are used (in series and/or in parallel) depends on the intended application. As explained in the previous section, a series configuration increases the total supply until the voltage required by the application, whereas a parallel configuration increases the total charge quantity available in the battery and therefore enhances the power capabilities of the supplied system.

Except in the case of a distributed battery system architecture (for more effectiveness in space use [24]), the battery pack is generally compact inside the battery pack housing. Besides numerous modules, a battery pack consists of mechanical components including a housing case with the necessary isolation, mounting components and a cooling system, typically a cooling plate at the bottom of the housing which can also ensure a heating function if necessary [11, 49].

An essential component of a battery pack is its Battery Management System (BMS). The State-of-the-Art BMS is a complex system of several hardware and software components, which ensures the tasks of cell monitoring, active and passive cell balancing, thermal management and charge control [11, 44, 50]. It guarantees the reliable functioning of the LiB battery and keeps its cells within their designed operation window. The use of the battery is hence optimized and its lifetime during its first-use-application is increased. The BMS anticipates risks, conducts self-tests, and interferes in the stand-by and active operative modes. In addition, it estimates and monitors the State of Charge and State of Health of the battery [4]. Therefore, it needs to collect real-time battery data and parameters, and to satisfy the conditions of measurement accuracy and data integrity [20]. As will be explained in Chapter 3, the Smart-LiB system supports the BMS with the real-time collection and communication of battery relevant data.

2.4 Risk situations and possible abuse scenarios

Figure 2.10 [30] shows the possible reactions of a LiB cell under different external stimuli it can be subject to. The abuse scenarios can be of mechanical (e.g. mechanical damage of housing), electrical (e.g. overcharge, deep discharge), and/or thermal nature (e.g. extreme heating). The approach to handle the safety issue can be addressed during one or more of the battery lifetime stages [30], i.e. during the design stage, the testing stage, or the run-time stage/ battery's operational life.
These happenings display risky events with given severity and likelihood levels and can lead to consequences ranging from faulty battery behavior to fire, rupture or explosion. Hazards levels from 1 to 4 (as given in Table 2.3 [51, 52]) are considered tolerable to humans, whereas hazards levels 5, 6 and 7 lead to a rejection of the cell.

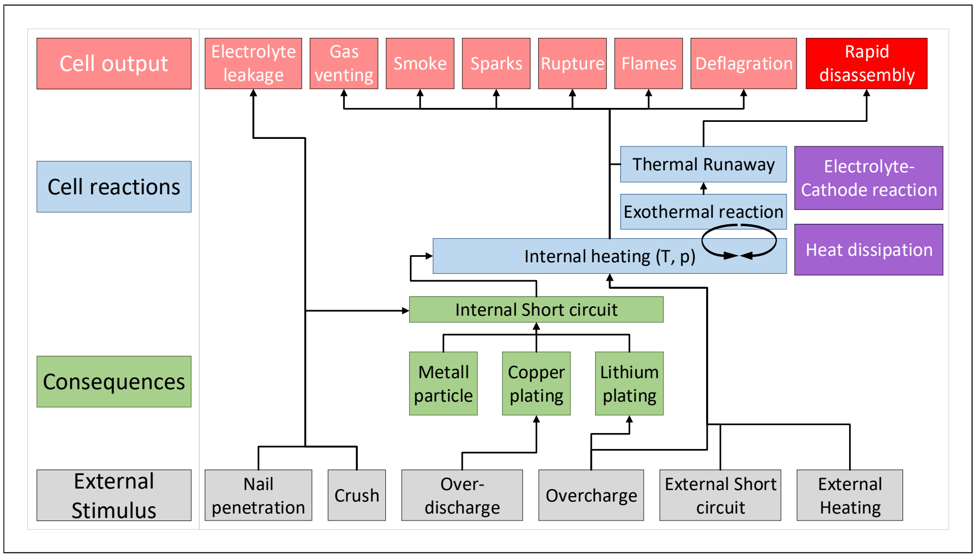

Figure 2.10: LiB cell reactions to external stimuli [30]

---

[4] Definitions and more details on the State of Charge and State of Health of the battery in Section 3.2

As can be seen from Figure 2.10, all these risk scenarios can generate heat or be detected by an abnormal increase in the cell temperature. Therefore, a temperature sensor is an essential component in the monitoring system intended by the Smart-LiB concept.

Table 2.3: European Council for Automotive R&D hazard levels for battery safety tests [51, 52]

Level	Description	Classification criteria and effect
0	No effect	No loss of functionality
1	Passive protection activated	Cell reversibly damaged. Repair needed.
2	Defect	No leakage. Cell irreversibly damaged. Repair needed.
3	Minor leakage or venting	Weight loss $<$ 50% of electrolyte weight.
4	Major leakage or venting	No fire or flame. Weight loss $>$ 50% of electrolyte weight.
5	Rupture	No explosion, but some internal parts are expelled.
6	Fire or flame	No explosion.
7	Explosion	Explosion (disintegration).

2.5 Aging of Lithium-ion batteries

The aging of a battery cell [5] is the reduction of its capacity and other characteristics due to long-term degradation effects [34, 53, 54]. LiB cells have a high cycle stability, i.e. they undergo up to one or several thousand cycles (compared to several hundred for other battery technologies [5], see Table 1.4) before they start showing degradation effects due to age.

When the aging results in a capacity fade of 20% or more, it makes the cell no more suitable for its first-life-application, i.e. its intended application that it was designed for (in this case automotive/ mobile application). It is then routed towards its second-life application (generally a stationary application for LiB technology in opposition to the automotive/ mobile first life application) or towards recycling. The degradation can affect the electrodes, the electrolyte and/or the separator. Table. 2.4 [34] shows typical aging effects of the different battery cell components together with their causes and their consequences. These effects are amplified with temperature [54]. Destructive as well as non-destructive methods can be applied to assess the aging of a given Lithium-ion cell [34].

One Figure of Merit pointing to the aging of a LiB cell is the increase of its internal resistance. When the internal resistance of a battery cell has increased to 200% of its

---

[5] The term **aging** is used here to describe the actual "growing older" of the cell, resulting in the fading of its capacity compared to its Begin of Life due to the high number of charge and discharge cycles through out its life time. It is to be differentiated form the technical term **aging** describing a necessary and final step in the cell manufacturing process as described in step (iii) of Subsection 2.2.2: Electrical activation of the cell

Table 2.4: LiB aging effects [34]

Affected component		**Physical/ Electrochemical effect**	**Cause**	**Consequence**
Electrolyte		electrolyte decomposition	overcharge overdischarge	electrolyte conductivity ↘ internal resistance ↗
Anode	**Graphite**	additional SEI layers [6]	intercalation of Li in graphite layers	lattice volume ↗ surface film stretching and destruction
	Li metal	dendrite or moss growth [7]	small discharge currents	self-discharge ↗ risk of internal short circuit
Cathode		material decomposition	high cell voltages	irreversible capacity loss risk of thermal runaway
Battery System		mechanical stress	lattice volume change	particle size ↘ encapsulation of electrode parts

---

[6] Although the formation of a Solid Electrolyte Interface (SEI) layer is a necessary step for the functioning of the cell (Subsection 2.2.2), the growth of the interface by additional layers harms the cell [53].

[7] Dendrites have a protrusive structure and risk puncturing the separator, causing thereby an internal short circuit and consequently a thermal runaway [54].

value at the cell's Begin of Life, it is considered that the cell is no longer suitable for its first-life-application. In this work, an internal resistance sensor assessing the aging of a LiB cell is designed and tested in Chapter 5.

2.6 Modeling of Lithium-ion batteries

Modeling of Lithium-ion batteries is necessary for the assessment of their status and quality during rest periods [55], as well as for management and balancing decisions in the active operative mode. Depending on the intended application, models can have different levels of **accuracy** (of status predictions), **complexity** (number of parameters needed to configure the model), and **physical interpretability** (level of directly correlated depiction of physical and electrochemical mechanisms and their dependence on temperature, age, etc.).

The models can therefore be classified into physical, empirical, and abstract models [8]. Table 2.5 [39] shows the different models used for Lithium-ion batteries and compares their characteristics. In applications similar to the Smart-LiB concept, abstract models are the most suitable given the computational resources available on the system (microcontroller as a digital signal processing unit).

Table 2.5: LiB models comparison [39]

Models	**Accuracy**	**Complexity**	**Physical interpretability**	**Suited application**
Physical	Very high	High ($>$ 50 parameters)	High	Battery system design stage
Empirical	Medium	Low (2 to 3 parameters)	Low	Predictions of life time and efficiency
Abstract	Medium	Medium to low (2 to 30 parameters)	Limited to acceptable	Real-time monitoring and diagnosis

2.6.1 Physical models

Also known as white boxes [43], physical models are low-level models of thermal and/or physical nature with a high accuracy level [44]. They describe the structure of the materials and reflect the reality of the physical and electrochemical phenomena happening inside the LiC, namely thermodynamics, active species kinetics and transport phenomena (as presented in Figure 2.2).

A large number of parameters and an exhaustive configuration effort are necessary to

---

[8] This modeling comparison was partially published in [39].

establish the interdependent differential equations on which such models are based. Although offering a useful insight and a high level of accuracy, these models are difficult to implement with limited computational and memory resources [39].

2.6.2 Empirical models

Empirical models are also called black boxes [43]. They use empirical parameters which offer limited physical significance [44]. The empirical parameters are generally entities of mathematical nature and easy to introduce into a status estimation algorithm. However, these models offer a poor insight into the battery system. Improved empirical models based on stochastics and/or fuzzy logic can deliver battery related parameters [56, 57].

2.6.3 Abstract models

Abstract models provide an alternative representation of the physical entity and are, therefore, known as grey boxes [43]. An equivalent representation of the battery system can have different forms. A popular approach is to use an electrical equivalent circuit. This allows for the complex electrochemical process to be replaced by a simple electrical circuit. This preserves the correlation with battery dynamics, without compromising much of the accuracy [58]. A configuration effort is needed to match the model parameters with experimental data. The complexity is, however, flexible and goes from basic circuits (e.g. one serial resistance and one or several RC dynamic elements) to more complex structures including environmental, age and second-order effects. Depending on the requirements and resources, the user can trade-off the high accuracy and the computational feasibility [39, 58].

Chapter 3

The Smart-Lithium-ion battery Concept: A Demonstrator

3.1 The Smart-Lithium-ion battery cell

The quality and price of Lithium-ion cells is strongly dependent on the manufacturing quality. As presented in Section 2.2, the production process includes several steps with defined parameters. The statistical variations from the optimal process parameters, even at minor deviation levels, reduce the yield of good quality cells. Substantial discrepancies in the produced cells capacities can then be observed. These discrepancies as well as several mistakes in the production process are unpredictable and only visible or detectable during the active lifetime. This leads to limitations in the reliability of the cells, since a Lithium-ion battery is only as strong as its weakest cell.

The process parameters are nowadays being precisely documented throughout the production cycle. However, a close monitoring of the “inner life” of the Lithium-ion cell (LiC) and its internal electrochemical processes, especially during the formation step (See Subsection 2.2.2), is still very limited. Sensors are available only at the module level (See Subsection 2.3.1: Module assembly).

In addition, the LiB technology can still not be considered safe. As presented in Section 2.4 (Figure 2.10 [30]), internal and external short circuits, overcharge and overdischarge, nail penetration and other external accidents can lead the LiC to irreversible damages.

The Smart-Lithium-ion battery (Smart-LiB) concept presents a solution to overcome these challenges by introducing smartness at cell level. This is done by monitoring the inner life of the LiC during the formation and the last production steps, the first cycles of operation, as well as the operative lifetime using a dedicated integrated circuit.

Sensors of the vital battery parameters are used. They are completely integrated inside the cell housing and placed close to the physical happening of electrochemical processes.

By communicating the sensors measurements to an external monitoring and management unit (e.g. the Battery Management System), accurate real-time data is collected. This helps improve the production quality and understand the specific status of every cell. This local, compact and smart monitoring system at cell level will be referred to as Cell Supervisory Circuit (CSC) in the following parts of this work. Figure 3.1 shows a possible placement of the CSC inside a prismatic battery cell.

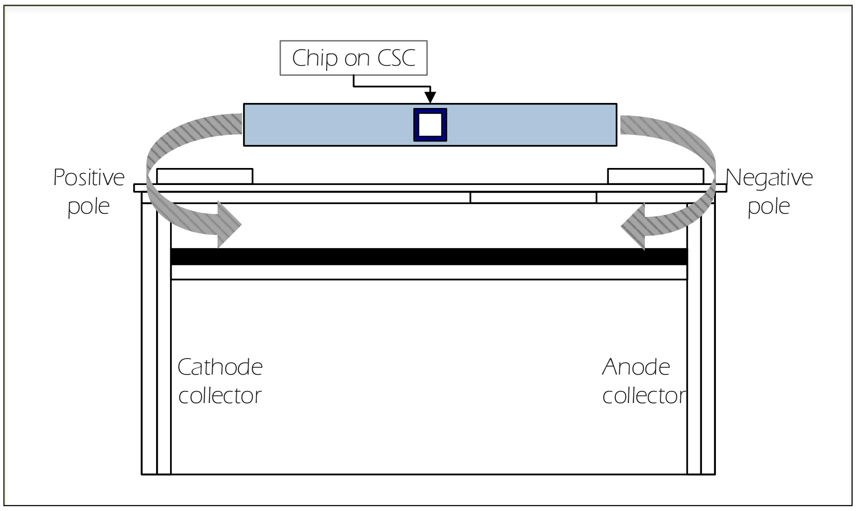

Figure 3.1: The Smart-LiB concept

A CSC can contain the mentioned sensors, relevant local front-end processing, a digital processing unit, a communication interface, local data storage elements along with actuators, as shown in Figure 3.2. Every cell together with its own CSC and a unique identifier (address) is a “smart cell”.

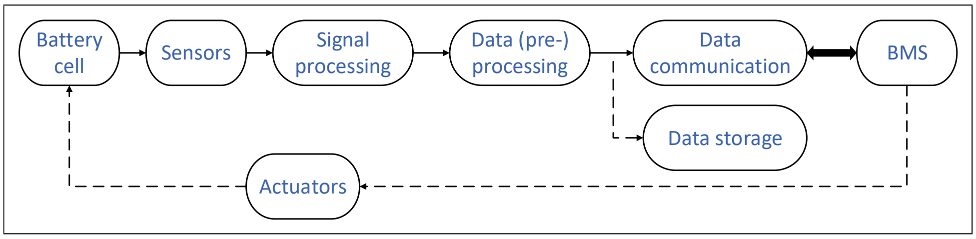

Figure 3.2: The Cell Supervisory Circuit (CSC) components

The final planned Smart-LiB product is a thinned-down electronic chip [59] (See Figure 3.1), which integrates the functionalities of the CSC described above on one monolithic solution, laminated for packaging and protection with a foil packaging system and connected to the poles of the LiC. For the chip packaging, the Chip Film Patch (CFP) Technology is to be adopted [60, 61].

The connection to the poles enables the electrical supplying of the chip by the cell itself. The measurement data of voltage, temperature and other quantities acquired by the chip is sent to the Battery Management System (BMS) using the communication interface. In case of a hazardous happening that constitutes a severe risk to the cell, a warning can be issued on time and with a larger maneuvering possibility before the point of no-return is reached. The actuators of the CSC can then be activated to treat the cell or to release its connection from the rest of the pack, in order to prevent damage to neighboring cells. Likewise, the BMS can contact the smart cells individually, using their respective unique addresses, either in a periodic or a scattered manner, in order to inquire about data or status (Figure 3.3).

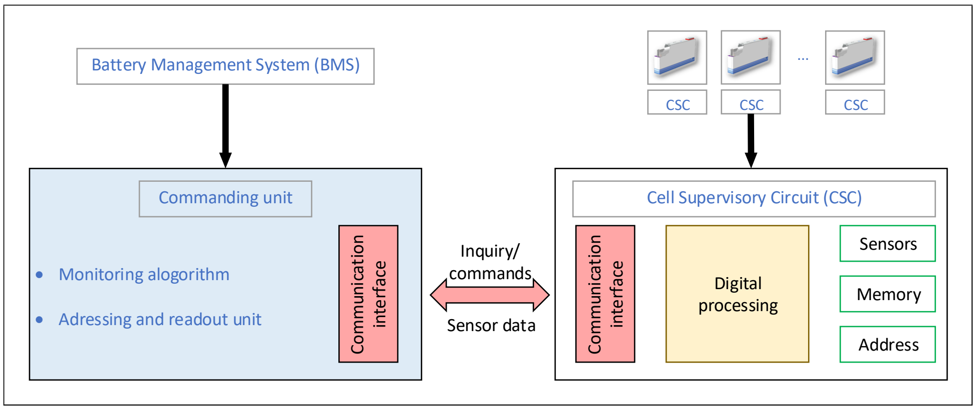

Figure 3.3: The Smart-Lithium-ion battery system overview

The State-of-the-Art communication protocol between battery modules and the BMS in Li-ion batteries uses data bus systems, e.g. the Controller Area Network (CAN)-bus system [24]. If the CSC in every cell would be connected to the BMS using the same network, a huge amount of cabling would be needed. This leads to an important increase in the total weight of a battery, which is rather undesirable in EVs. To minimize the required amount of needed circuitry, the communication protocol used for the CSC should be cable-free or at least not weigh down the battery with any additional cabling, but rather use the existing connections.

3.1.1 Unique features of the Smart-Lithium-ion battery concept

A successful manufacturing of a final product according to the Smart-LiB concept presenting a thin chip encapsulated in polymers according to the CFP technology process would offer several uniqueness features over the SoA monitoring solutions for LiB cells or currently conducted research:

- The encapsulation of back-thinned chips (down to $< 20\,\mu m$) and their thin packages (around $100\,\mu m$) into the limited available space inside the battery housing is possible.

- The reduced geometric dimensions of the sensor devices allow for closeness to where the electrochemical processes physically take place. This makes measurements of temperature, pressure, etc. more accurate. Hence, evaluations of the cell status based on retrieved information is more reliable.

- The enabled *in-situ* monitoring of the important last production steps of the cell (formation and first aging cycles, Subsection 2.2.1) as well as early life stages presents a valuable insight that would otherwise be inaccessible.
  First, it allows to learn more about the first life stages of cell. Results can constitute the first base towards a "smarter" cell production process line.
  Second, it enables an uninterrupted tracing of the cell's State of Health (SoH) from the manufacturing step to the operational lifetime. The hereby created "product memory" offers valuable data towards the second-life application and recycling phases.

- The packaging of the chip serves as protection from the harsh chemical environment that is the battery electrolyte as well as a routing support to supply and connect the monitoring circuit.

- The complete integration of the CSC as a monitoring system can be included as an additional in-between step in the cell manufacturing process as described in Section 2.2 without major changes in the process line, thereby avoiding high implementation costs. For pouch cells, it can be positioned immediately after the stacking and folding step. For round and prismatic hard-case cells, it can be the concluding step after the winding and before the final welding.

- The design of the CSC should aim for a low-power system. The supplying of this system from the cell itself reduces the circuitry effort considerably. This leads to a simpler architecture and a reduced overall weight.

3.1.2 Challenges and tasks

Several challenges will be faced when carrying out the realization and implementation of the Smart-LiB concept. The expected challenges are of mechanical, chemical, and electrical nature.

3.1.2.1 Mechanical challenges

The integration of foreign devices inside the housing of a battery cell is so far untested. Since the highest energy density possible is pursued inside a Lithium-ion cell, the standard configuration hardly offers any remaining space to implement a monitoring system.

Claiming any additional space to integrate the CSC comes at the cost of a lower energy density of the cell, which is undesired. Therefore, the system needs to have minimal dimensions.

The first mechanical challenge to be faced is finding space with sufficient geometrical dimensions to include the CSC and its packaging. The second one is to connect the CSC supplies and to lead all of its necessary connections through the cell housing to the outside without causing leak tightness damages.

3.1.2.2 Chemical challenges

The battery electrolyte is a harsh chemical environment. The SoA components of a battery cell are selected so that they are inert to it. However, the compatibility of the chip and packaging materials that will be used in the CSC with the electrolyte is so far untested. This chapter presents a workaround to this problem. Chapter 6 treats it as well.

3.1.2.3 Electrical challenges

The first task is to implement several different elements on a single medium. In the final result (CSC as chip), this requires the design and the management of the physical layout of all functionalities (sensor elements, analog and digital processing, memory elements, etc.) on one monolithic design.

As an intermediate step, the CSC is realized as an assembled Printed Circuit Board (PCB). A system design task solving is then necessary: choosing elements available on the market according to the technical requirements for the sensor devices, correctly interconnect, place and route them, tune their operation for a correct intercommunication and program their digital controlling. The related challenge in this system design phase is to keep the design at a low power level. Since the monitoring system that is the CSC is supplied by the LiB cell itself, it is undesired that the circuit consumes much power from the cell, which would preferably flow into the intended application.

On another aspect, the voltages treated in this context are manageable. However, some LiB cells have capacities of several tens of Ampere (A h), and in case of external short circuit or a hazardous event, which are the happenings that the CSC is meant to treat, electrical currents of several Ampere could flow. From a circuit design aspect, the elements in the CSC, either designed or chosen from the market, should have a sufficiently high power rating.

3.2 Possible sensors in the Lithium-ion battery context

To assess the real-time status of a battery cell using the Smart-LiB concept, different quantities should be continuously monitored by direct measurements and/or estimations. In this section, the different sensors of theses quantities are presented and classified into physical and defined quantities. The physical quantities are universally defined and directly measurable, e.g. voltage or temperature. The defined quantities are specific to the battery. They are not direct physical quantities in the analog (electro-)chemical or the electrical domain, but rather defined quantities, which are relevant in the LiB context, i.e. the State of Charge (SoC), the State of Health (SoH) and the State of Function (SoF).

3.2.1 Physical quantities

3.2.1.1 Voltage

The Open Circuit Voltage (OCV) of a Lithium-ion cell is extracted by a high-impedance measurement in the unloaded status (no load is connected). It is the first indicator of the cell status by comparing the measured values to values in look-up tables and statistical models. Figure 3.4 is a qualitatively typical discharge curve of a LiB, showing the decrease of the OCV over time using a constant discharge current (adapted from the model *battery* in [62]). The OCV passes through three main regions during the discharge of the cell: the exponential area, the nominal area, and the breakdown.

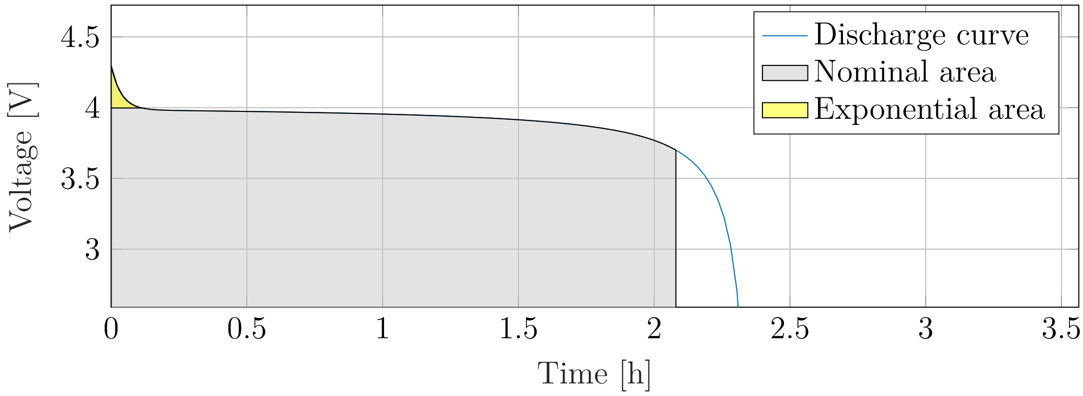

Figure 3.4: The typical LiB cell discharge curve (adapted from the model *battery* in [62])

The nominal area is the longest lasting. The voltage is then almost constant at the nominal voltage. This represents one important positive feature of Li-ion batteries. In fact, the circuit or the application depending on the cell can be supplied with a constantly stable voltage down to relatively low State of Charge (SoC) levels.

However, this presents a challenge to the estimation of the SoC, since the OCV is barely dependent on it and remains stable from SoC values ranging from ≈ 90% down to ≈ 20%. Like for any other battery cell, the OCV should be measured as a first indicator. However, it alone is not sufficient. Other quantities need to be additionally retrieved or sensed, in order to better evaluate the status of the cell. When OCV measurements in the µV range (for a precise localization on the discharge curve) are combined with a coulomb counter delivering measurements in the µA (for a complete consideration of all discharge and leakage currents) range, a more accurate estimation of the consumed and remaining capacity is possible (Subsection 3.2.2) [20, 22].

As presented in Chapter 5, physical processes inside the LiB cell can be very slow with frequencies in the µHz and mHz range. The OCV has to be measured in the unloaded state and after these processes have settled. Therefore, a rest period of at least 1 h before measurement is recommended [63].

3.2.1.2 Reference voltage

It is common practice in electrochemical systems to conduct high-impedance measurements of electrical potential differences of specific points or active electrodes relatively to a so-called “Reference electrode”. The active (or working) electrode is the electrode of which the potential is to be measured. The reference electrode is the one with a constant and reproducible equilibrium potential and serves as reference point to the other measurements. The commonly used reference electrode is the Standard Hydrogen Electrode [11, 64]. The active and the reference electrodes must be connected through an ion-conductive medium (the electrolyte in the battery cell case). If there is gradient in the ion concentration (because of intercalation and de-intercalation) or if a hybrid composition of the medium is used, a diffusion overpotential will additionally be seen at the output.

In the context of Li-ion batteries, the potential of $\mathrm{Li/Li^+}$ is commonly used. The metal lithium electrode is widely established as reference electrode and a NiCu connector is used as the corresponding collector. Metallic Li-foils are also being used. Independently of the form, shielding (e.g. using Kapton) of the active area of the reference electrode is always necessary. In addition, the presence of a reference electrode modifies the kinetics and dynamics inside the cell and leads to diffusion and reaction overpotentials [38, 64].

Theoretically, the spatial arrangement of the reference electrode towards both electrodes should be the same, with equal distance and comparable ion-conductive medium quantities in-between. This is, however, impossible since the reference electrode needs to be physically placed on either side of the separator. If the reference electrode is placed nearer to the anode, then the potential of the anode U_{anode} is measured. The potential of the cathode U_{cathode} can be calculated using Equation 3.1 [38]. The conditions with the rest period as for the Open Circuit Voltage (OCV) measurement also apply here.

$$U_{\text{cell}} = OCV_{\text{cell}} = U_{\text{cathode}} + U_{\text{anode}} \tag{3.1}$$

Therefore, only one potential is measured. The other one is then derived using the OCV.

3.2.1.3 Temperature

As presented in Section 2.4, many of the danger and abuse scenarios inside a LiB cell are manifested by internal heating. Since the SoA suggests that a temperature sensor is only available at the module level, this results in a gradient in temperature between the physical position of the hazardous event and the placed sensor, which leads to a delay in issuing the necessary warning. With the proposed CSC, and with a cyclic, reliable, and precise measurement of the temperature, the sensor output will much sooner exceed the defined threshold and deliver the necessary warning before the occurring of irreversible damages [22].

Better yet would be a complete “skin” of temperature sensors. In fact, the temperature is not constant all over the cell: the part closer to the electrodes connectors is known to be a hotter spot than the lower part of the cell. In addition, the cathode is generally hotter than the anode [65]. Several sensors are needed to cover the complete temperature profile of the cell. These temperature sensor(s) need to accurately cover the automotive range (−40 °C to 125 °C) [66].

Temperature measurements can also be indirectly relevant to measurements of other physical quantities. For example, the look-up tables of OCV are generally generated in dependence of the temperature and the load current. The measured OCV values are therefore more meaningful when combined with information on the temperature and the load at the time of measurement. Additionally, all electrical sensors and elements have a certain Temperature Coefficient. A precise measurement of the temperature is necessary to compensate for the temperature dependency and extract a more accurate output of the sensed quantity [22].

3.2.1.4 Pressure

Different definitions of a pressure sensor in the LiB context are distinguishable.

First, pressure can stand for the surface pressure (measured in Pa or in N/m), which can be seen on the adjacent edges and surfaces of pouch or hard-case prismatic cells when closely stacked inside their respective modules. To monitor their breathing effect (See Section 2.3), a skin of pressure sensors can be placed at the wall surfaces of cells from the inside.

Second, the pressure can stand for hydrostatic pressure (measured in bar) inside the LiB cell. At high temperatures (between 80 °C and 100 °C), several components of the battery electrolyte begin to boil, creating and releasing gases. The pressure in the cell increases. At higher temperatures (between 130 °C and 250 °C), further components of the electrodes also boil or decompose, increasing therbey the pressure inside the cell and bursting overpressure valves or pressure release mechanisms (if present). Further increase of the temperature would lead to a "thermal runaway" [67] (Section 2.4, Figure 2.10 [30]).

3.2.2 Defined quantities

3.2.2.1 State of Charge (SoC)

The SoC is defined as the ratio of the current battery capacity $Q(t)$ to the nominal battery capacity Q_{nom} representing the maximum amount of charge that can be stored in the battery cell. It is expressed in percentage according to Equation 3.2 [68].

$$SoC(t) = \frac{Q(t)}{Q_{\text{nom}}} \tag{3.2}$$

It is important information to deliver to the user (driver in the case of EVs) from which the remaining driving range can be extracted. It is equivalent to the filling level of fuel tanks in combustion engine vehicles. It is also relevant information to the BMS [69].

There are several methods to measure or estimate the SoC. A commonly used method is the Open Circuit Voltage measurement combined with the Coulomb counting method. Other estimation algorithms include fuzzy logic and Kalman filter estimation methods. Extended or hybrid versions of the mentioned methods are also applicable [68, 69].

3.2.2.2 Cell impedance and State of Health (SoH)

Following the analogy of the fuel tank in a combustion engine vehicle, a battery's "tank" effectively gets smaller with time. In fact, aging of the battery makes more of the rated battery capacity, which was available at its Begin of Life, unextractable and therefore unusable. This is expressed by a deterioration of the State of Health (SoH). The speed and rate of this degradation is dependent on environmental conditions and charge/discharge history. Figure 3.5 [5] shows a graphical illustration of the SoC and the SoH in this analogy.

The evaluation of the SoH is not straightforward though. Only the battery impedance is electrically measurable. This impedance increases along with the decrease of the battery's SoH. The battery impedance is, then again, defined in different ways (more details in

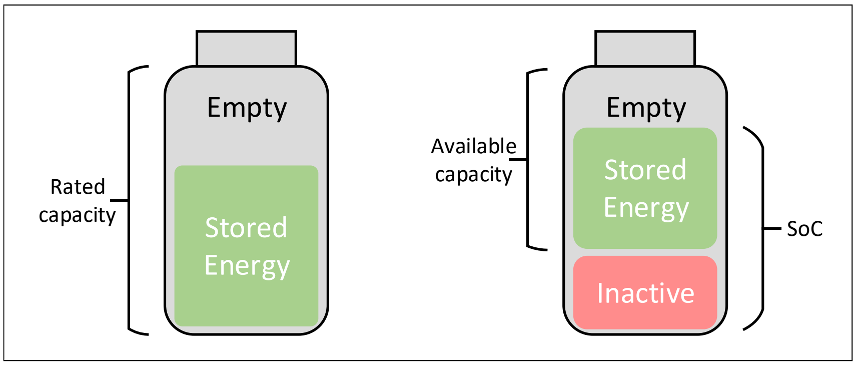

Figure 3.5: Graphical illustration of the SoC (left) and SoH (right) [5]

Chapter 5).

The inclusion of a SoH sensor in the CSC presents an added value to the monitoring system by signaling the functionality deterioration due to aging. A real-time assessment of this quantity enables a more accurate diagnosis of the battery system. Other definitions of the SoH include [70]:

- The SoH is the ratio of the capacity (amount of extractable charge) of a aged battery cell to the capacity of a new one.
- The SoH is the ratio of the State of Function (SoF) or of a selected and well-defined SoF-parameter of an aged battery cell to the corresponding one of a new cell.

3.2.2.3 State of Function (SoF)

The State of Function (SoF) is not a characteristic of only batteries or battery cells. It can be defined for all energy storage systems. Moreover, it is not specific to the battery but rather load-related, i.e. a battery cell with the same characteristics and history can be assigned two different SoF estimations with two different loads, according to the supplying functionalities that have to be delivered to these loads [70]. A general definition of the SoF of an energy system is its ability to fulfill a given task or a function correlated with a defined load. It can be presented as a percentage figure or simply reduced to a fail/pass statement [70, 71].

3.3 Proof-of-concept: a Cell Supervisory Circuit

A Cell Supervisory Circuit (CSC) was developed in this work for the purposes of proving the Smart-LiB concept. This section reports on two different approaches for the proof-of concept. In both cases, the same CSC, which is developed based on the frame conditions given by the geometry and the design of 22 A h prismatic hard-case cells, is used.

In the first approach: the integration inside the active cell housing, its mounting and protection from the battery internal chemistry as well as the extraction of the formation phase data using the communication interface was tested on several LiB cells [1].

In the second approach: the setting-up of a module out of battery cells containing the CSC and the testing of the complete communication chain to and from the BMS was tested [2]. Because of the safety issues in this case, exact geometrical replicas of the LiB cells, but without electrochemical active material, were used instead of chemically active LiB cells.

3.3.1 Cell Supervisory Circuit design

The CSC was implemented as a compact Printed Circuit Board (PCB) with the dimensions of 18×140 mm^2 and 150 µm line spacing as shown in Figure 3.6. Figure 3.7 shows the layout of the fabricated circuit.

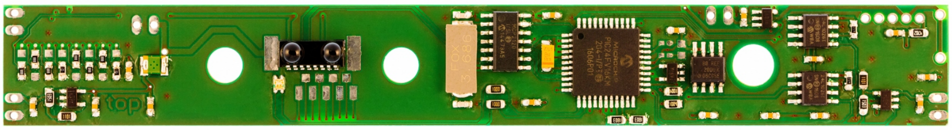

Figure 3.6: Top view of the CSC

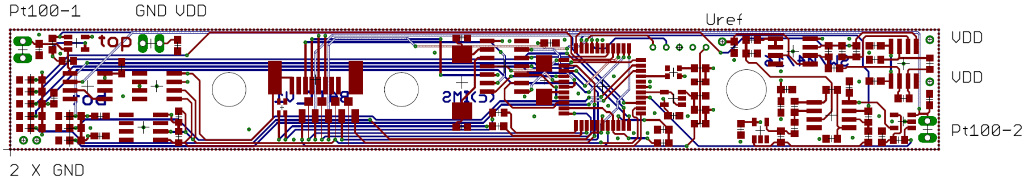

Figure 3.7: Layout of the CSC

The CSC used for this proof-of-concept consists of the following main elements:

- a digital processing unit: the controlling unit of the CSC
- sensors: sensors of cell voltage, reference voltage and temperature are used
- a communication interface: Infrared (IR) optical communication is used
- Data storage elements: commercial EEPROM memory devices.

Every CSC and hence every cell has a specified and unique address, which can be set per software using the digital processing unit, or per hardware, so that each prototype is individually addressable. To set the address per hardware, as many digital inputs as the necessary bits to code the address need to be allocated at the micro-controller. By hardwiring these inputs to SUPPLY (digital 1) or to GND (digital 0) using SMD 0-Ω

---

[1] This was conducted in cooperation with Zentrum für Sonnenenergie- und Wasserstoff-Forschung Baden-Württemberg (ZSW-BW) and was (partially) published in [32].

[2] This was (partially) published in [22]

resistors, a binary coding of the address is realized. A total of 8 inputs and therefore 8 bits are available to code the address. Since the addresses (00000000) and (11111111) are not permitted, a total of $2^8 - 2 = 254$ addresses are available.

3.3.1.1 The digital processing unit

A 44-pin general-purpose commercially available microcontroller in a compact SMD package was chosen as the digital processing unit of the CSC. The selection criteria for this device included: the possibility of in-circuit programming, the low power consumption, the availability of an on-board integrated 12-bit Analog-to-digital Converter (ADC) and the large range of operational supply voltage (starting from 1.8 V) [72].

The microcontroller fulfills several tasks. First, some of its analog channels are connected and used to detect and measure the analog outputs of the sensors. The controller then converts the measurement outputs to the digital form using its internal ADC.

Second, it communicates (using an I2C interface) and manages the writing and reading of the data storage elements, which save sensor measurements in the early life stages of the LiC together with a time stamp in milliseconds resolution. Therefore, the microcontroller operates an internal timer.

Third, the microcontroller communicates with the commander unit (part of the BMS) using a Universal Asynchronous Receiver-Transmitter (UART)-compatible Infrared (IR) optical communication interface. It receives cyclic or sporadic inquiries, and commands and responds with measured data.

The design, fabrication, assembly of the CSC and the programming of its microcontroller were carried out in this work. The microcontroller's tact is given by an external crystal oscillator. The algorithm operates according to 3 different operating modes: System initialization, Data logging and External communication.

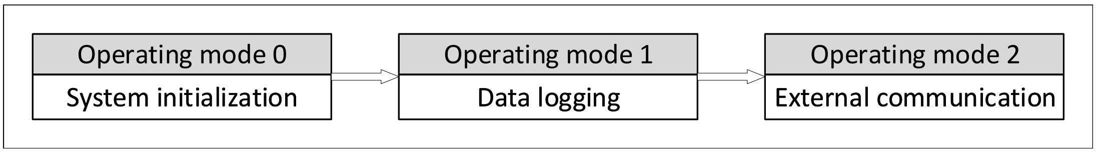

Figure 3.8: The CSC operating modes

Operation mode 0: System initialization When the current flows into the cell for the very first time (formation step, Subsection 2.2.1), the system initialization phase is activated. The internal device resources of the microcontroller are then initialized. These include:

- the internal oscillator
- the configuration of the microcontroller pins (Figure 3.9, extracted from [73])

- the internal ADC
- the Interrupt Manager
- the internal operational amplifier
- the I2C communication interface (to communicate with the EEPROM elements)
- both available UART interfaces, one of which is connected with an Infrared transceiver through an asynchronous UART/IrDA-Encoder/Decoder (More on the IR transceiver and the IrDA communication protocol in Subsection 3.3.1.4).

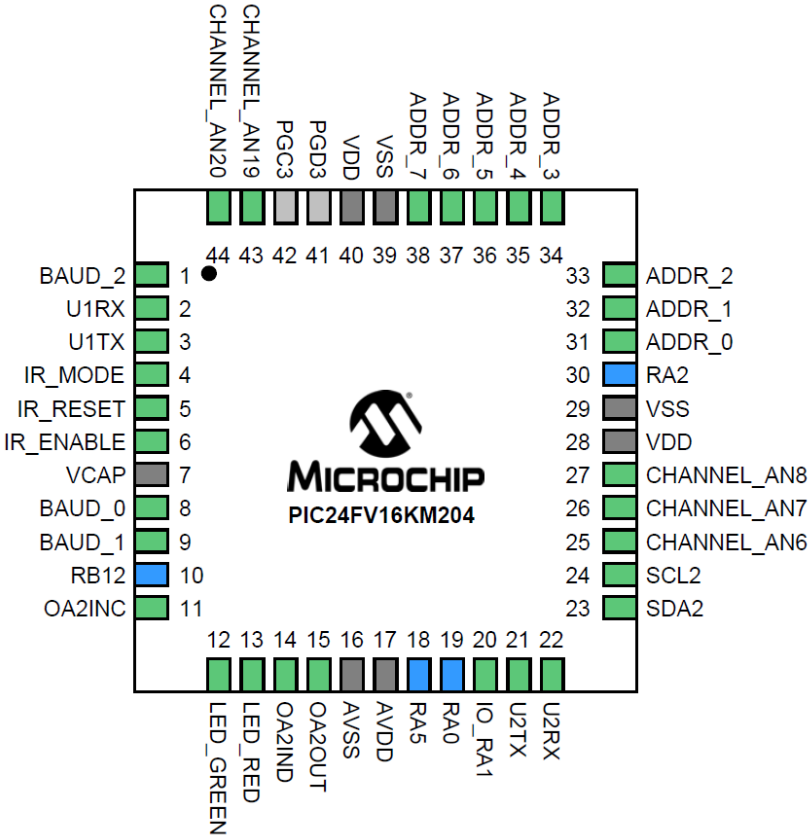

Figure 3.9: The microcontroller pin configuration programmed and used in this work (extracted from [73])

The system conducts a self-test and brings itself to a “Safe State”, by waiting for a stable supply voltage of at least 1.8 V (Minimum supply voltage required by the microcontroller to operate in a stable manner). Also, the own hardware-set address as well as the IR communication baud rate are read out of the 0-Ω resistors and recorded by the software. The internal timer is started.

Operation mode 1: Data logging As soon as the system initialization and the self-test are completed, the microcontroller switches automatically to the Data logging mode. The CSC then records and saves the sensor data in the local EEPROM elements (More in Subsection 3.3.1.3). During this phase, the green LED indicator is blinking (See Pin 12 in

Figure 3.9). The recorded data sets contain time information in seconds and milliseconds, as well as sensor data of cell voltage, reference voltage and temperature values (2 values, more in Subsection 3.3.1.2). The internal Timer (not a Real-Time Clock and Calendar) is used for this purpose.

The aim of the Data logging phase is the recording of the happenings inside the LiC during the first critical operational phases (formation cycle) in the local memory devices (EEPROM elements) together with a time stamp. This data is then available at the cell level and can later be retrieved by the BMS. A new data set is started every time a voltage difference of at least 5 mV is detected or whenever 20 s have passed, whatever occurs first. The typical progress of the cell voltage is then recorded. The Finite-state machine (FSM) of Operation mode 1 is shown in Figure 3.10.

When the voltage measurement reaches the value of 3.5 V, the recording frequency is reduced to one data set recording every minute. The cell is namely approaching the expected plateau at the end of the formation phase. The data logging phase is completed when the available memory is full or when the cell voltage reaches the plateau of 4.2 V. The probability of data loss because the memory is full is, however, very low, since the implemented memories are sufficient for several days of data measurements.

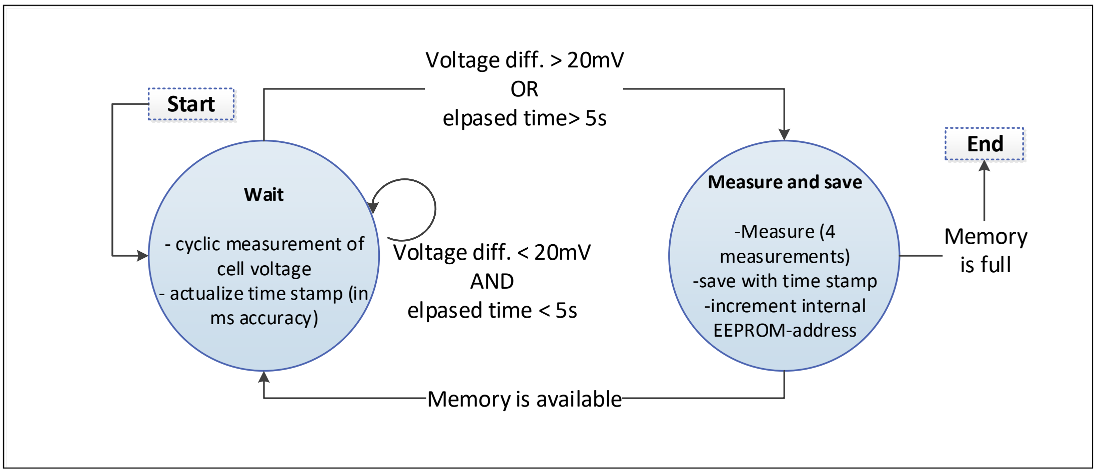

Figure 3.10: The FSM of Operation mode 1

Operation mode 2: External communication When Operation mode 1 is completed, the microcontroller (and the CSC) enters Operation mode 2. The green LED is permanently On. This indicates that the CSC is now able to receive commands and send data through its IR communication interface. The received commands from the commander unit are encrypted. So are the data packages sent back. In case a communication error is detected, or the received command or inquiry is unintelligible, the red LED blinks and no data is communicated. An error code is communicated instead. In the error free case, the CSC sends back, depending on the received command, the requested data (a real-time measurement of a voltage or a temperature). A reserved command triggers the reading out of the EEPROM elements and the acquisition of the formation phase data. The FSM of Operation mode 2 is shown in Figure 3.11. The corresponding FSM of the commanding unit (See Figure 3.3) is shown in Figure 3.12.

Table 3.1 decrypts the commanding unit (master) commands and the corresponding CSC (slave) answers in this operating mode.

Table 3.1: Master commands and corresponding slave responses in Operation mode 2

Command from Master		**Answer/Response from Slave**
Command code	**Requested data/action**	
0000	Reset	No Answer, CSC system reset
0001	Temp 1	Sensor data of Temp 1
0010	Temp 2	Sensor data of Temp 2
0011	Cell voltage	Sensor data of the cell voltage
0100	Not used	Error
0101	Not used	Error
0110	Reference voltage	Sensor data of the reference voltage
0111	Not used	Error
1000	Not used	Error
1001	Not used	Error
1010	Not used	Error
1011	Not used	Error
1100	Not used	Error
1101	Not used	Error
1110	Not used	Error
1111	Read out memory content	Data stream from EEPROMs

In Table 3.1, sensor data from four different sensors are decrypted:

- Temp 1: the temperature at the anode, measured with a Pt-100 measurement resistor, value detected with Analog channel AN 6, Pin 25 (See Figure 3.9)
- Temp 2: the temperature at the cathode, measured with a Pt-100 measurement resistor, value detected with AN 7, Pin 26
- Cell voltage: value detected with AN 8, Pin 27
- Reference voltage: value detected with AN 20, Pin 44.

The data packages exchanged between Master and Slave are compatible with the UART communication protocol. A total of 10 bit pro Byte (=one data package) is received. Start Bit and Stop Bit are equal to 0 and 1, respectively, and are set by the microcontroller. The Parity Check code is set to even parity. It is computed and added at the end of the data package by the user.

The Data Direction (DD) is one convention bit:

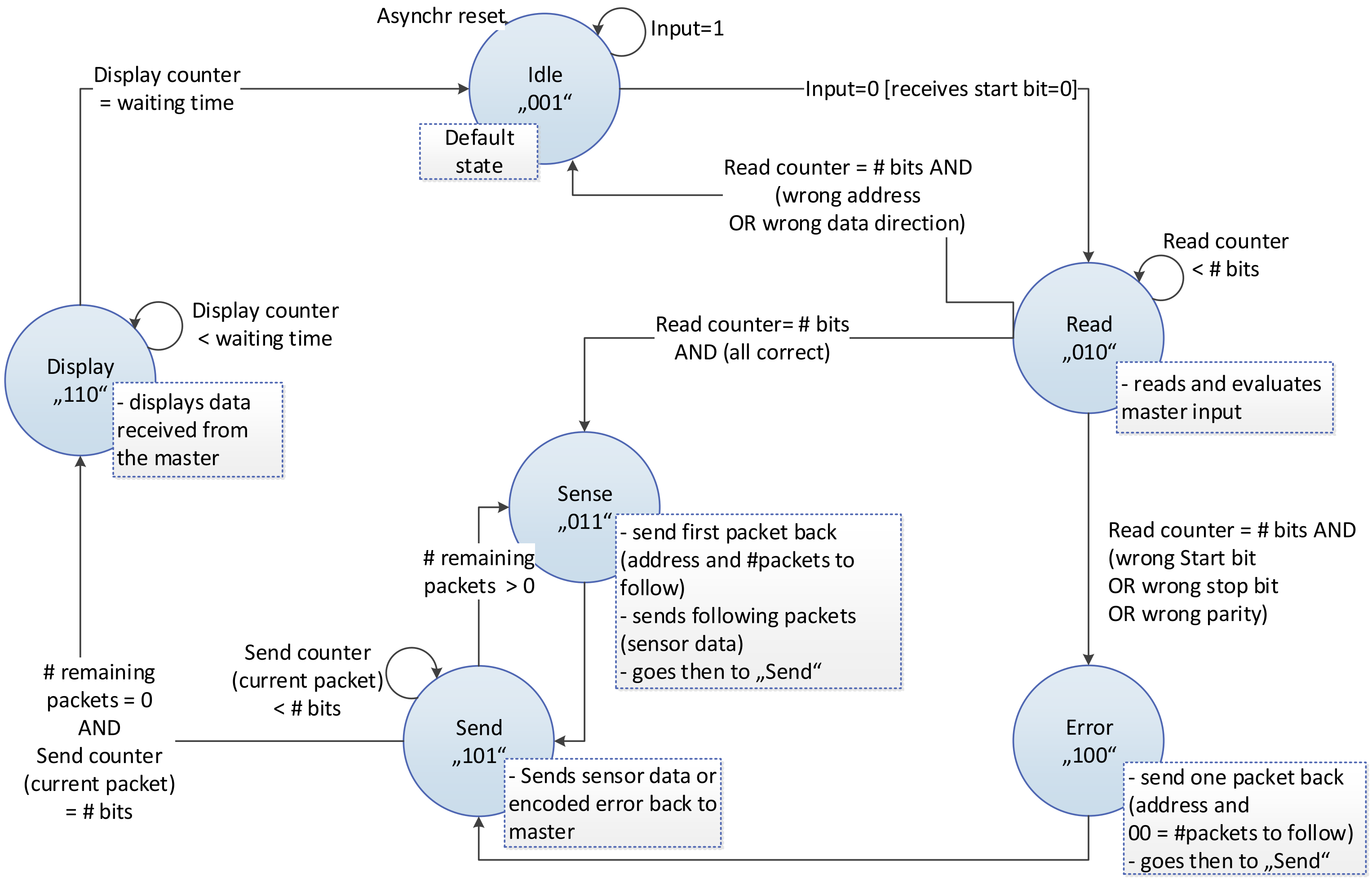

Figure 3.11: The FSM of the CSC (slave) in Operation mode 2

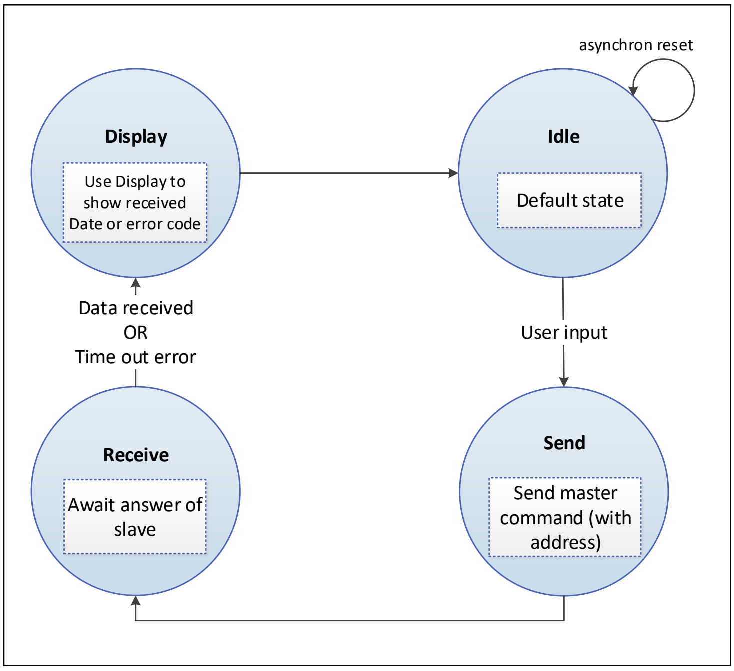

Figure 3.12: The FSM of the commanding unit (master) in Operation mode 2

- 1 stands for a data package going from Master (here commanding unit of the BMS) to Slave (here the CSC, or more precisely its microcontroller)
- 0 stands for a data package going from Slave to Master.

This convention is also used to respond to the commanding unit with measurement results. Several data packages are needed to cover the encoding of the sensor measurements (See also Subsection 3.3.1.2).

The following tables decrypt the bits of the different bytes used to communicate between Master and Slave. The Master sends a total of 2 bytes (Tables 3.2 and 3.3) containing the address of the cell (a total of 8 bits, numbered from [0] to [7]) and the command (as shown in Table 3.1, a total of 4 bits, numbered from [0] to [3]). For simplification purposes, only the 8 bits with information content are shown in the tables. The start bit (= 0) and stop bit (= 1) are not shown .

The Slave answers with 2 Bytes, containing its own address (a total of 8 bits, numbered from [0] to [7]) and an answer (a total of 4 bits, numbered from [0] to [3]). The address necessarily corresponds to the one sent by the master. The answer can contain a series of logical zeros. This corresponds to an error coding and occurs in case a not used command is received from the master (See not used commands in Table 3.1), or a parity check error is detected. If the answer contains a code > 0000, Sensor data is available to be sent. The answer code corresponds then to the number of the following bytes to be sent by the slave. The sensor data is then sent in groups of 6 bits (numbered from [0] to [5]), which will be reconstructed by the master. Since 4 bits (numbered from [0] to [3]) are available for the number of following bytes, a total of 15 Bytes (corresponding to 6×15 bits of sensor data) can follow. This is illustrated in Tables 3.4, 3.5 and 3.6.

3.3.1.2 Sensors

The temperature is measured using Pt-100-resistors at both poles of the LiC as shown in Figure 3.13. An on-board precision current source is used to detect the voltage across the resistors and therefore calculate the resistance and deduce the temperature.

Additionally, the cell voltage and the reference voltage are measured. The cell voltage is reduced by half with a voltage divider, of which the output signal is connected to an analog input channel of the microcontroller. The reduction is necessary in order to match the expected voltage range at the analog channel of the microcontroller. The original value is then regained digitally after signal processing.

The reference voltage is measured after a buffer stage. For the voltage divider as well as for the buffer structure, a high-precision CMOS Op-Amp [74] is used. Table 3.7 shows the different sensors used in this proof-of-concept as well as their accuracies and measurement ranges.

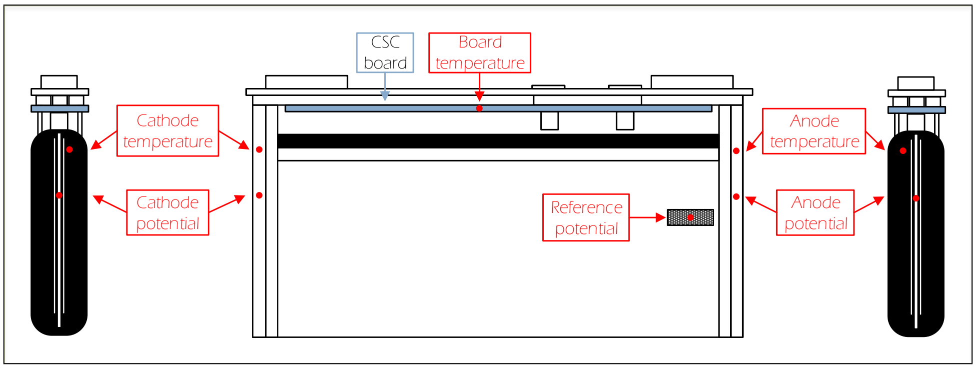

Figure 3.13: Overview of the sensors placement

3.3.1.3 Data storage elements

As previously mentioned, two local EEPROM devices are present on the CSC and used as data storage elements. They record voltage and temperature values together with a time stamp during the formation phase of the Lithium-ion cell. They communicate with the microcontroller (central processing unit of the CSC) using the I2C communication protocol with a frequency of 500 kHz. Two signal conducting lines are therefore needed (Pins 23 and 24 in Figure 3.9):

- Serial Data (SDA): the data conduction line between the master (here the microcontroller) and the slave (here the EEPROM element) to send and receive data.
- Serial Clock (SCL): The clock signal carrying line.

Table 3.2: Decryption of the master's first byte

8	7	6	5	4	3	2	1	Bit
Parity bit	DD	[5]	[4]	[3]	[2]	[1]	[0]	Position
Even parity	1	Address						Function/ Convention

Table 3.3: Decryption of the master's second byte

8	7	6	5	4	3	2	1	Bit
Parity bit	DD	[3]	[2]	[1]	[0]	[7]	[6]	Position
Even parity	1	Command				Address		Function/ Convention

Table 3.4: Decryption of the slave's first byte

8	7	6	5	4	3	2	1	Bit
Parity bit	DD	[5]	[4]	[3]	[2]	[1]	[0]	Position
Even parity	0	Address						Function/ Convention

Table 3.5: Decryption of the slave's second byte

8	7	6	5	4	3	2	1	Bit
Parity bit	DD	[3]	[2]	[1]	[0]	[7]	[6]	Position
Even parity	0	Answer: error code (=0000) or number of following bytes				Address		Function/ Convention

Table 3.6: Decryption of the slave's following bytes

8	7	6	5	4	3	2	1	Bit
Parity bit	DD	[5]	[4]	[3]	[2]	[1]	[0]	Position
Even parity	0	Sensor data						Function/ Convention

Table 3.7: Characteristics of the CSC sensors

Physical entity	**Range**	**Accuracy**	**Test points**
Temperature	0 °C to 90 °C	1 K/LSB	at anode and cathode
Cell voltage	2.5 V - 4.2 V	1 mV/LSB Offset: 0-100 mV	between anode and cathode
Reference voltage	0 V - 4.2 V	1 mV/LSB Offset: 0-50 mV	between anode and reference electrode

The internal EEPROM addresses are numbered serially: 0 to 131071 (decimal), which corresponds to 0 to 0x 1FFFF (hexadecimal). A new recording occurs every time a voltage difference of 5 mV in the cell voltage or a time lapse of 20 s is detected, whatever occurs first. Each storing process requires 10 Bytes as detailed in Table 3.8. With the available memory space on both EEPROM elements, a total of 13106 data sets (of 10 Bytes each) are recordable.

Table 3.8: Data format saved in the EEPROM

Seconds	Milliseconds	Temp 1	Temp 2	Cell voltage	Reference voltage	Sum
2 bytes	2 bytes	1 byte	1 byte	2 bytes	2 bytes	10 bytes

The implementation of a Real-Time Clock and Calendar was also a possibility. However, with a time stamp format as DD.MM.YY, HH:MM:SS for the date and time, too many data bytes are consumed. The total amount of the bytes available to save sensor measurement data is then limited, which should be avoided. Moreover, the current date is not relevant. More important is the absolute age of the cell starting from its first formation. Therefore, the time stamp is given by the implemented internal timer.

Since the maximal value for milliseconds is 999 ms, 2 Bytes are sufficient. By allocating another 2 Bytes for the seconds information, it is possible to save for a total time span of 2 Bytes = 16 bit = 65 535 s = 18 h, 12 min, 15 s, which is sufficient to record the complete formation phase. The second EEPROM (Code 11) is only then used when the first (Code 00) is full and the formation phase is still not completed.

3.3.1.4 The communication interface

The communication interface at cell level (implemented on the CSC) has to be compatible with the one available at the BMS. The SoA communication protocols in Lithium-ion batteries for HEV and EV applications consist in CAN data bus systems. These systems cause an additional weight, which is undesirable. Research effort [24, 26, 75, 76] is being invested to develop alternative communication protocols such as wireless as well as powerline systems.

The optical Infrared Data Association (IrDA) communication protocol [77] between the CSC and the commander unit is selected in this research work. The IrDA Serial Infrared (SIR) specification defines a half-duplex serial data transfer in a asynchronous system. Data transfer rates are adjustable between 9.6 kbit/s and 115.2 kbit/s. Distances up to 1 m between communication parties are allowed. In this work, this is guaranteed by the total dimensions of the battery. The IrDA SIR protocol also specifies a viewing angle of 15° on the transmitter side and between 15° and 30° on the receiver side [78]. This can be sufficiently guaranteed by a parallel placing of the cells, and therefore their viewing angles, and the positioning of the commander unit IrDA device centrally above them. Moreover, the metal of the cells housing as well as the battery system housing provides the advantage of additional reflections of the light signals.

The signal modulation is UART-conform as presented in Tables 3.2 to 3.6. According to the UART protocol, the idle state is powered at HIGH (logical one). The start bit of a data package is LOW (logical zero). Optically, logical ones (1) are modulated by the absence of a light pulse, whereas logical zeros (0) are represented by a pulse with $\frac{3}{16}$ bit duration [78]. The data transfer rate of 19.2 kbit/s is selected. The bit duration is therefore equal to 52.1 µs. Using a local oscillator to set the correct duration of bits and a UART/IrDA-Encoder/Decoder (UART/IrDA-ENDEC), the modulation in and from light pulses with the correct data rate is ensured through the hardware configuration shown in Figure 3.14 (adapted from [78]).

Since the commanding unit as well as the CSC receives and transmit data/inquiries, both should dispose of a transceiver, which assures the functions of transmission and reception. Used here is a low–power IR transceiver module compliant to the IrDA standard for SIR data communication, integrating a PIN-photodiode and an IR-emitting diode in a total front–end solution in a single package. As will be explained in the next section, the housing upper shell of the LiC needs to be modified to provide an optical window for the IR-emitting diode and the photodiode.

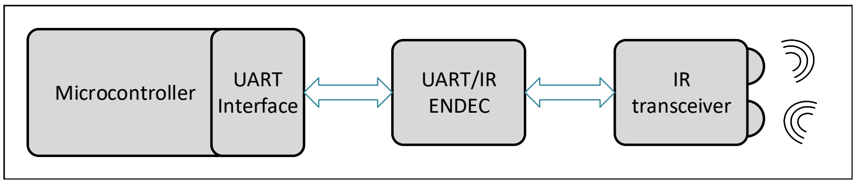

Figure 3.14: The UART-IrDA hardware configuration (adapted from [78])

3.3.2 Mounting

After the design, fabrication, assembly and programming of the CSC, it needs to be included in the fabrication process of the LiC in order to be mounted under its upper shell and before its full enclosure and formation. Therefore, the upper shell needed to be modified (Figure 3.15) from the standard design used in the manufacturing line. The modifications accommodate for a viewing window with the dimensions $10 \times 15\,\text{mm}^2$ for the IR transceiver of the CSC , as well as for the screws that will be fixating the CSC to the housing with 26 mm spacing (See viewing window with given dimensions ans screws with indicated spacing in Figure 3.15).

Corresponding holes and threads for the screws are provided on the CSC (See holes in Figure 3.7). The layout of the PCB took these holes into consideration by not leading any

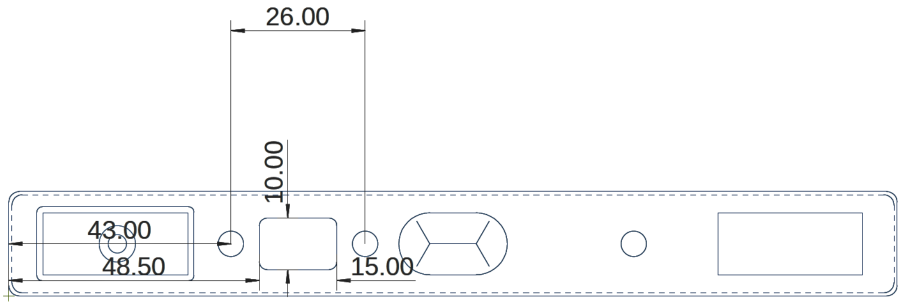

Figure 3.15: Modified upper shell housing of the cell

conductor paths through this area. Besides the screws (mechanical fixation), electrical connections are needed between the CSC and several points inside the cell. Figure 3.16 shows the exact placement and dimension of these electrical connections with cables. Figures 3.17 and 3.18 show a front and a bottom view photo of the realized mounting, respectively.

The cables include:

- Two 80 mm cables to connect the CSC to the battery poles (blue connected to GND/Anode, grey connected to VDD/cathode),
- One 120 mm cable to connect the CSC to the reference electrode (white),
- Double connections (for 4-point measurements) of the Pt-100-resistors mounted at their respective electrodes (a 20 mm connection for the Pt-100 at the anode, and a 30 mm connection for the Pt-100 at the cathode).

All cables are made of a Cu/Ag-Alloy and shielded with PTFE, except for the cable connecting the reference electrode which is made from Nickel (Ni).

Since the CSC is integrated inside the Lithium-ion cell, it is in direct contact with the active electrolyte fluid, and can therefore be damaged. Resin casting is used to protect the CSC. The complete assembled PCB is covered using a layer of liquid synthetic Polyurethane (PU) casting resin [32], which then hardens.

3.4 Evaluation of the designed Cell Supervisory Circuit

The results of the proof-of-concept are reported in this subsection following three main points: the test results of the temperature sensors plausibility inside a chemically active LiC, the successful integration of a CSC inside a Lithium-ion cell and the extraction of its formation data, and the building of a demonstrator of a Lithium-ion battery containing ten cells with integrated Cell Supervisory Circuits.

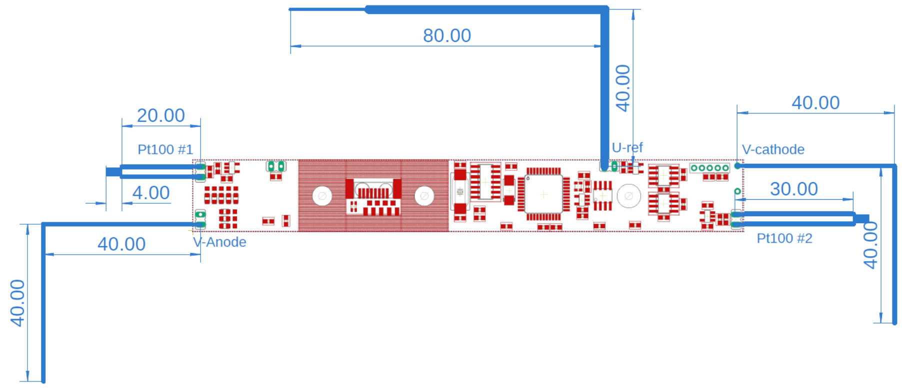

Figure 3.16: Layout of the CSC connections inside the cell

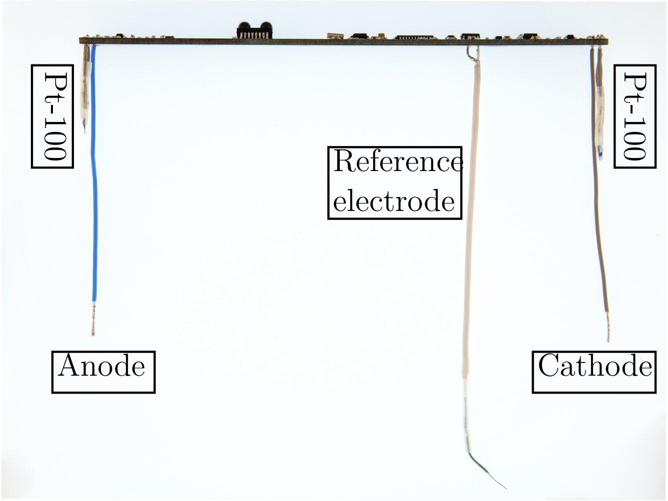

Figure 3.17: Front view of the CSC connections inside the cell

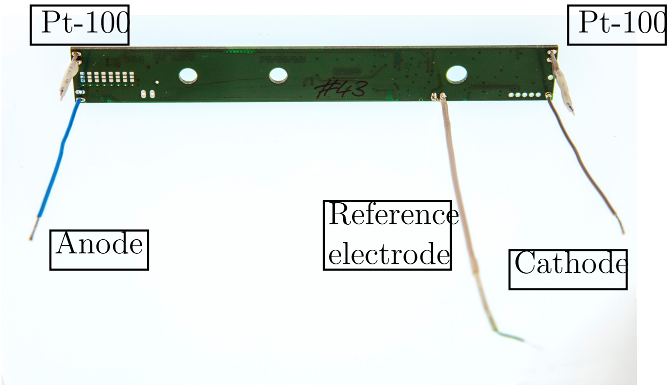

Figure 3.18: Bottom view of the CSC connections inside the cell

3.4.1 Temperature sensors plausibility

In order to ensure that the electrical functionality of the temperature measuring resistors (not covered by the resin to enable measurement) is not impaired by the harsh chemical environment inside the LiC, an investigation of the stability of the Pt-resistors inside the cell electrolyte is necessary. Therefore, a Pt-100 measurement resistor of the Class Y of the DIN EN 60751 F0.1 Norm [79] with soldered cables (protected with PVDF-heat-shrink tubes) is placed in an electrolyte bath. In order to accelerate a potential degradation of the temperature sensor, the electrolyte bath is heated up to 60 °C for 2 weeks.

The temperature sensor is then extracted from the electrolyte bath and needs to undergo a control measurement, which is conducted in a climate chamber (More details on this chamber in Subsection 4.3.1.1). A temperature sweep from -40 to 100 °C in 10 °C-steps and from 100 to 125 °C in 5 °C-steps is conducted. The resistance values of the temperature sensor at these different temperature points are then recorded (a total of 20 measurement points). Inside the climate chamber, after reaching a given temperature value, a compulsory stabilization period of 30 min is needed. This is dictated by the thermal mass of the chamber and ensures that the Pt-100-resistor has also reached this intended temperature value, and that the measurement is not falsified by an offset due to the absence of thermal equilibrium. The resistor temperature measurement curve will then be calculated from the measured resistor values at absolute temperatures. Figure 3.19 shows a comparison between the expected norm value and the actually measured resistance values at the given temperatures.

The linearization equation of a Pt-100 resistor is given by Equation 3.3 [80]:

$$R_t = R_0 \cdot (1 + \mathrm{A} \cdot T + \mathrm{B} \cdot T^2 + \mathrm{C} \cdot (T - 100) \cdot T^3), \tag{3.3}$$

wherein:

R_t is the resistance in Ω at temperature T,

R_0 is the resistance in Ω at temperature $T = 0\,°\mathrm{C}$,

T is the temperature in °C,

A is constant with $\mathrm{A} = 3.9083 \cdot 10^{-3}\ °\mathrm{C}^{-1}$,

B is constant with $\mathrm{B} = -5.775 \cdot 10^{-7}\ °\mathrm{C}^{-2}$,

C is a conditional constant with $\mathrm{C} = -4.183 \cdot 10^{-12}\ °\mathrm{C}^{-4}$ for temperatures below 0 °C, and $\mathrm{C} = 0$ for temperatures above 0 °C.

Since the back-calculation of the temperature value will be implemented in the microcontroller, using Equation 3.3 requires a high computational effort. At the cost of accuracy, an approximate, but simpler (numerically extracted) back-calculation is given by Equation 3.4:

$$T = r\left(255.8723 + r\left(9.6 + r \times 0.878\right)\right), \tag{3.4}$$

wherein:

$r = R/R_0 - 1$, with

R is the measured resistor value in Ω, and

R_0 is the resistance value in Ω at $T = 0\,°\mathrm{C}$.

Figure 3.20 shows a comparison between the calculated value using Equations 3.3 and 3.4 and the reference value of the temperature at the given resistance values.

Figure 3.21 shows the deviations of the hereby calculated temperature values from reference values. The temperatures on the y-axis of the figures on page 52 are set by the relevant temperature range for the automotive application. The measurement and calculation error is constantly under 1 °C until approximately the limit of 90 °C. The maximum error is 2 °C on the complete range.

It can be concluded that the electrolyte bath did not significantly change the accuracy of the Pt-100-resistor. Also, Equation 3.4 will be implemented in the microcontroller on the CSC and used in the calculations due to its simplicity in order to save computational power.

3.4.2 Cell Supervisory Circuit integration and formation data extraction

The production process was modified in order to account for the integration and mounting of Cell Supervisory Circuits in pouch cell with a capacity of 22 A h. Out of a total of 23 tested cells, 2 chemically active cells (cells A and B) with responsive CSCs could be produced. Cell A ist the first chemically active cell where no leakage was detected and the measurement data was extractable. Cell B was produced in a later phase, after the issues were better understood, and the process was optimized according to the learnings from previous trials.

In fact, the modification of the upper shell as presented in Subsection 3.3.2 made it impossible to apply automatic welding. Indeed, a leakage issue was detected. Instead, manual post-processing and welding of the upper shell of the cell with the rest of the cell housing was necessary. This led to a low yield.

Also, after each welding trial, the cell was powered-up and the previously saved data was overwritten. Therefore, the software was modified to leave the Operation mode 1: Data logging (See Subsection 3.3.1.1) as soon as a cell voltage plateau of 3.7 V is reached. The cells are activated by forcing a charging current and hence increasing the cell voltage until a previously defined threshold value (typically between 3 and 4.2 V) is reached.

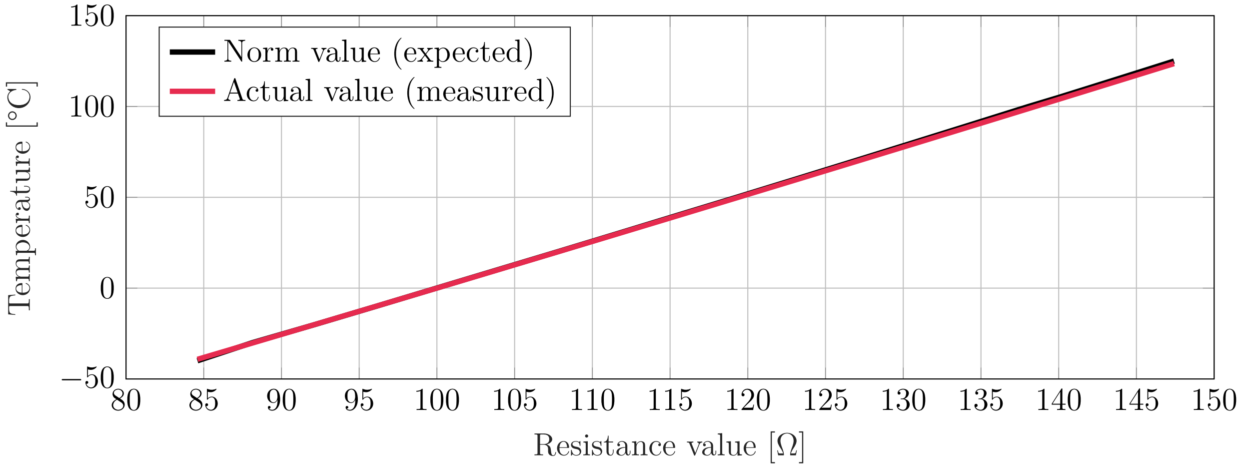

Figure 3.19: Plausibility temperature measurements of Pt-100 resistors

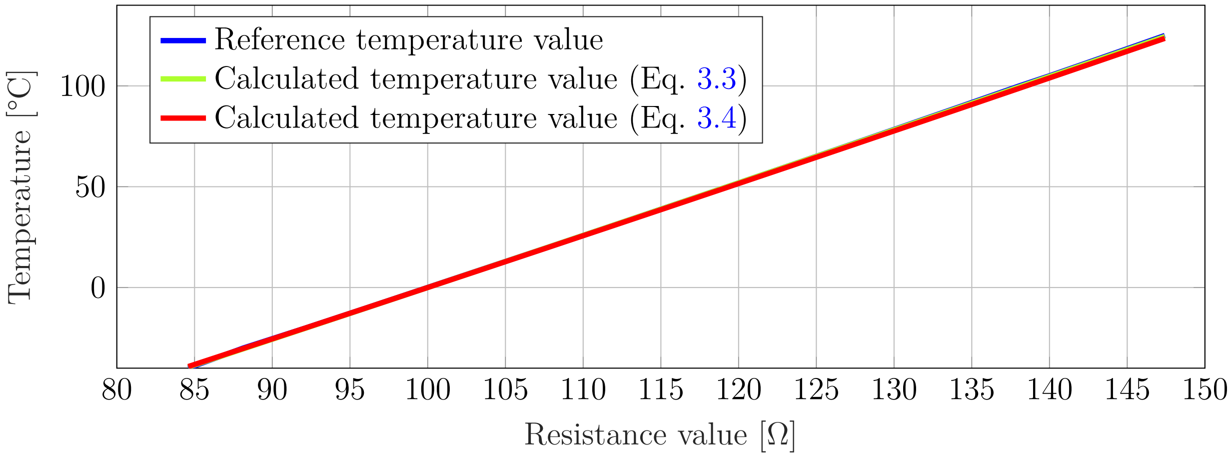

Figure 3.20: Temperature back-calculation from resistance values

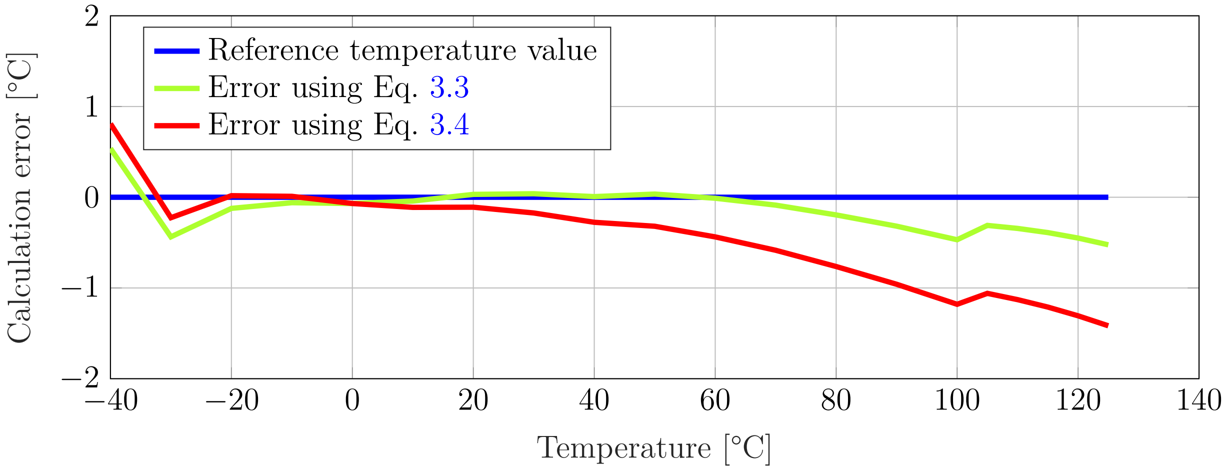

Figure 3.21: Deduction error of the back-calculated temperature values

Figures 3.22 and 3.23 show the results (voltages and temperatures) for Cell A, extracted from its CSC and compared with the external measurement of the formation process apparatus. Figures 3.24 and 3.25 correspond to the results of Cell B. The time limit on the x-axis on all figures was set by the highest time stamp from the extracted data sets.

3.4.3 Data Measurements discussion

Comments on the reference electrode: The potential difference between the reference electrode and the anode is expected in the range from $-100\,\mathrm{mV}$ to $1000\,\mathrm{mV}$. In both cases, the achieved measurements were (starting from a time point above 1000 s) above this level. An analysis of this effect would require the opening of the cell and therefore its (partial) destruction.

Comments on the cell voltage: For Cell A, the voltage measurement shows an offset between the CSC and the external measurement. This is due to the poor concordance between the start time point of recording between both measurement systems. For Cell B, a better accordance in results between internal (CSC) and external measurement is obtained, although the first 800 s of measurement could not be extracted.

Comments on the temperature: For Cell A, an error occurs around t=50 s in the Pt-100 element delivering the anode temperature signal. The excessive signal increase cannot be explained by a physical increase of the temperature since the other two signals (cathode temperature and cell temperature in Figure 3.25) do not show a similar behavior. It is rather a signal error or a disconnection (OPEN-Status) causing a saturation of the signal.
For Cell B, a better temperature recording is obtained. The internal measurements show higher values than the external one, since the sensors are closer to the physical hot spot. Additionally, the cathode shows slightly higher values than the anode, which is expected (as presented in Section 3.2).

Comments on the cell fabrication and formation process: After the modification of the upper shell of the Lithium-ion cell (made of soft Aluminum), the laser-welding process used to seal the housing was not as effective as in the standard process. The pressure applied on the metal by the screws and the new weight minimally modified its contour, so that the computed laser pointing position was no longer accurate. Since the presence of foreign particles is not admissible inside the cells, making the sealing process crucial, a manual rework was often necessary and, in many cases, even insufficient, making

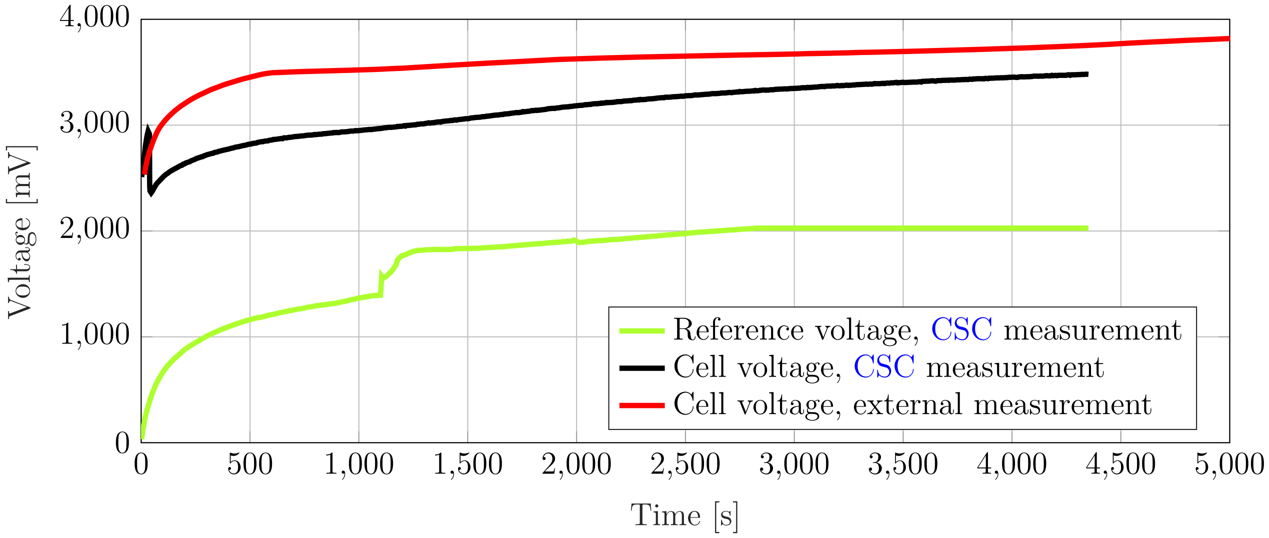

Figure 3.22: Extracted voltage measurements of Cell A

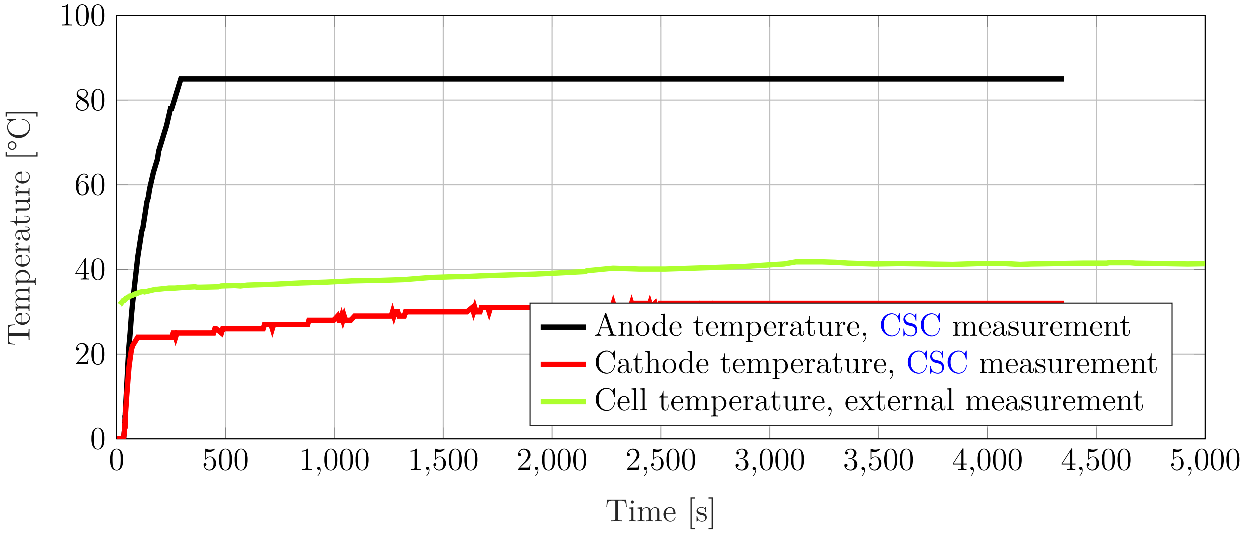

Figure 3.23: Extracted temperature measurements of Cell A

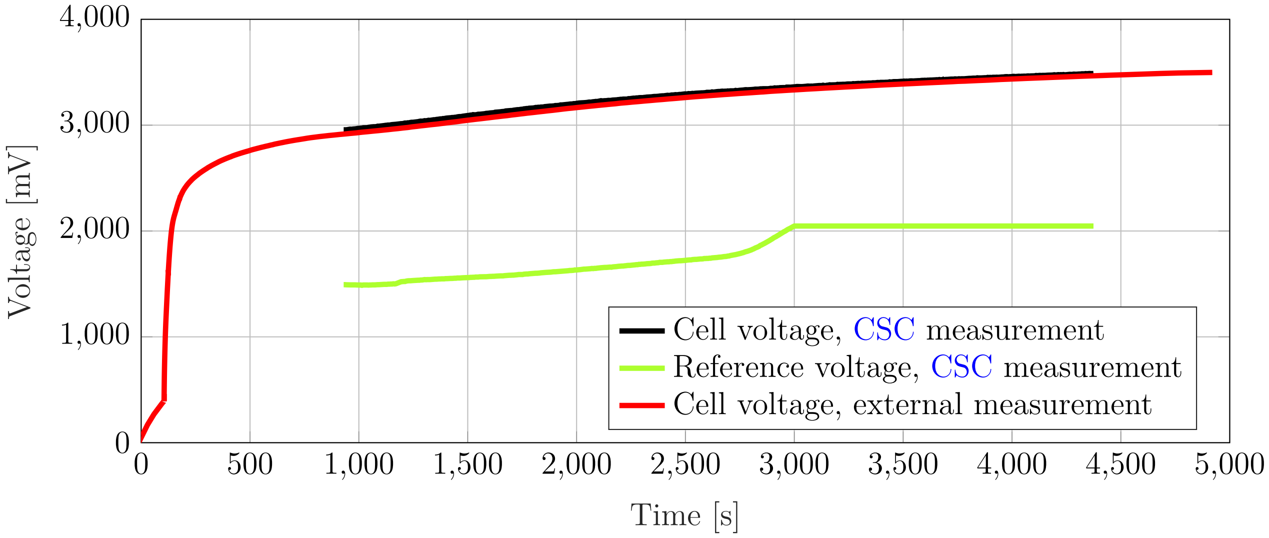

Figure 3.24: Extracted voltage measurements of Cell B

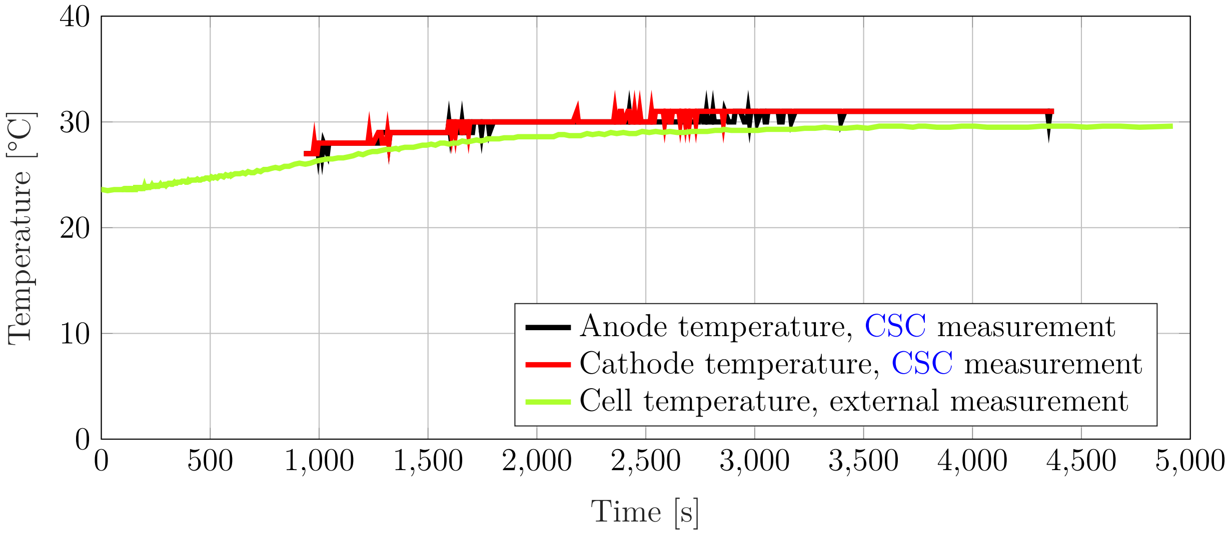

Figure 3.25: Extracted temperature measurements of Cell B

the smart cell unreliable.

Additionally, with the new (manually modified) cell design, a new filling process needed to be developed. Although full cell capacity was theoretically pursued, less volume was available for the active material. As a result, an average capacity loss of 27% was observed. In addition, after the formation process, the gas formation, and the sealing of the cell, it is left to rest for 4 h, during which the CSC continues to discharge the cell. A deep discharge leads to a wrongful reactivation of the data logging algorithm.

3.4.4 Demonstrator module of Smart-LiB cells

After the experiment of integrating CSCs into single chemically active cells, the next experiment is to build a battery demonstrator with smart cells, the same way they are found in battery systems of EVs/ HEVs. For safety reasons, no chemically active cells are used. Instead, exact geometrical replicas of the LiB cells with the dimensions 173×85×21 mm^3 were fabricated and used. An external supply powers the CSCs of the different cells at 3.7 V.

Besides, by using externally powered cells and potentiometer elements, the system limits can be tested with a wider spectrum of error and extreme scenarios, including those difficult or too risky to realize in active chemical cells. Empty cells with integrated CSC boards (pseudo-Smart-LiB cells) were combined to build a 10-cell battery pack as shown in Figures 3.26 and 3.27 (with housing and potentiometer control knobs). Figure 3.28 shows the complete system of the battery with the Smart-LiB commander (commanding unit playing the role of a BMS).

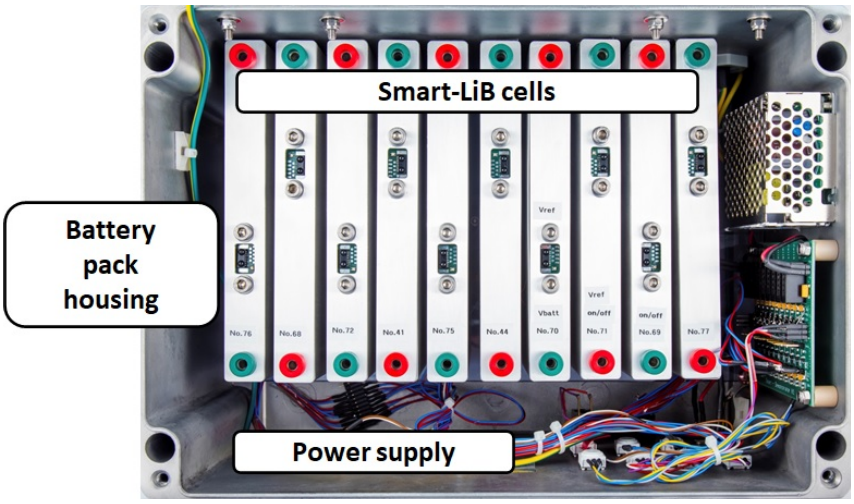

Figure 3.26: Battery pack with 10 pseudo-Smart-LiB cells

In fact, the demonstrator system consists of three parts: the battery unit (Aluminum box with fixed pseudo-cells inside), the reading unit (Smart-LiB Commander) and a reading

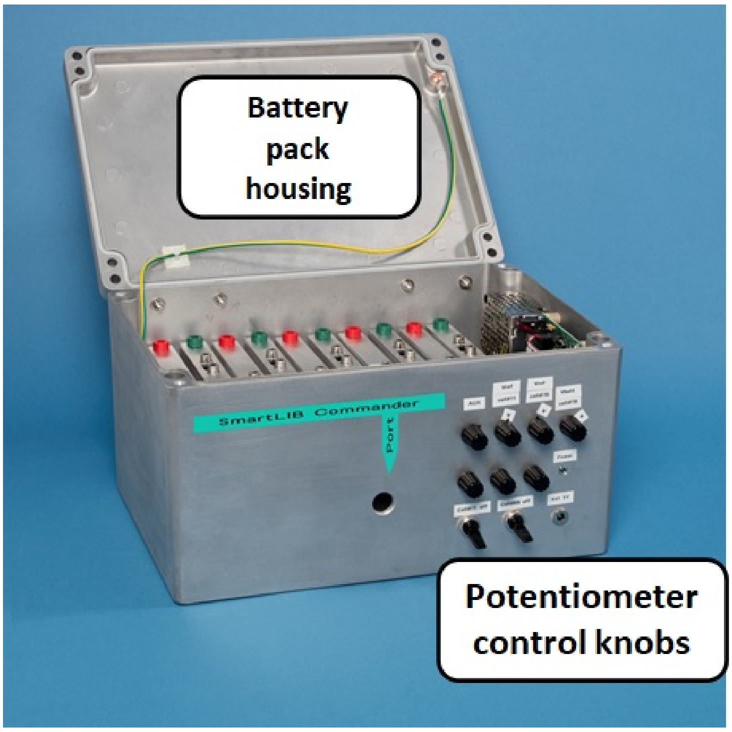

Figure 3.27: Housing of battery pack with 10 pseudo-Smart-LiB cells

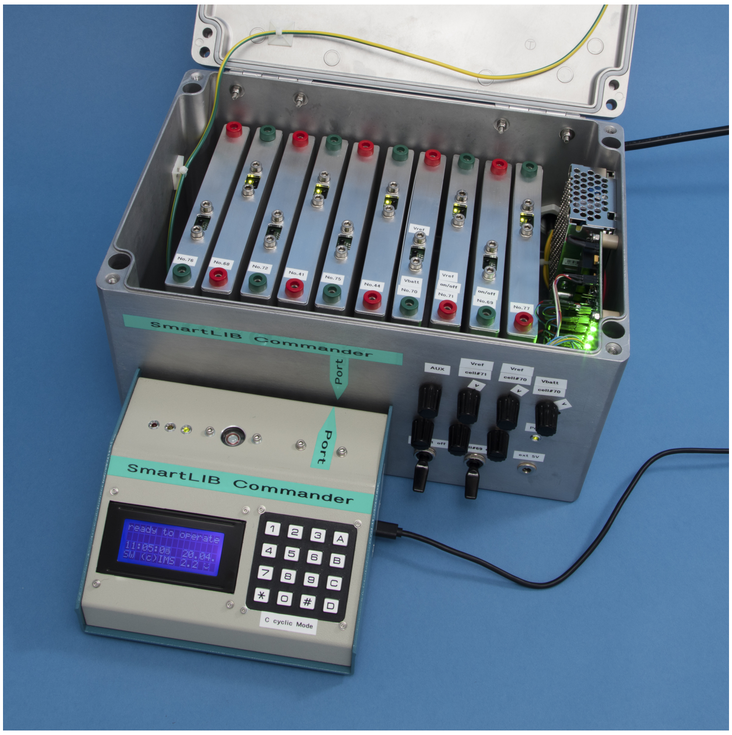

Figure 3.28: Battery pack with Smart-LiB commander

software on the laptop realized in the development environment "Processing" [81]. The Smart-LiB commander is powered by the laptop through a USB connection and partially carries a function of the BMS (See Figure 3.3). Based on a commercial microcontroller and having a purely digital functionality, it represents the addressing and readout unit that addresses single cells, requests measurements of the different sensors of the CSC and reads out measured data, exactly as was described in Subsection 3.3.1.1. Cyclic as well as single addressing of cells is possible. The laptop can also take over the addressing and monitoring functions. The LCD display on the commanding unit shows the currently executed task (addressing, receiving, etc.) and its advancement status. A GUI is also implemented on the laptop in order to better visualize the different cells and their real-time measurements.

The commanding unit addresses the single cells using the same IrDA communication interface with the same baud rate (See Port opening in Figure 3.27). When the aluminum box is completely closed, it was seen that the optical information, if not directly addressed to the single transceivers of the CSCs, needs several reflections on the aluminum surfaces to be detected, which leads to longer transmission periods. A higher power of the IR radiation and/or the use of fiber optic cable reduces this effect.

3.5 Improvement possibilities of the Cell Supervisory Circuit

The following conclusions and improvements can be drawn and suggested from the experiments of integrating CSCs inside LiCs and building a demonstrator of Smart-LiB cells:

- The Smart-LiB concept to monitor the inner life of LiCs was successfully proven. A CSC containing a microcontroller, sensors, a communication interface, and local memory devices (EEPROM) elements is designed and integrated inside active cells. Relevant data of the formation phase were recorded and could be retrieved in later life stages of the cell.
- A single addressing method and a data encryption method for data exchange between the CSC and the BMS are presented.
- By using two voltage sensors and two temperature sensors, relevant physical processes of the Lithium-ion cell are recorded. However, more sensors of other physical quantities are possible as well as needed, and recommended.
- This work includes a first experiment to include a designed reference electrode inside an active Li-ion pouch cell during the production process. The measurement values were outside of the expected range. It can be concluded that the design and reading

process of this electrode and its insertion inside the cell is still not deeply understood. More research work is needed in order to obtain more relevant readings.

- The IrDA protocol was used as communication between the CSC and the BMS. This offered the advantage of not loading the battery housing with any additional weight compared to the State-of-the-Art CAN bus system.
- The insertion of the Smart-LiB CSCs into the cells caused challenges in the production process. The filling percentage of the LiC was also reduced. More test cells are needed to establish a better know-how and a higher success rate without recurring to manual rework. The frequent recurring of manual reworks and work-around kludges reduces the reliability of the cell as well as the plausibility of the results.
- It is also necessary to reduce the dimensions of the CSC and of its mechanical fixations since they caused a pressure on the external housing of the cell, which led to a frequent failure of the laser welding process. The available filling volume and the total extractable capacity were reduced as well. Once the CSC becomes available as a monolithic solution (single packaged chip), this restriction is reduced.
- The temperature sensors require an on-board current source and additional connections. They can be reduced to just one (on a monolithic solution) reducing thereby the necessary mounting. Developing a temperature sensor not relying on a constant current flow reduces the overall power consumption of the CSC.
- The starting time point of the measurements needs to be tuned more accurately in order to avoid measurement offsets and data losses. More accurate time flags should be accurately identified within the formation phase. The algorithm of the CSC should then be modified to accommodate for these flags and record happenings accordingly.
- The choice of low power elements (low-power microcontroller) was not sufficient to guarantee a low-power consumption. The presence of the quiescent current of the CSC leads to a continuous discharge, which is fatal to the cell. Specifically, the presence of an on-board precision current source, which constantly supplies the temperature measuring resistors awaiting a possible reading from the BMS should be avoided. As an improvement, another concept for a temperature sensor (a Bandgap temperature sensor) will be presented, designed, and tested in the next chapter (Chapter 4).
- The CSC can be extended to include other sensors as presented in Section 3.3.1.2, e.g. an SoC sensor and an SoH sensor (concept presented in Chapter 5).

Chapter 4

Design of a Bandgap temperature sensor

As concluded in Chapter 3, more effort needs to be put towards the complete integration of the Smart-LiB system. This chapter reports on the optimization of the sensor functions by integrating the temperature sensor and realizing an on-chip temperature measurement solution.

4.1 Working principle of Bandgap temperature sensors

Transistors are natural temperature sensors since the dependency of their metrics on temperature is well-known. However, performing single readings from a transistor output (i.e. the transistor current) is too inaccurate, since manufacturing tolerances can lead to errors up to 3 °C [82].

The Bandgap (BG) voltage reference circuit is a mature design with a temperature insensitive output obtained by combining a Complementary to Absolute Temperature (CTAT) and a Proportional to Absolute Temperature (PTAT) voltage. The combination is carried out with the adequate circuit technique (parallel or serial realization) and topology according to Equation 4.1, wherein T is the temperature, and K a temperature independent coefficient chosen properly [82, 83].

$$V_{\mathrm{BG,REF}}(T) \;=\; V_{\mathrm{CTAT}}(T) \;+\; K \cdot V_{\mathrm{PTAT}}(T)\,. \tag{4.1}$$

Figure 4.1 [84] shows a combination example of voltages wherein

$V_{\mathrm{BE},1}$ and $V_{\mathrm{BE},2}$ are CTAT voltages with different Temperature Coefficients (obtained from base-emitter voltages of different Bipolar Junction Transistor transistors as will be explained in Subsection 4.1.1),

ΔV_{BE} is a PTAT voltage (obtained from the difference of base-emitter voltages of different Bipolar Junction Transistor transistors as will be explained in Subsection 4.1.2),

V_{PTAT} is a PTAT voltage with $V_{\mathrm{PTAT}} = \alpha \cdot \Delta V_{\mathrm{BE}}$, and

V_{ref} is temperature insensitive reference voltage (obtained as in Equation 4.1).

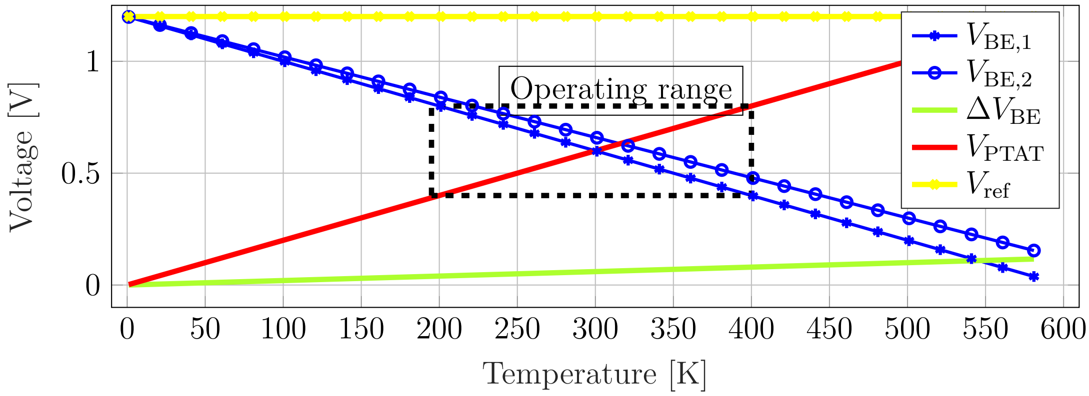

Figure 4.1: The combination of CTAT and PTAT voltages to a BG voltage is possible in the chosen temperature range [84]

Strictly speaking, delivering only a PTAT or a CTAT output is sufficient to obtain a temperature sensor. However, as shown in Figure 4.2 [82], the analog electrical signal output from the sensor undergoes analog pre-conditioning and is then digitized using an Analog-to-digital Converter (ADC). Since every ADC requires a reference voltage, this reference voltage can be provided by the BG output, hence the smartness of the design, simultaneously using the same voltages for several purposes, reducing thereby the implementation complexity, and offering a temperature independent quantity as sensor reference [82].

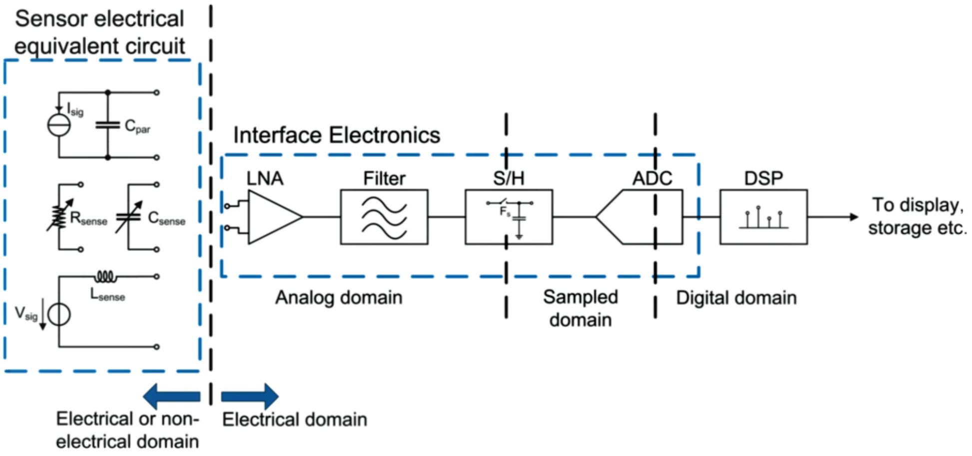

Figure 4.2: The sensor interfacing stages [82]

4.1.1 Creating a Complementary to Absolute Temperature voltage

The closest approximation of a CTAT voltage can be achieved starting from the current through a p-n diode given by the Shockley diode equation (Equation 4.2) [85],

$$I_{\mathrm{D}} = I_{\mathrm{S}} \cdot e^{V_{\mathrm{D}}/n.V_{\mathrm{T}}} \,, \tag{4.2}$$

wherein

I_{D} is the current through the diode,

$I_{\mathrm{S}} = I'_{\mathrm{S}} \cdot A$ is the reverse bias saturation current and a function of the cross-sectional area A of the diode,

V_{D} is the voltage across the diode,

$V_{\mathrm{T}} = \kappa_{\mathrm{B}} \cdot T/q$ is the thermal voltage, wherein κ_{B} is the Boltzmann constant, T is the temperature and q the elementary charge, and

$n \approx 1$ is an ideality factor, also known as the quality factor.

However, it is unlikely to find diodes (single p-n structures) in commonly accessible technologies as design devices. The more available structure in typical BiCMOS and CMOS processes is a vertical PNP Bipolar Junction Transistor (BJT) transistor (Figure 4.3a) using the p-substrate as the collector. Therefore, the collector is always grounded. By grounding the base and hence shorting it with the collector (Figure 4.3b [84]), the base-collector p-n junction is reverse biased and the current flow in the BJT is essentially one-dimensional.

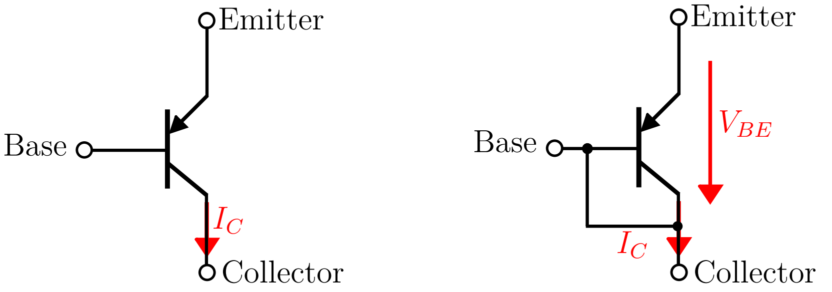

(a) The unconnected BJT **(b)** The BJT in diode configuration

Figure 4.3: BJT configurations [84]

The collector current I_{C} of the BJT is then rewritten from Equation 4.2 as a function of its base-emitter voltage V_{BE} and emitter area A_{E} for $V_{\mathrm{BC}} = 0$ and is expressed by Equation 4.3. It is then simplified in Equation 4.4 with the assumption that $V_{\mathrm{BE}} \gg V_{\mathrm{T}}$ for the considered temperature range, e.g. $V_{\mathrm{T}} = \kappa_{\mathrm{B}} \cdot T/q \approx 25.85\,\mathrm{mV}$ at room temperature (300 K).

$$I_{\mathrm{C}}|_{V_{\mathrm{BC}}=0} = I'_{\mathrm{S}} \cdot A_{\mathrm{E}} \cdot [e^{V_{\mathrm{BE}}/(\kappa_{\mathrm{B}} \cdot T/q)} - 1] \tag{4.3}$$

$$I_{\mathrm{C}} \overset{V_{\mathrm{BE}}\gg V_{\mathrm{T}}}{\approx} I'_{\mathrm{S}} \cdot A_{\mathrm{E}} \cdot [e^{V_{\mathrm{BE}}/(\kappa_{\mathrm{B}} \cdot T/q)}] \tag{4.4}$$

Conversely, the base-emitter voltage V_{BE} can be expressed as a function of the collector current I_{C} as in Equation 4.5.

$$V_{\mathrm{BE}} \;=\; \frac{\kappa_{\mathrm{B}} \cdot T}{q} \cdot \ln[\frac{I_{\mathrm{C}}}{I'_{\mathrm{S}} \cdot A_{\mathrm{E}}}] \;=\; V_{\mathrm{T}} \cdot \ln[\frac{I_{\mathrm{C}}}{I'_{\mathrm{S}} \cdot A_{\mathrm{E}}}]\,. \tag{4.5}$$

When biased at a PTAT current, this voltage can also be written (using linear approximation) as Equation 4.6 [86]

$$V_{\mathrm{BE}} \;=\; V_{\mathrm{BE,0}} - \lambda_{\mathrm{BE}} \cdot T - c(T) \tag{4.6}$$

with

$$\begin{aligned} V_{\mathrm{BE,0}} &= V_{\mathrm{g,0}} + \frac{\kappa_{\mathrm{B}} \cdot T_{\mathrm{r}}}{q}(\eta - 1)\,, \\ \lambda_{\mathrm{BE}} &= \frac{V_{\mathrm{BE,0}} - V_{\mathrm{BE}}(T_{\mathrm{r}})}{T_{\mathrm{r}}}\,, \\ c(T) &= \frac{\kappa_{\mathrm{B}}}{q}\;(\eta - 1)\;(T_{\mathrm{r}} - T + T\ln\frac{T}{T_{\mathrm{r}}})\,. \end{aligned}$$

In Equation 4.6:

$V_{\mathrm{g,0}}$ is the extrapolated value of the BG voltage at 0 K,

η is a process dependent constant, and

T_{r} is a reference temperature.

The base-emitter voltage is therefore expressed in Equation 4.6 as the sum of a linear term, with $\lambda \;\approx 2\,\mathrm{mV/K}$, which gives the CTAT behavior and a non-linear term $c(T)$, which gives a curvature behavior, resulting in a non-linearity and in an error in the total “temperature independent voltage” (Figure 4.4a [84]). Curvature correction techniques are available [82, 86, 87]. However, since the needed accuracy for the temperature sensor in the battery application context is acceptable at ≈ 1 °C, the curvature correction is not implemented in this work.

4.1.2 Creating a Proportional to Absolute Temperature voltage

The difference of the base-emitter voltages of two diode-connected BJT transistors with different emitter areas $A_{\mathrm{E,1}}$ and $A_{\mathrm{E,2}}$ biased with the same current I_{q} results in a PTAT voltage as given by Equation 4.11 (Figure 4.4b [84]). The necessary PTAT coefficient is

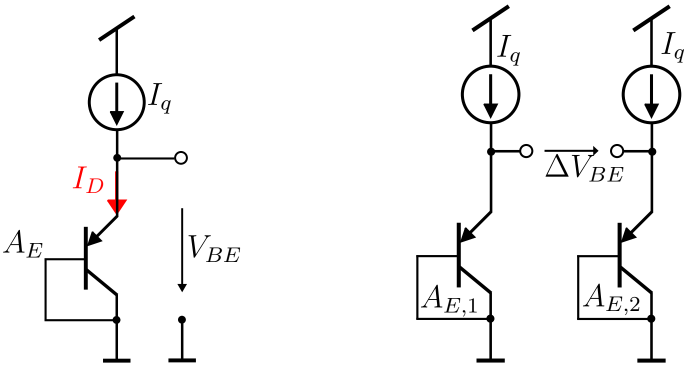

(a) The CTAT voltage **(b)** The PTAT voltage

Figure 4.4: BJT voltages dependence on temperature [84]

then obtained by appropriately chosen emitter area ratios.

$$
\begin{aligned}
V_{\text{ptat}} &= \Delta V_{\text{BE}} && (4.7)\\
&= V_{\text{BE,1}} - V_{\text{BE,2}} && (4.8)\\
&\approx \frac{\kappa_{\text{B}} \cdot T}{q} \cdot \ln[\frac{I_{\text{q}}}{I'_{\text{S}} \cdot A_{\text{E,1}}}] - \frac{\kappa_{\text{B}} \cdot T}{q} \cdot \ln[\frac{I_{\text{q}}}{I'_{\text{S}} \cdot A_{\text{E,2}}}] && (4.9)\\
&= \frac{\kappa_{\text{B}} \cdot T}{q} \cdot \ln[\frac{I_{\text{q}} \cdot I'_{\text{S}} \cdot A_{\text{E,2}}}{I'_{\text{S}} \cdot A_{\text{E,1}} \cdot I_{\text{q}}}] && (4.10)\\
&= \frac{\kappa_{\text{B}} \cdot T}{q} \cdot \ln[\frac{A_{\text{E,2}}}{A_{\text{E,1}}}] && (4.11)
\end{aligned}
$$

Figure 4.5 [84] shows the complete circuit diagram delivering a PTAT and a BG reference voltage (obtained from the combination of PTAT and a CTAT voltage) to the ADC.

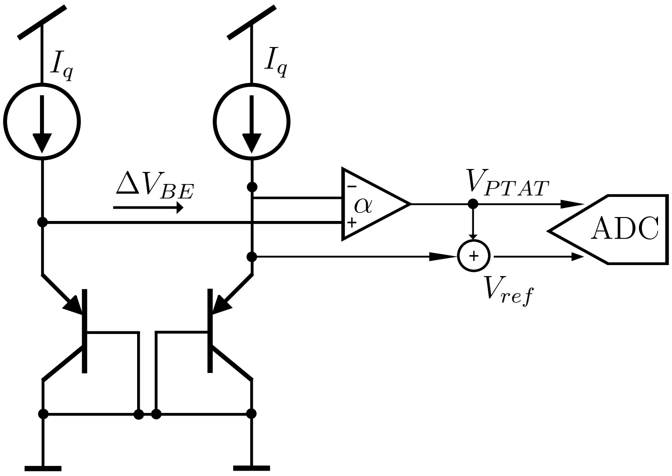

Figure 4.5: Operating principle of the BG temperature sensor [84]

4.2 Circuit implementation

4.2.1 Design technology

The design of the integrated temperature sensor is carried out at the 180 nm technology node X-FAB 0.18 Micron Modular HT HV CMOS Technology (XH018). The available BJT structures are 1.8 V vertical PNP bipolar transistor with unchangeable predefined dimensions and layout. The available emitter areas are 2×2, 5×5 and 10×10 µm^2, respectively. The emitter is embedded in a p-diffusion area, the n-well serves as base and the p-well (substrate) as collector (respectively PWELL and NWELL in Figure 4.6 [88]).

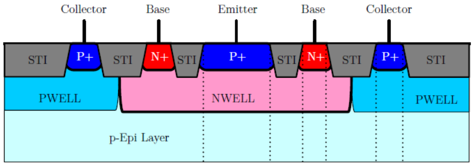

Figure 4.6: The layout of BJT in the used XH018 technology node [88]

4.2.2 Circuit design

4.2.2.1 Core of BG circuit

Since the BJT layout is fixed in the Process Design Kit, it is not possible to arbitrarily chose the emitter areas and their ratios as suggested in Equation 4.11. The workaround is to implement m parallel BJT transistors in the design which is equivalent to multiplying the emitter area by factor m. Figure 4.7 shows the complete design of the BG circuit with connections to the start-up and the Op-Amp subcircuits (See Subsections 4.2.2.2 and 4.2.2.3). Table 4.1 gives an overview of the design parameters.

Table 4.1: Design parameters of the BG circuit

Device	Type	XH018 name	Size	
Q_1	BJT	*qpvc*	A_E =10×10 µm^2	$m = 10$
Q_2	BJT	*qpvc*	A_E =10×10 µm^2	$m = 1$
R_1	Resistor	*rnp1h*	16.16 kΩ	
R_2, R_3	Resistor	*rnp1h*	150 kΩ	

In Figure 4.7, two base-emitter voltages are labeled “Y” and “Z”. Figure 4.8 shows the extraction principle of the PTAT voltage as a difference of these base-emitter voltages using an Op-Amp in a differential configuration. The signals “Y_{buf}” and “Z_{buf}” are the respective outputs of an Op-Amp in buffer configuration (not shown) using the signals

"Y" and "Z" from Figure 4.7 as inputs, respectively. The resistors in Figure 4.8 are of equal sizes and values.

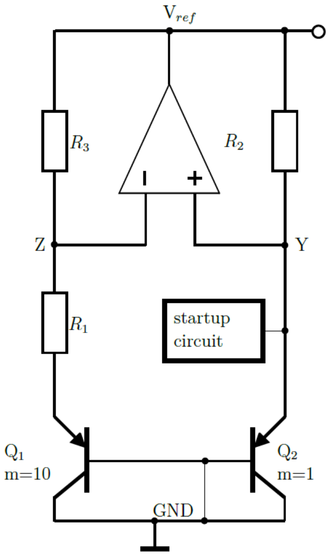

Figure 4.7: The BG core circuit [83]

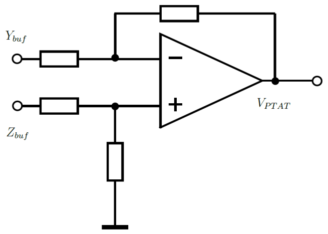

Figure 4.8: The PTAT output circuit

4.2.2.2 The operational amplifier

The chosen design is a 2-stage Op-Amp with a PMOS differential input pair and a single-ended output. Figure 4.9 shows the design details of the circuit and Table 4.2 the design parameters.

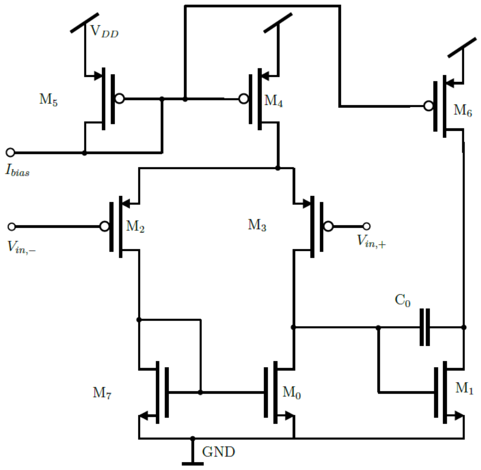

Figure 4.9: The Op-Amp circuit

The simulated gain and phase of the Op-Amp spectra are presented in Figures 4.10 and 4.11, respectively. These characteristics are accepted for the intended application.

Table 4.2: Design parameters of the Op-Amp circuit

Device	**Type**	**XH018 name**	**Size**	
M_0, M_7	N-MOSFET	*nei*	w =10 µm	l =10 µm
M_1	N-MOSFET	*nei*	w =10 µm	l =1.8 µm
M_2, M_3	P-MOSFET	*pei*	w =20 µm	l =1.8 µm
M_4, M_5	P-MOSFET	*pei*	w =10 µm	l =5 µm
M_6	P-MOSFET	*pei*	w =20 µm	l =5 µm
C_0	Capacitor	*cmm5t*	1.65 pF	

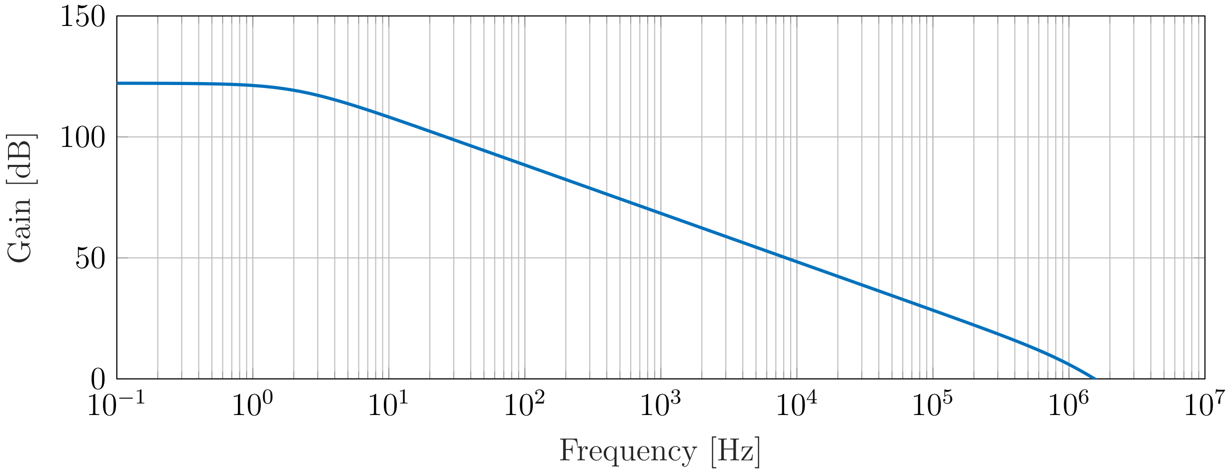

Figure 4.10: The designed Op-Amp gain spectrum

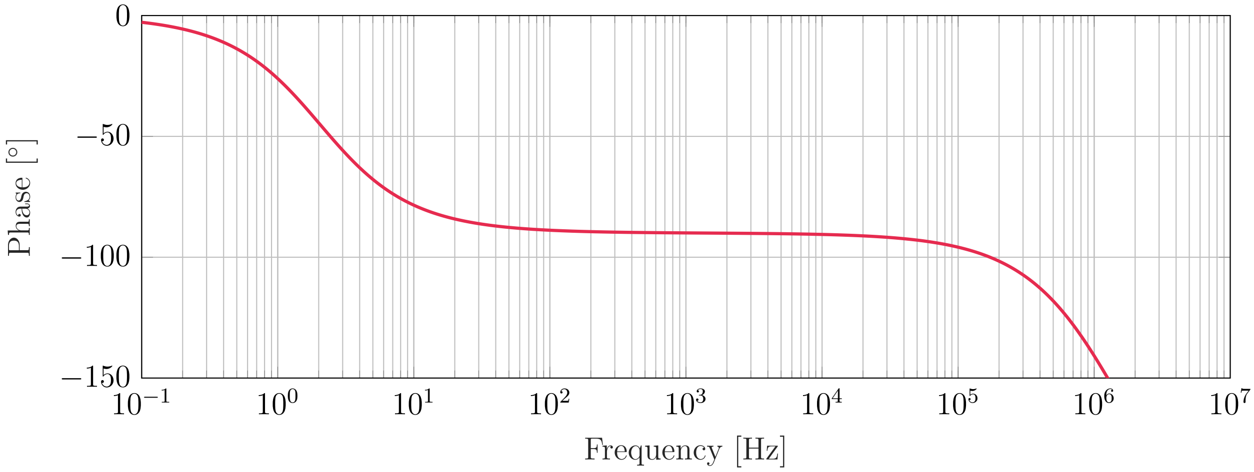

Figure 4.11: The designed Op-Amp phase spectrum

4.2.2.3 The start-up circuit

The start-up circuit is a needed add-on to conventional BG circuits. These circuits have namely two stable operation points. The zero point is indeed a stable, but undesired, operation point. The start-up circuit prevents the BG circuit from starting at undesired zero point [89–91]. After the transient behavior and once the reference circuit has reached its intended operational point, the start-up circuit switches off (current is reduced to negligible leakage current), disconnecting itself from the reference circuit and not interfering with its operation. The absence of current flow in the start-up circuit during the steady-state operation prevents additional undesired power consumption. Figure 4.12 shows the design of the implemented start-up circuit. Table 4.3 shows its design parameters.

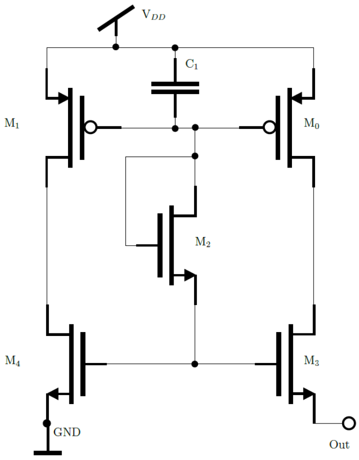

Figure 4.12: The start-up circuit

Table 4.3: Design parameters of the start-up circuit

Device	Type	XH018 name	Size	
M_0, M_1	P-MOSFET	*pei*	w =220 nm	l =180 nm
M_2, M_3, M_4	N-MOSFET	*nei*	w =220 nm	l =180 nm
C_1	Capacitor	*csf3*	33 fF	

4.2.3 Simulation results

Figure 4.13 shows the simulated BG reference and the PTAT voltage outputs over the temperature range from −20 to 100 °C.

Figure 4.14 shows the histogram of the Monte-Carlo (MC) simulations for the PTAT reference voltage with a mean value $V_{\mathrm{PTAT},mean} = 896.45\,\mathrm{mV}$ and a standard deviation $\sigma_{\mathrm{PTAT}} = 25.64\,\mathrm{mV}$.

Figure 4.15 shows the histogram of the MC simulations for the BG reference voltage with a mean value $V_{\mathrm{BG},mean} = 1.2127\,\mathrm{V}$ and a standard deviation $\sigma_{\mathrm{BG}} = 12.26\,\mathrm{mV}$.

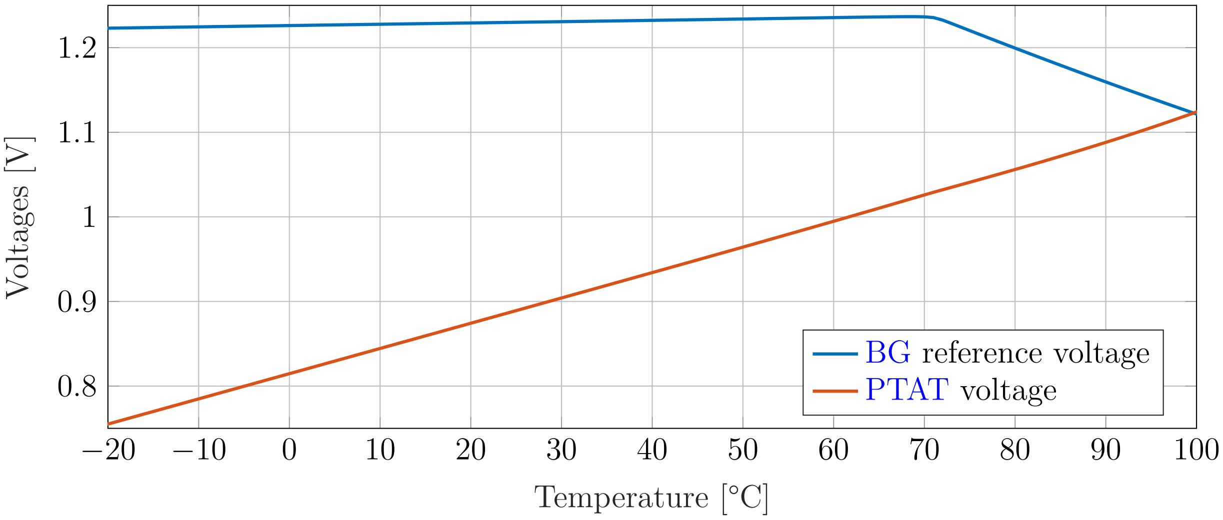

Figure 4.13: The BG reference and the PTAT voltage outputs

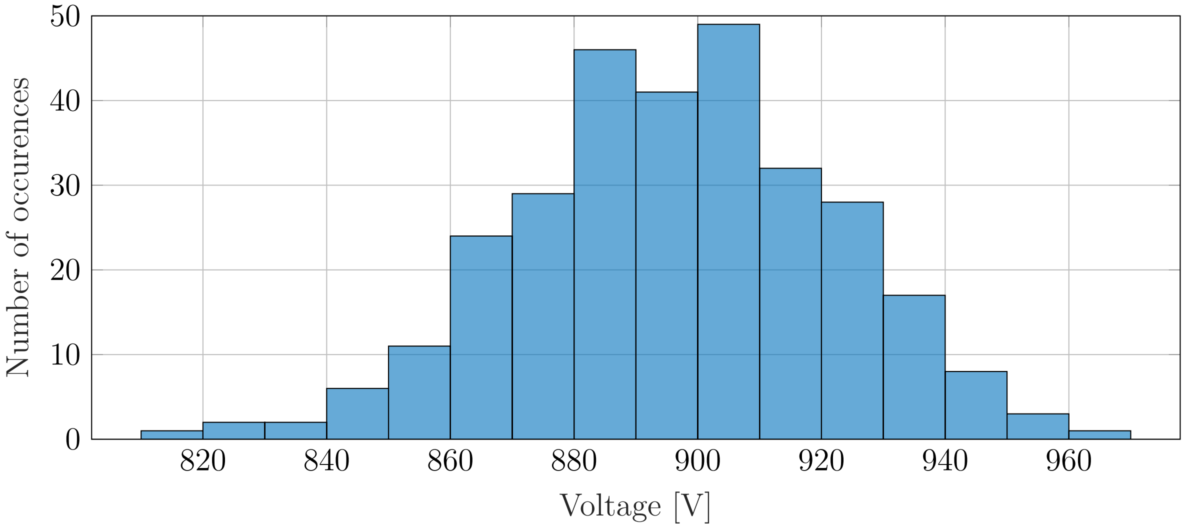

Figure 4.14: Histogram of the MC simulations for the PTAT voltage output

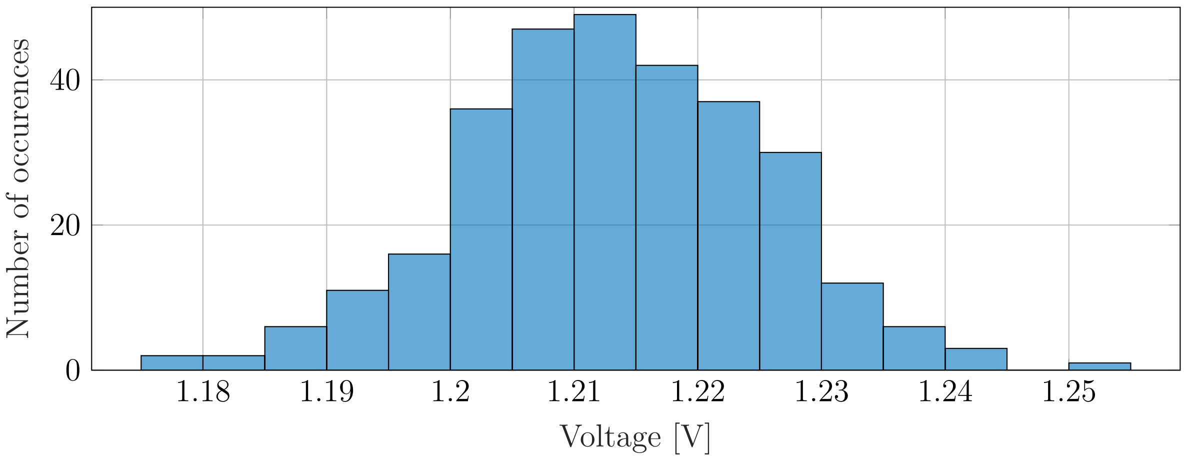

Figure 4.15: Histogram of the MC simulations for the BG voltage output

4.2.4 Layout

The complete design is taped-out on an available die size equal to 1.52×1.52 mm^2. The chip layout can be seen in the micro-graph in Figure 4.16. Figure 4.17 shows a zoom into the BG reference circuit layout. Additional dummy BJT transistors are added to the design for the purpose of better matching. Close compact placing is also applied to enhance the matching of paired devices.

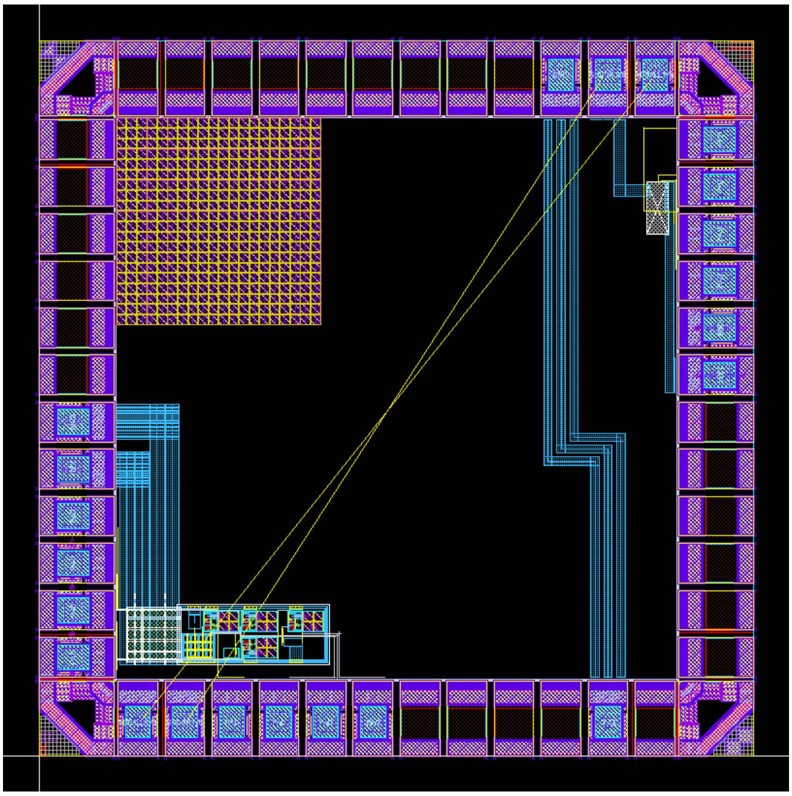

Figure 4.16: The chip layout

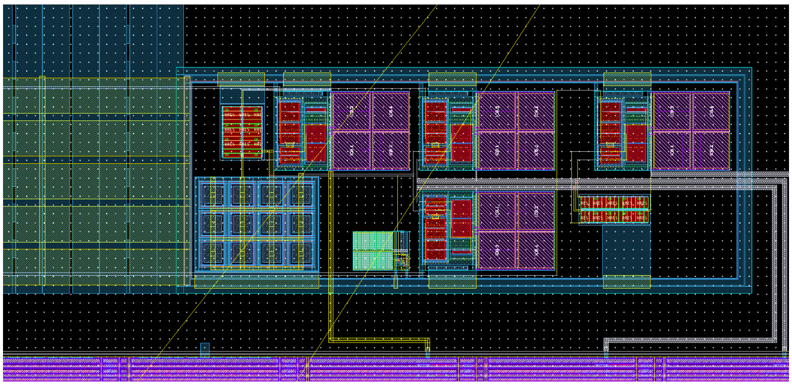

Figure 4.17: The layout of the BG circuit

4.3 Measurements

4.3.1 Measurement method

The chips need to be wire-bonded for the purposes of measurements. The bonding allows for the external biasing of the Op-Amp structures as well as the measurement of the two main outputs of the circuit: the BG reference output voltage and the PTAT output voltage. A total of 31 produced chips were bonded on a 24-pin Ceramic Dual in-Line Package (CDIP) with a 15.24 mm width (row-to-row spacing) and a 2.54 mm pitch. After the bonding, the chips were covered using a metal cover to protect the bonds and to enable a better heat flow to and from the outside environment.

At the same time, a PCB was designed for the measurements. It will be used with both measurement apparatuses (see Subsections 4.3.1.1 and 4.3.1.2). On this measurement PCB, a 40-pin DIP Zero Insertion Force (ZIF) socket [92] with Au over Ni plated pins and a 40-core ribbon cable (to contact the chip pins from outside the measurement apparatus) are soldered.

Two measurement apparatuses were used. First measurements were conducted using a climate chamber (oven, Subsection 4.3.1.1). The measurements were then reproduced using a thermostat (also called thermal bath, Subsection 4.3.1.2).

4.3.1.1 Measurements using a climate chamber

The climate test chamber Vötsch VT 4004 [93] was first used. The test chamber is a remotely programmable oven, where the measurement PCB is placed. A side opening (highlighted in green in Figure 4.18) allows for the leading through of biasing and measurement cables.

Figure 4.18: The Vötsch VT 4004 climate test chamber [93]

Since the heat transfer medium (air) inside the climate chamber has a relatively low thermal conductivity, the displayed temperature by the oven might have a gradient to the actual temperature on the measurement PCB and/or chip. Therefore, the PCB is mounted on an Al plate, where a total of 9 calibrated digital temperature sensors [94] are placed in its immediate vicinity.

A Visual Basic for Applications (VBA) script on a laptop controls the measurement sequence. The climate chamber is remotely controlled using a LAN connection. The circuit outputs (the BG and the PTAT output voltages) are measured with a digital multimeter (DMM) and transmitted using a USB connection. The digital temperature sensors are connected to an arduino board, which is remotely programmable using a USB connection as well. The sensors measurement values show small gradients (<0.5 °C). The gradient is due to their positioning and to the inaccuracy of each sensor. The average of all measurements using all 9 digital temperature sensors is calculated and considered to be the actual temperature at the chip. This average temperature constitutes the comparison value for the condition to remain or go over to the next measurement step. The measurement sequences follow the steps as presented in Table 4.4. The retrieved data is saved under the format given in Table 4.5 to be processed later.

Table 4.4: Measurement sequence using the climate chamber

Step	**Sequence**	**Description**
1	Steady State/ Start	at room temperature ≈ 20 °C
2	heat up	up to 100 °C
3	wait	for 20 s
4	cool down	down to −20 °C
5	wait	for 20 s
6	heat up	up to 20 °C
7	Stop	End of program, settling to room temperature

Table 4.5: Saved data format of climate chamber measurements

Position	**Data**	**Description**
1	time stamp	in seconds accuracy
2	current temperature	as shown by the oven
3	target temperature	set by user [90 °C, −20 °C, 20 °C]
[4:12]	digital sensors temperature	from Arduino readings
13	Reading of DMM 1	BG output voltage
14	Reading of DMM 2	PTAT output voltage

A first test included setting a target value and evaluating the time needed to reach and the accuracy of the measurement. Figure 4.19 shows a saturation of the blue curve (average of the sensors) at 88 °C when the target value was set to 90 °C. After more than 80 min, the system has reached a status of thermal equilibrium. The measurement program was not able to reach the end condition of the heating phase (Temperature >= 90 °C). It was not able to begin the cooling sequence. Therefore, the target value must be set slightly higher (or in the case of cooling slightly lower) than the desired ending condition values, for example 95 °C for 90 °C and −25 °C for −20 °C, respectively, in order to avoid endless loops in the VBA measurement program. Generally, the temperature limits on the y-axis for the figures on pages 75 to 75 as well as 77 are set by the automotive range as well as the capabilities of the measurement equipment.

Besides, important gradients between the value shown at the oven and the actual temperature on the aluminum board are seen in Figure 4.20.

Figure 4.21 shows a measurement example of a bonded chip in the climate chamber. The PTAT output voltage shows a hysteresis behavior.

Such a measurement needs more than 3 h to be completed. An alternative with a shorter measurement time and a heat transfer medium with a better thermal conductivity is presented in Subsection 4.3.1.2.

4.3.1.2 Measurements using a thermostat

The long settling time during heating/cooling towards a certain temperature value using the test chamber Vötsch VT 4004 is due to the transfer medium (air) with has a low thermal conductivity and to the relatively high inner dimensions of the chamber compared to the dimensions of the measurement PCB. Low-temperature thermostats present an alternative measurement apparatus. The Lauda Proline RP 855 [95] is used. The thermostat provides an empty bath with a volume of 8 L, that can be filled with a heat transfer liquid. Glysantin G30 [96] is used. The chip is mounted on the same measurement PCB using the DIP ZIF socket, which is then mounted inside a submersible metal housing. This housing is shown in Figure 4.22. By using a sealing ring and after the enclosure screwing of the metal housing, the submersible is then sealed against the external liquid and is placed inside the thermal bath. A ribbon cable as well as the connections cables to a temperature measuring resistor placed inside the housing in a 4-wire configuration are extracted to the outside of the bath. The temperature measuring resistor is a Pt-1000 and is considered the reference inside the submersible. It is placed in direct thermal connection to the chip and the metal housing. The use of thermal pads and a heat sink compound allows for a direct heat transfer between the heat source through the transfer medium to the chip with no discontinuities in the thermal path.

The measurement is controlled with a NI-LabVIEW program. The measurement sequence and the saved data format are similar to Table 4.4 and Table 4.5, respectively. The new measurement configuration allows for much smaller gradients between the external temperature (temperature of the heat transfer liquid measured by the sensor of the thermostat) and the internal temperature (temperature of the chip inside the metal

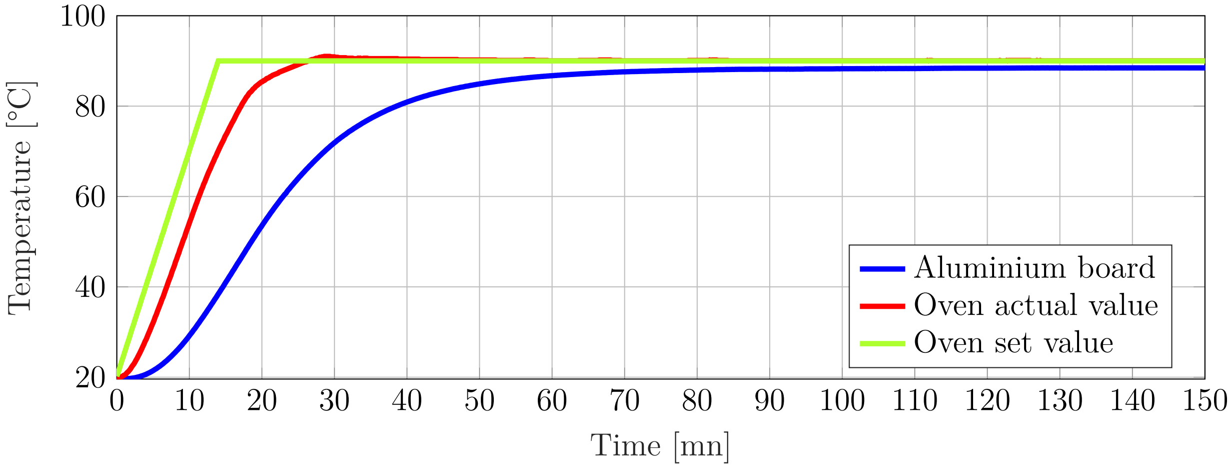

Figure 4.19: Saturation of the thermal system at 88 °C

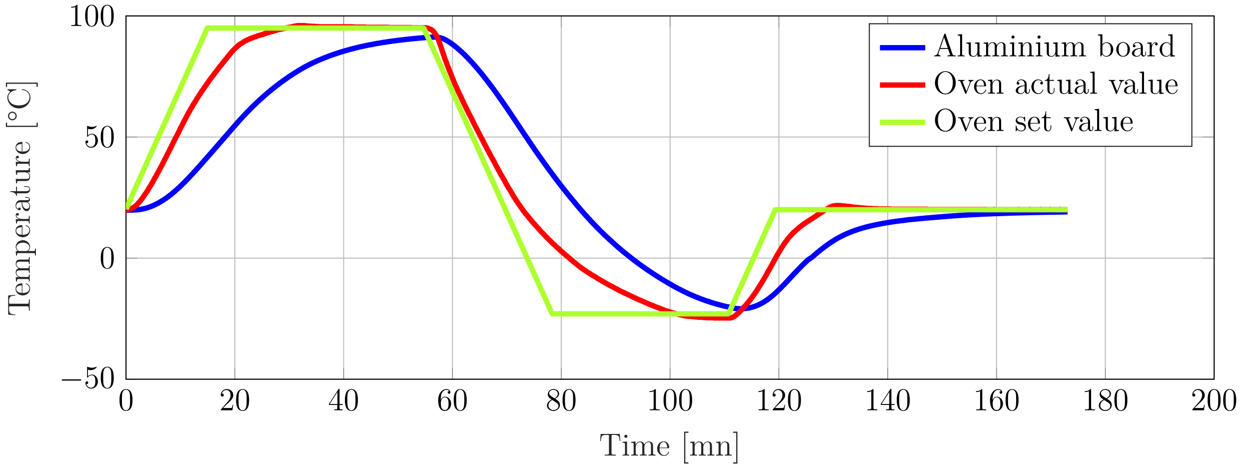

Figure 4.20: Gradient between targeted, shown and actual measurement values in the climate chamber

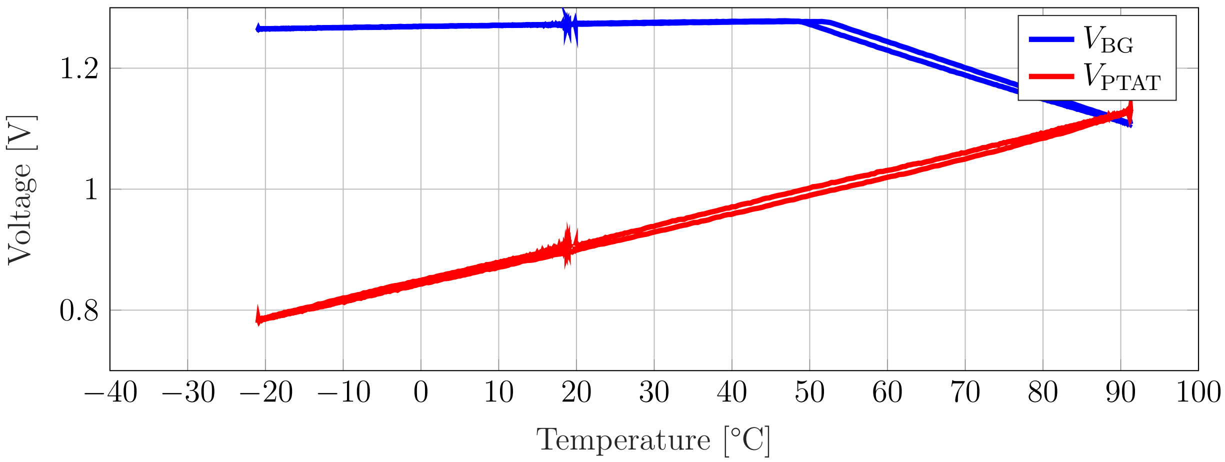

Figure 4.21: Measured PTAT and BG output voltages

(a) Mounting threads for PCB **(b)** closed submersible housing

Figure 4.22: Submersible metal housing for thermostat measurements

housing measured with Pt-1000 resistor). In addition, shorter measurement durations for the complete measurement sequence (less than 90 min vs. 3 h using the climate chamber). This measurement option is the one used to measure all 31 bonded chips and to characterize the temperature sensor.

4.3.2 Measurement results

Measurements were conducted using thermostat setup and delivered the results shown in Figure 4.23. All 31 chips show the typically expected PTAT behavior of the voltage as a function of the temperature. Important offset of several degrees °C are however seen between the measurements.

Several reasons can explain these errors. First, as shown in Equation 4.11, the PTAT coefficient is given by the ratio of the emitter ratios of the BJT transistors. Wafer-to-wafer and die-to-die variations cause mismatches in the effective areas and therefore variations in the resulting voltage (see also Monte-Carlo simulations results in Figure 4.14). Additionally, the voltage is extracted after a buffering stage using an Op-Amp with a differential input pair (Figure 4.9). The mismatch of this differential pair in the input stage also causes variations in the resulting voltage, and therefore an offset.

For the following purposes of using the chip as a temperature sensor in the Smart-LiB demonstrator (Subsection 3.4.4), the average of the linear equation is used, as given by the Equation 4.12,

$$T = a_{\text{mean}} \cdot V_{\text{sensor}} + c_{\text{mean}} \,, \tag{4.12}$$

wherein

T is the temperature result,
V_{sensor} is the PTAT voltage read by the sensor chip in V,
$a_{\text{mean}} = 315.02\,°\text{C/V}$ the and
$c_{\text{mean}} = -279.2\,°\text{C}$.

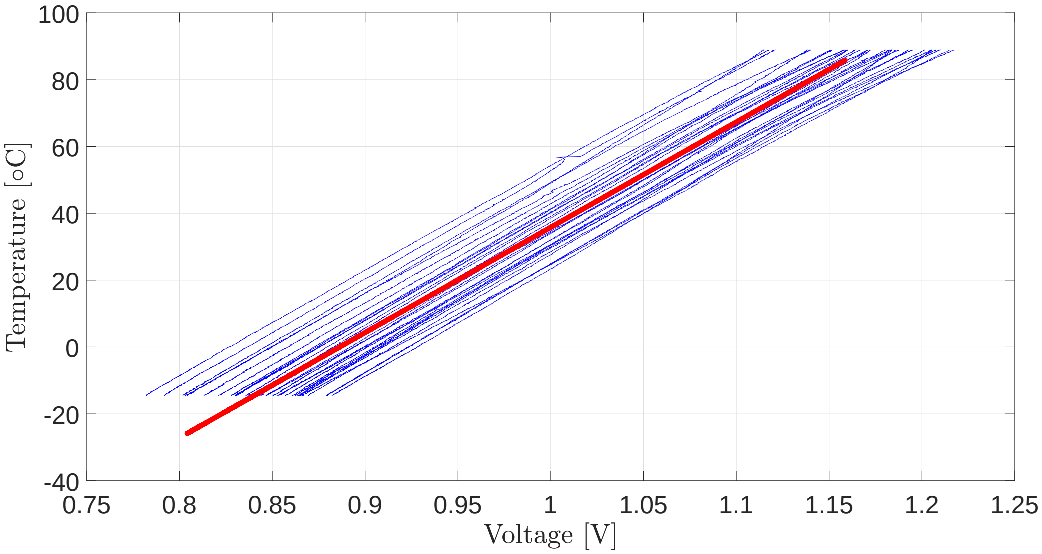

Figure 4.23: The measured PTAT outputs (average in red)

4.4 Integration into the Smart-Lithium-ion battery demonstrator

The aim from the design and fabrication of the BG temperature sensors was to replace the temperature measuring Pt-100 resistors used in the Smart-LiB as shown in Chapter 3 using a fully integrated alternative. In this section, the concept where temperature sensors are mounted close to the electrodes to monitor their thermal behavior is put into application, as shown in Figure 3.13. . Here, the chips will be bonded on flexible commercially available Polyimide (PI) foils which serve as flexible circuit boards following the Chip on Board (CoB) technique. The foils are then attached to the central CSC in order to deliver the sensor signal to the microcontroller. This represents an intermediate step towards the realization of a complete flexible system. The foil structure is presented in Table 4.6.

Table 4.6: Structure of flexible circuit boards with one layer

Layer	Thickness
PI coverlay	25 µm
coverlay adhesive	25 µm
Copper (Cu)	35 µm
PI	25 µm
	Total = 110 µm

The designed foil has the dimensions 65 $\times$25 mm^2 with a standard trace pitch of 150 µm. Figure 4.24 shows the foil design. The surface of the flexible foil was designed as ENEPIG, which is suited for Gold and Aluminum wire bonding, instead of the standard lead-free

PCB surface known as HASL. A pocket is provided (gray area in Figure 4.24) where the solder resist is not applied, to enable the bonding. The circuit on foil has 2 input signals (VDD and GND) and two output signals (the BG reference and the PTAT voltages). 8 pins connect these signals (each signal has two redundant pins for more flexibility).

A low-dropout voltage regulator is used to regulate down the voltage of the battery cell supplying the circuit on foil from 3.7 V. The chips are namely supplied at 1.8 V (See Section 4.2.1). SMD capacitors are mounted on the input and output stages of the voltage regulator for stability purposes. SMD resistors are used to bias the Op-Amp circuits on chip. Figure 4.25 shows a zoom of the chip bonded on the foil.

As explained in Chapter 3, the address of each PCB is set per hardware. A total of 8 SMD 0 Ω-resistors are hardwired to SUPPLY (digital 1) or to GND (digital 0) and realize therefore a binary coding of the address. These inputs are then connected to 8 different pins on the microcontroller where the address is read and adopted. By setting the address per software, the 8 pins are freed and can be reallocated to other functions. The foil is then attached to these the pins. The signals VDD and GND are supplied at the corresponding pins. The output voltages are then hardwired to the analog inputs of the microcontroller. The integrated ADC of the microcontroller digitizes the signal to deliver the temperature reading.

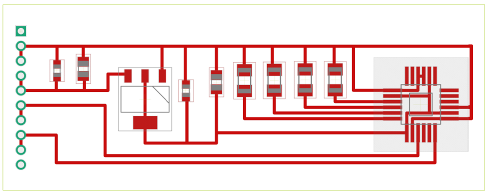

Figure 4.24: Layout of the chip boding on foil

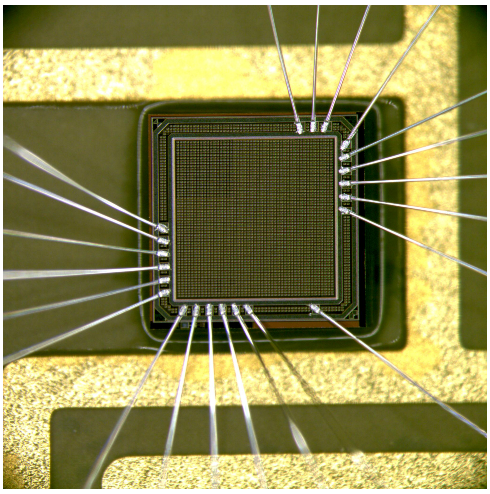

Figure 4.25: Photo of the bonded chip on foil

Chapter 5

Design and measurements of an internal resistance sensor

In this chapter, the design and evaluation of an internal resistance sensor will be discussed. This sensor can be added to the array of sensors possible to be integrated in the Smart-LiB system, as was discussed in Chapter 3.

Measuring the internal resistance of the battery is a way to evaluate the SoH of a battery. The SoH itself is, as defined in Section 3.2, used to evaluate the degradation due to aging of a battery cell and therefore its readiness to be used in an application. For example, in the context of EVs, it is considered that Lithium-ion battery cells are suitable for the application until their SoH has decreased to 80%. This is equivalent to an increase to 200% of the internal resistance value compared to the value at its Begin of Life [49].

The designed internal resistance sensor is implemented using commercially available elements first. Particularly, it examines the possibility of designing a sufficiently accurate integrated sensor with commercially available Off-the-Shelf (OTS) elements and a standard PCB design.

Before discussing the details of the designed sensor, a review of the definitions of the internal resistance/impedance is given.

5.1 The Lithium-ion battery impedance

There are varying definitions of the internal resistance of a battery, depending on the method of measurement and extraction. The following sections will describe those different definitions, from which a definition is selected to be implemented in the designed sensor.

5.1.1 The typical impedance spectrum of a Lithium-ion battery

The battery cell is a low impedance DUT. The expected value of the impedance is in the range of mΩ. Figure 5.1 [97] shows a qualitatively typical Nyquist curve (Real Re(Z) Vs imaginary Im(Z) part of impedance Z) resulting from the frequency sweep impedance measurements of a LiB cell. Quantitatively, the values depend on different factors, i.e. the temperature, the SoC, the load profile and the age [39, 98].

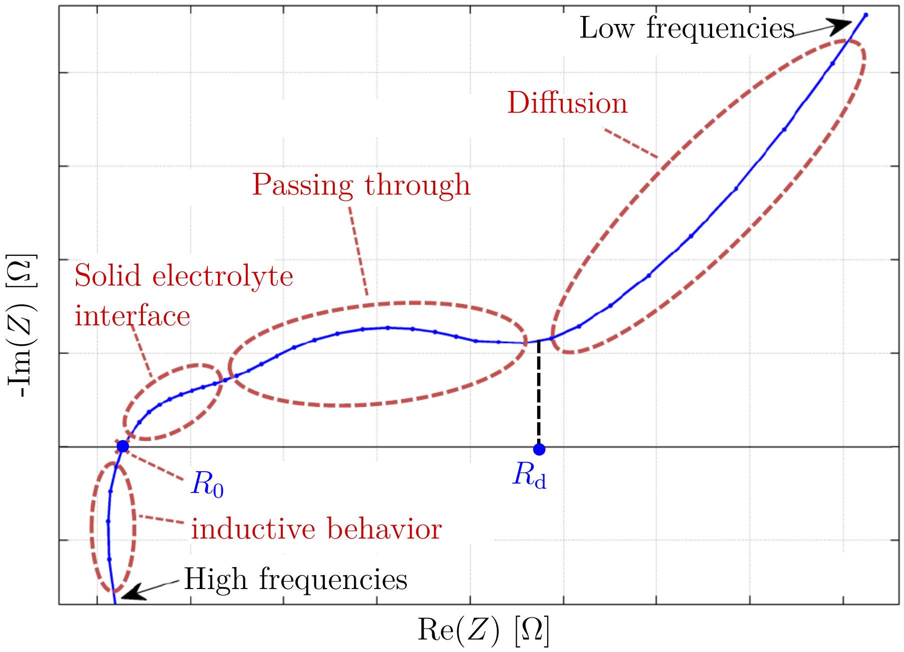

Figure 5.1: Qualitatively typical EIS response represented as a Nyquist Plot [97]

Typically, the battery impedance spectrum shows:

- at low frequencies: a diffusion tail (Warburg element) [99] with a constant phase,
- at middle frequencies: two semicircles representing the physical process of charge-transfer (passing-through) and the physical processes at the Solid Electrolyte Interface (SEI),
- a purely resistive intersection point with the X-axis (Point R_0), and
- at higher frequencies: a (mainly but not purely) inductive tail [100].

The second semicirle at middle frequencies (corresponding to the SEI) is generally smaller than the first one (corresponding to charge transfer). It is established that its presence corresponds to the presence of a SEI or to the particle-to-particle-contact and that its size increases with age. It can be indistinguishable and/or neglected for new cells [101].

The extracted spectra can be used to generate a battery model (See Subsection 2.6). Typical circuits commonly used in the literature to model this frequency response are shown in Figure 5.2a [102] (using the Warburg impedance element) and in Figure 5.2b [58, 103] (using conventional passive circuit elements).

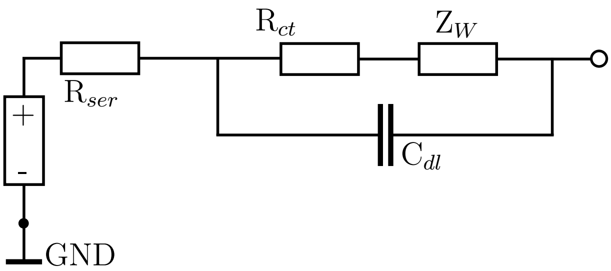

(a) Battery model with Warburg element [102]

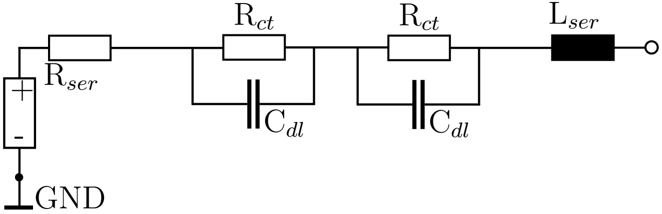

(b) Battery model with passive elements [58, 103]

Figure 5.2: Battery impedance models

In Figure 5.2:

R_{ser} is a serial purely ohmic resistance,
R_{ct} is the charge-transfer resistance,
C_{dl} is the double-layer capacitance,
L_{ser} is the serial inductance, and
Z_{W} is the Warburg element.

In fact, the Kramers-Kronig-transformation [43], which suggest that different circuits can have diverse topologies and still show identical or similar impedance response, can be applied on batteries. Therefore, a battery can be modeled with a more or less simple circuit topology which elements having little or no direct physical interpretation, but are easier to parameterize than in a complex circuit having the same frequency response.

5.1.2 Definitions of the battery internal resistance

There is an ambiguity around the concept of the internal resistance of a battery in the literature [100, 101]. As explained in the previous section, the battery shows a complex impedance and not a purely resistive behavior. The following definitions are found in the literature for the battery internal resistance:

- The Direct Current Resistance (DCR) is the ohmic contribution observed at the battery poles at the event of the establishment of a non-zero current [100, 101]. The value is referred to as R_{DCR} (also R_{Ω}). It is widely accepted that the resistances of the separator, active mass, the current collectors and the connections between them, as well as the resistance related to th ionic conductivity of the electrolyte and the electronic conductivity of the current collectors sum up to R_{DCR} [100, 103]. The aging processes affecting the electrolyte and electrodes (see Section 2.5) contribute to the increase in this value.

- The point where $-\Im(Z)$ shows a first local minimum observed between the low-frequency and the middle frequency spectra shows a near-to-ohmic impedance value. The real part of this impedance is referred to by R_{d} (See Figure 5.1). This definition can substitute the definition of R_{DCR}. The points are physically different, but the values are close and show a similar behavioral dependency on temperature and other factors [101].
- The point of intersection of the impedance spectrum with the Real part axis ($-\Im(Z) = 0$) is referred to as R_0, also as the zero-phase impedance value. The exact frequency (f_0), where the capacitive and the inductive parts are compensated, and this purely resistive value is delivered, is previously unknown. Therefore, the value of R_0 is only extractable when the EIS has covered the frequency range around f_0 (typically but not necessarily between 100 Hz and 1 kHz) [101].
- Another, close, definition of the internal resistance, noted $R_{\mathrm{real,min}}$ is the estimated minimum value of the real part of the cell impedance. It corresponds to the (almost) constant real part of the impedance values in the inductive tail at high frequencies [34, 70] (See Figure 5.1).

5.1.3 Measurement of the battery internal resistance

Various ways to calculate internal resistance correspond to the different definitions. Several methods are presented here (and in more details in [100, 101, 104]).

5.1.3.1 Exhaustive or simplified EIS

The Electroimpedance Spectroscopy (EIS) is a system identification tool that delivers the system (complex) impedance spectrum (dependency on the frequency) as a response to a multi-spectral excitation [105]. When applied to a battery cell, it depicts the cell dynamics and assesses its internal electrochemical processes. A Linear time-invariant (LTI) system is a necessary requirement for the application of EIS measurements [106]. Since the battery cell is highly nonlinear during the charging and discharging cycles, the EIS can only be applied at given SoC values, where the battery has had a compulsory rest of a given period, so that the linearity of the system is sufficiently guaranteed.
The EIS relies on the multi-spectral excitation of the system using sinusoidal signal (Voltage/ Current) and the measurement of its response (Current/ Voltage, respectively) at

those specific frequencies, therefore measuring the impedance.
The EIS allows to measure the impedance as the frequency response at individual frequencies using several sinusoidal signals. The impedance is calculated according to Equation 5.1.

$$\overline{Z} = \frac{\overline{U}}{\overline{I}} = \frac{\hat{U} \cdot e^{i(\omega t + \varphi_u)}}{\hat{I} \cdot e^{i(\omega t + \varphi_i)}} \tag{5.1}$$

An exhaustive EIS should have

- a large spectral coverage: range of covered frequencies. Ideally, for a LiB cell, The interesting frequency range would be from DC (several µHz) up to around 10 kHz, and
- a high spectral density: number of covered frequency points per decade [106].

Due to the low impedance values of the LiB as DUT (expected values of the impedance in the range of mΩ), the measurement equipment should be adequately precise. Most measurements take in laboratory environments with apparatuses especially designed for this task [34, 107], suppressing wires and parasitics contributions to the impedance.
The task becomes even more challenging if an integrated measurement device is required (on-chip). In fact, the design of the signal generator (of sinusoidal signals) puts high constraints of area and power consumption on the chip in order to realize the needed spectral coverage and density [106]. In addition, the high power signals (impedance in the mΩ range, currents in the A range) to be measured require special devices and/or design technologies.
A simplified EIS reduces the spectral density to several points and therefore the effort to measure them. The rest of the impedance graph is completed using a fitting tool or a battery model. However this result risks becoming erroneous with changes in the battery state [100].

5.1.3.2 Measurement at a single point/ AC resistance

The measurement at a single point is an oversimplification of the EIS and its reduction to a single frequency point. Most battery manufacturers use solely an AC signal at 1 kHz [100, 103]. The real part of the measured impedance, referred to as the LiB cell internal resistance [70, 103] is the resistance value presented in the commercial data sheet. The measurement frequency of 1 kHz is typically close but not necessarily equal to the transition frequency f_0, where the capacitive and inductive parts of the impedance cancel out delivering the purely resistive R_0. This extracted value at 1 kHz is widely accepted as a substitution for R_0 or $R_{\text{real,min}}$.

5.1.3.3 Joule's heating

Joule's first law helps estimate the value of internal resistance of the batteries R_{int} by estimating the losses due to the presence of a resistance and therefore as heat, according to Equation 5.2, wherein E_{losses} is the lost heat energy $P(t)$, $I(t)$ and $R_{\text{int}}(t)$ are the lost heat power, the current through the battery and the internal resistance of the battery as a function of time, respectively.

$$E_{\text{losses}} \;=\; \int P(t)\ \mathrm{d}t \;=\; \int I(t)^2 \cdot R_{\text{int}}(t)\ \mathrm{d}t \tag{5.2}$$

In order to extract the R_{int}, the resistance has to be constant over time. Since the value of the internal resistance is not constant as it depends on the SoC, age and other factors, its mean value $R_{\text{int,mean}}$ is then extracted according to Equation 5.3, wherein the losses are measured between the time points t_1 and t_2, and I is the current during the measurement time period assumed constant.

$$R_{\text{int,mean}} \;=\; \frac{E_{\text{losses}}}{I^2 \ \cdot\ \Delta T} \;=\; \frac{E_{\text{losses}}}{I^2 \ \cdot\ (t_2 - t_1)} \tag{5.3}$$

The energy losses are estimated from the difference of the charging and discharging energies, or by the means of a calorimeter [103].

5.1.3.4 Current step/ Current interrupt

This method aims to measure R_{DCR} by means of Ohm's law. An ohmic contribution is observed at the battery cell poles at the event of a current step (particularly the connection of load or the interruption of current). The internal resistance is then calculated differentially according to Equation 5.4.

$$R = |\frac{\Delta U}{\Delta I}| = |\frac{U_2 - U_1}{I_2 - I_1}| \tag{5.4}$$

One particular voltage is the Open Circuit Voltage (OCV) where, $U_1 = V_{OCV}$ and $I_1 = 0$. Figure 5.3 shows the contribution of the internal battery resistance to the voltage drop at the event of a current pulse. Since the battery impedance is not purely ohmic [108], an initial immediate drop (ΔV_0 in Figure 5.3) is seen at the event of non-zero current, followed (in time) by a dynamic further potential-decay (ΔV_1).

However, it is practically very difficult to separate these two contributions to the voltage drop because it would require an infinitely short current pulse together with an infinitely fast measurement [101]. At least, the pulse must be kept short enough for the measurement to be accurate. In fact, high currents are required to reach the detection limit of

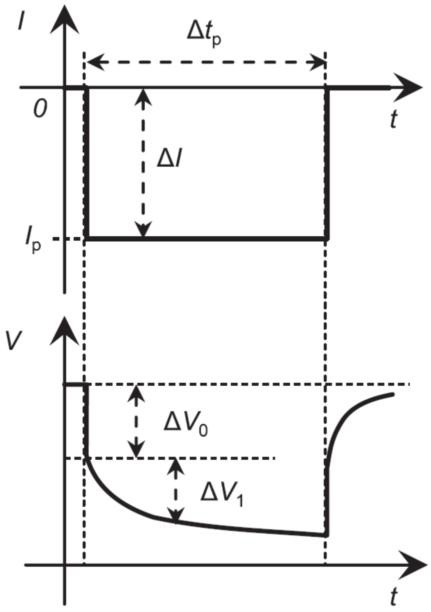

Figure 5.3: The R_{int} contribution to the voltage drop [101]

standard measurements test benches: for detectable voltages in the mV range and DUT resistances in the mΩ range, currents in the A range are needed and expected. With such high power levels, longer pulses would contribute to the heating of the measurement loads leading to measurement inaccuracies due to the Temperature Coefficient (TC).

5.2 Pulsing method and measurement circuit

The aim of this experiment is to investigate the possibility of designing an sensor for the internal resistance of a LiB with solely OTS elements on a PCB using the pulsing method as presented in Subsection 5.1.3.4. The definition used for the internal battery resistance (in the following referred to as R_{int}) is therefore the DCR presented in Subsection 5.1.2.

5.2.1 The pulsing method

Several standardization organizations such as the ISO, the VDA and the IEC [109, 110] set standards for general test procedures for Lithium-ion battery cells in automotive applications. Each test assesses one or several characteristics. Tests can be conducted at cell, module or system level and include performance, aging and safety characteristics [111, 112].

Among these test procedures, current step methods to measure the internal resistance of LiB cells are available [103]. Battery cell manufacturers are recommended to enlist the measurement standardized test and its results in their data sheets to guarantee a fair comparison of different LiB cells from different manufacturers.

The tests set the duration(s) and the current rate of charging and/or discharging pulses, in addition to the rest periods between the different measurement pulses. The VDA testing procedure suggests a discharging pulse with a duration of 18 s, a current rate of 20 C [1] and a rest period of 40 s, followed by a charging pulse of 10 s with a current rate of 16.6 C. The Hybrid pulse power characterization (HPPC) pulse test, a test norm suggested and set by the IEC, originally intends to test the dynamic power capability [63, 104].
Since the exact discharge C for a cell cannot be exactly set in a similar way to a battery laboratory, these tests were used in this work as a guideline. They were slightly modified to set the measurement method used to determine the internal resistance R_{int}. Particularly, the test sequence timing of the HPPC (Figures 5.4 and 5.5 [113]) is adopted. The 1 h rest guarantees a near LTI system.

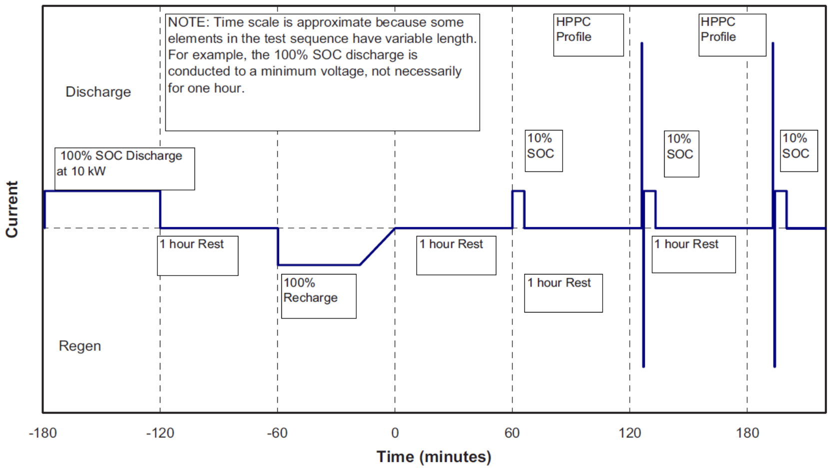

Figure 5.4: The HPPC sequence start [113]

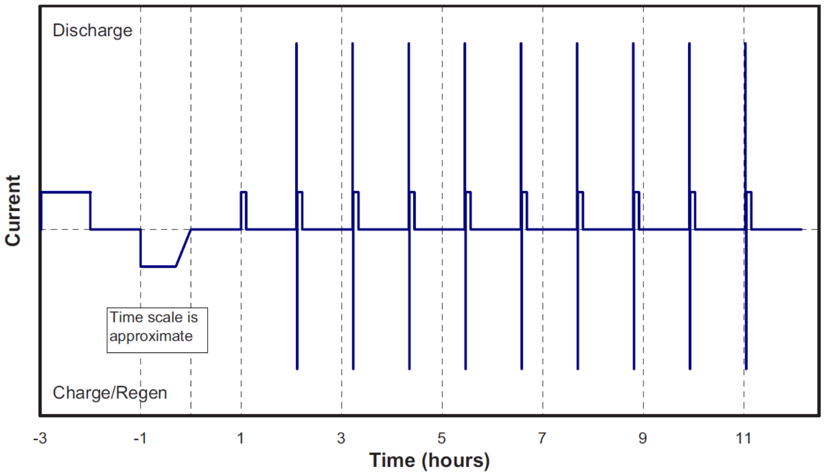

Figure 5.5: The complete HPPC sequence [113]

---

[1] Definition of C-ratio in the Terminology section

The charging pulse measurement method, as will be presented in the next section, does not rely on setting a fixed discharge rate. It rather uses precision resistors (with well-known values) as discharging loads and measures the discharge currents through them. Three different discharging resistor values in combination with three different battery chemistries were used to assess the dependence of the resistance value on these factors.

5.2.2 Measurement principle

In its simplest form, the pulsing circuit can be designed as in Figure 5.6. The battery cell is represented by an ideal battery element in series with its internal resistance R_{ser}. R_{ser} is the unknown in this configuration, considered to be non-linear [108] and dependent on several factors (temperature, aging, etc.), but primarily on the SoC, and correspondingly on the Depth of Discharge (DoD). The current pulse is created when the switch is closed and the battery cell is connected to the load resistance R_{L}. The value of the current is set by the values of the currently available voltage at the battery cell, its serial resistance, and the load resistance, in the case of an ideal switch.

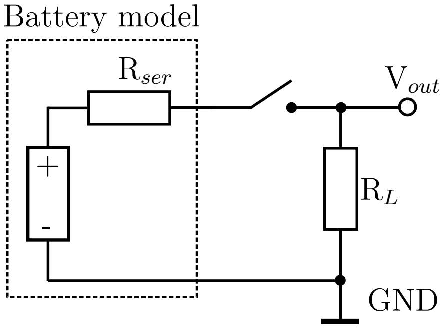

Figure 5.6: Measurement principle of the internal resistance

5.2.3 Sensitivity to the serial resistance and choice of the load resistance

The dependence of the output voltage V_{out} on load and serial resistances, if the switch is considered ideal, is given by Equation 5.5.

$$V_{\mathrm{out}} = \frac{R_{\mathrm{L}}}{R_{\mathrm{L}} + R_{\mathrm{ser}}} \cdot V_{\mathrm{DC}} \tag{5.5}$$

The sensitivity S of the output voltage V_{out} to the serial resistance R_{ser} is given by the partial derivative as in Equation 5.6.

$$S(R_L, R_{ser}) = \frac{\partial V_{\mathrm{out}}}{\partial R_{\mathrm{ser}}} = R_{\mathrm{L}} \cdot V_{\mathrm{DC}} \cdot \frac{-1}{(R_{\mathrm{L}} + R_{\mathrm{ser}})^2} \tag{5.6}$$

In order to find the extrema of S using R_{L}, S is differentiated with respect to R_{L} (Equation 5.9). The point where this derivative equals zero and changes its sign is the extracted (Table. 5.1).

$$
\begin{aligned}
M &= \frac{\partial S}{\partial R_{\mathrm{L}}} && (5.7)\\
&= (-V_{\mathrm{DC}}) \ \cdot \ \frac{(R_{\mathrm{L}} + R_{\mathrm{ser}})^2 - R_{\mathrm{L}} \cdot 2 \cdot (R_{\mathrm{L}} + R_{\mathrm{ser}})}{(R_L + R_{ser})^4} && (5.8)\\
&= V_{\mathrm{DC}} \ \cdot \ \frac{R_{\mathrm{L}} - R_{\mathrm{ser}}}{(R_{\mathrm{L}} + R_{\mathrm{ser}})^3} && (5.9)
\end{aligned}
$$

As explained in Table 5.1, in order to maximize the sensitivity of the output voltage V_{out} to the internal resistance R_{ser} of the battery, the load resistance R_{L} used as a current measurement resistor needs to be equal to or in the same range as R_{ser}, i.e. in the mΩ range. However, this will lead to currents in the kA range. In the following, a compromise is found by choosing load resistances in the Ω range, in order to have manageable currents in laboratory environment, trading off hereby the sensitivity of the measured output quantity (V_{out}) and therefore the accuracy of the end result (R_{ser}).

Table 5.1: Slope of the sensitivity curve depending on R_{L}

Value of R_{L}	$R_{\mathrm{L}} < R_{\mathrm{ser}}$	$R_{\mathrm{L}} = R_{\mathrm{ser}}$	$R_{\mathrm{L}} > R_{\mathrm{ser}}$
Sign of M	negative (-)	$M = 0$	positive (+)
Slope of S	$\searrow$	$\longrightarrow$	$\nearrow$

5.2.4 Circuit design

The more detailed version of the regulated pulsing circuit of Figure 5.6 is shown in Figure 5.7.

The holder for the DUT (the LiB cell) is chosen with Gold (Au) contacts [114].

Power resistors with the 3 different values of $10\,\Omega$, $2.5\,\Omega$ and $1\,\Omega$ [115] were chosen as precision current measurement load resistors R_{L}.

A GaN-transistor is chosen as switch because of its low on-resistance (in the mΩ range) and its high current capabilities ($> 40\,\mathrm{A}$) [116]. Both the power resistors and the GaN transistors are supported with heat sinks suitable to their housing to assist with the power dissipation and avoid the TC effect.

As shown in Figure 5.7, the voltages at the pole of the DUT, at the resistor and at the Drain of the GaN-switch are measured using a high precision DMM. These voltages are not loaded by this measurement but extracted after a buffered stage using an Op-Amp in a voltage follower configuration. The Op-Amp is chosen with a very low offset (in the

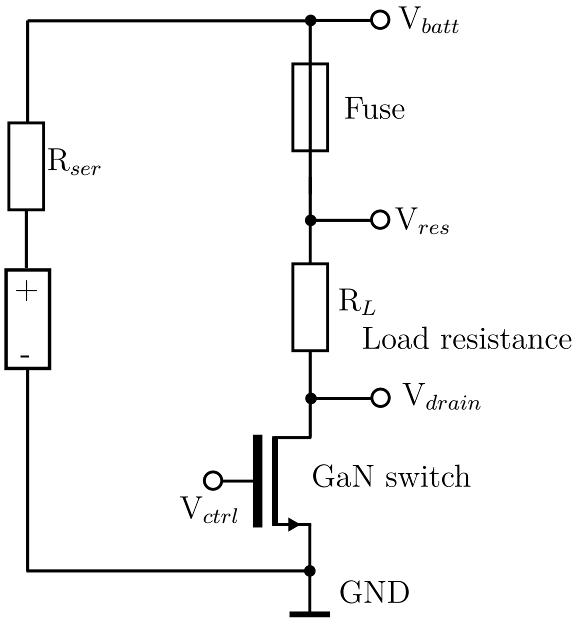

Figure 5.7: The measurement circuit design

µV range). It is supplied with the stabilized output of a voltage regulator (not shown). Figure 5.8 shows the layout of the designed circuit. Empty (of footprints and others) areas of the PCB are filled with as much coverage of the GND plane as possible to increase the system's heat dissipation properties. The tracks width was increased to enhance the current carrying capability of the board [117]. Figure 5.9 is a photo of the circuit showing the battery holder and the power elements (GaN transistor and power resistor).

5.3 Measurement method and results

5.3.1 Used battery cells

The chosen LiB cells for this test are cylindric cells of type *18650*. They have similar geometrical dimensions and electric capacities but different types (internal chemistries) as listed in Table 5.2 (adapted from data sheets and technical descriptions) [2]. A flat positive pole in a 18650 cylindric battery cell indicates the absence of a protection circuit. The dimensions in Table 5.2 are given as Diameter×Height.

5.3.2 Testing conditions and measurement sequence

As listed in Table. 5.2, the recommended charging method: CC-CV (Constant Current-Constant Voltage [118, 119]) is used. To follow the HPPC measurement sequence as

---

[2] See Chapter 2, Table 2.1 for battery chemistries

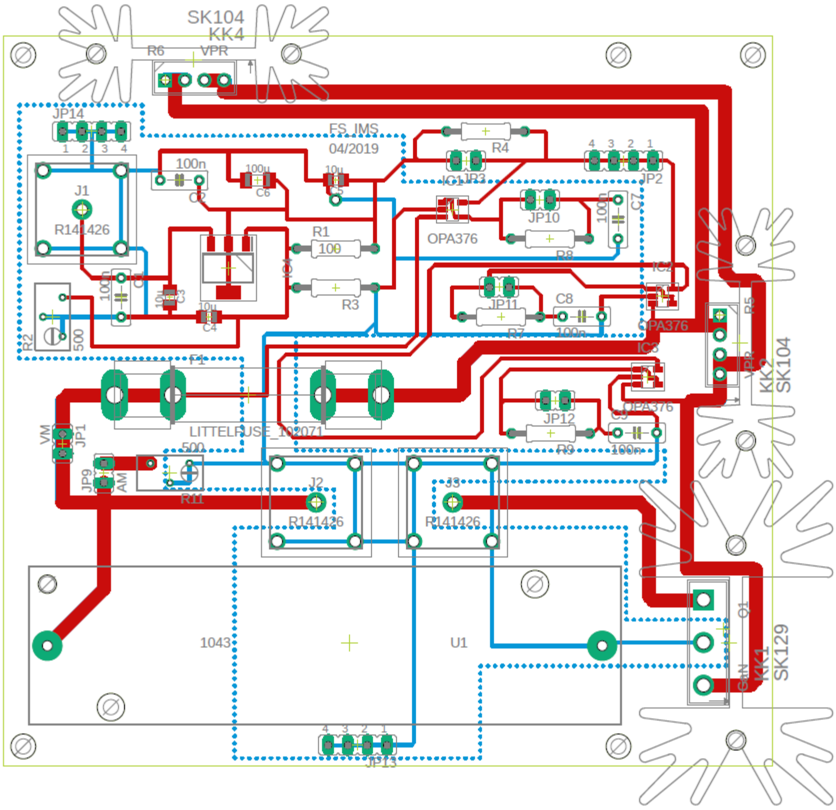

Figure 5.8: The measurement circuit PCB layout

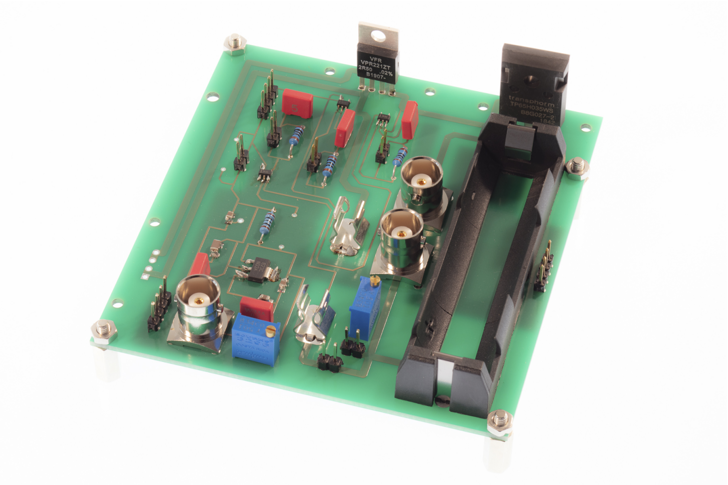

Figure 5.9: The designed measurement circuit on PCB

Table 5.2: Comparison of the characteristics of the tested battery cells

Cell	A (blue)	B (green)	C (purple)
Type	INR	NCR	IMR
Rated capacity	3200 mA h	3100 mA h	3000 mA h
Nominal voltage	3,6 - 3.7 V	3.6 V	3,6 - 3.7 V
Max. current output	$3\,\mathrm{C} \approx 10\,\mathrm{A}$	$2\,\mathrm{C} = 6.2\,\mathrm{A}$	20 A
Dimensions	18.3 mm×65.1 mm	18.1 mm×64.9 mm	18.5 mm×65.2 mm
Internal resistance	0.07 Ω	Not specified	0.04 Ω
Plus pole	flat		
Charging process	CC-CV		
Charging end voltage	4.2 V		
Cut-off voltage	2.5 V		

shown in Figure 5.5, the Lithium-ion cell is fully discharged (until its manufacturer-specified discharge cut-off voltage [63]) and then fully charged to SoC = 100% before the measurement sequence. The cell is then placed in its holder on the measurement PCB. The load resistance on the PCB has the value of 10 Ω, 2.5 Ω or 1 Ω.

The pulsing sequence is controlled using the GaN switch. After the measurement of the OCV, a pulse is generated for 10 s, leading to a fall in the battery voltage allowing the measurement of the internal resistance. After a rest of 10 s (GaN switch is off), the discharge continues to reach the next 10% DoD increment (i.e. from SoC = 100% to 90%, from SoC = 90% to 80% and so on down to SoC = 10%). The length of the discharge pulse to reach the next 10% DoD is calculated from the battery capacity and the average current value during the 10 s pulse. It lasts several minutes or more. It is to be noted that the first discharge pulse of 10 s already slightly discharged the cell and should be taken into account in this calculation. Table 5.3 shows the measurement sequence described. The measurement is controlled with a NI-LabVIEW program. The complete measurement sequence is repeated for the three battery cells and their different chemistries in combination with the three different load resistance values. The steps 1 to 4 as well as 15 and 16 ensure having similar initial conditions for all cells.

5.3.3 Measurement results

Figure 5.10 shows an example of the current pulse of 10 s for the battery cell B at SoC = 100% using a load resistor R_{load}, followed a rest period 10 s and the continued discharging until the next DoD increment.

Figures 5.11, 5.12 and 5.13 show the extracted measurements of the internal resistances R_{int} using the three load resistance values for cells A, B and C, respectively. The x-axis shows the SoC values from 10% to 100%. The y-axis shows the extracted internal

Table 5.3: Measurement sequence to determine R_{int}

Step	**Sequence**	**Notes**
1	complete discharge	until cut-off voltage
2	1 h rest	-
3	full charge	
4	1 h rest	-
Measuring algorithm at SoC=100% (DoD=0%)		
5	GaN-switch is off	for 1 s, measurement of OCV
6	GaN-switch is on	Current pulse of 10 s, measurement of potential decay
7	GaN-switch is off	for 10 s
8	GaN-switch is on	Continue discharge to the next 10% DoD increment SoC=90% (DoD=10%)
9	1 h rest	-
Iteration at following DoD values		
10	GaN-switch is off	for 1 s, measurement of OCV
11	GaN-switch is on	Current pulse of 10 s, measurement of potential decay
12	GaN-switch is off	for 10 s
13	GaN-switch is on	Continue discharge to the next 10% DoD increment last discharge level is SoC=10%
14	1 h rest	-
15	complete discharge	until cut-off voltage (if necessary)
16	Stop measurement	-

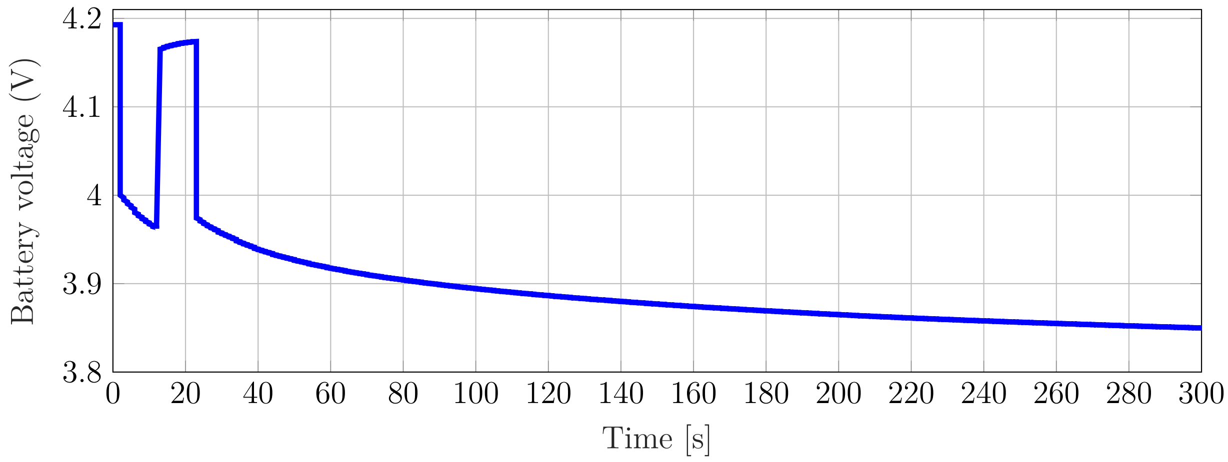

Figure 5.10: The used current pulse for the measurement of R_{int}: Pulse for 10 s, Rest for 10 s, then discharge until the next DoD increment

resistance values in the mΩ range.

5.3.4 Results discussion

The following comments and conclusions can be made from this experiment:

- A PCB with OTS elements was successfully designed and fabricated for the purposes of implementing an internal resistance sensor for LiB cells. The chosen pulse method enables the extraction of internal resistance values for different cell types and SoC values.
- The extracted internal resistance is in the expected range of 50 to 200 mΩ, although slightly higher for cell A.
- The extracted internal resistance values are not equal to the values specified for the cells, although these were specified without further information concerning the method and/or conditions of measurement. No temperature dependence or load profile characteristics were specified either.
- The 3 different values used for the load resistance R_L do not show a direct discrepancy. No trend was seen as to which value offers higher measurement accuracies. This might be due to the fact they are in the same range (1 to 2-digit Ω range), which is considerably higher than the optimal value of R_L.
- The measurement accuracy with the given PCB design and device choices and under the given laboratory conditions (no additional electrical shielding) is not sufficient to see a trend differentiating the values extracted using the different resistors R_L, nor to distinguish a difference between the battery chemistries.
- The current design is theoretically suitable to extract the internal resistance value of a LiB cell but practically still not in the needed accuracy range. The integration of this solution on-chip is therefore not immediately possible without further improvements. Additionally, integrating the proposed PCB would require a dedicated GaN technology or alternatively a power CMOS technology to handle the high currents.

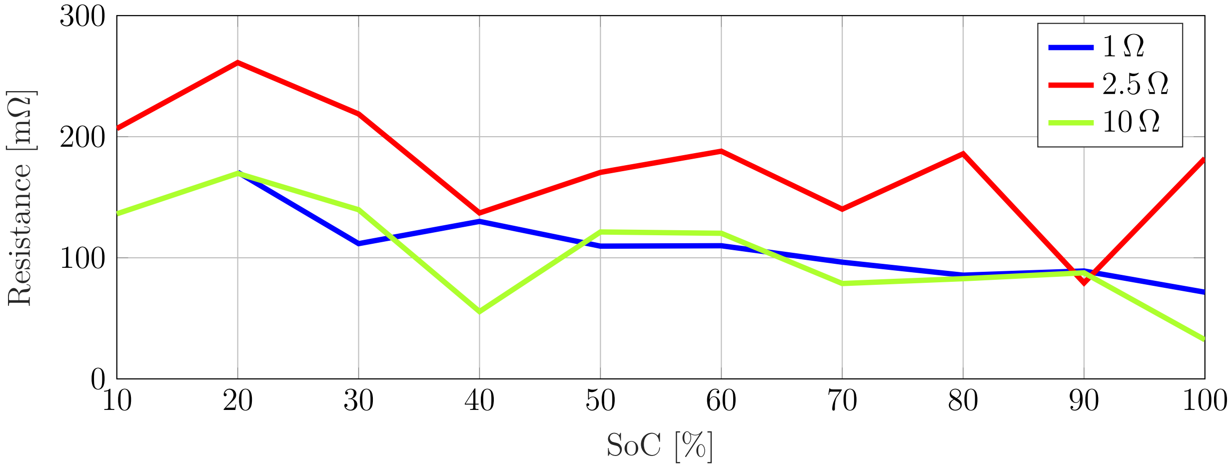

Figure 5.11: Extracted measurements of R_{int} for cell A

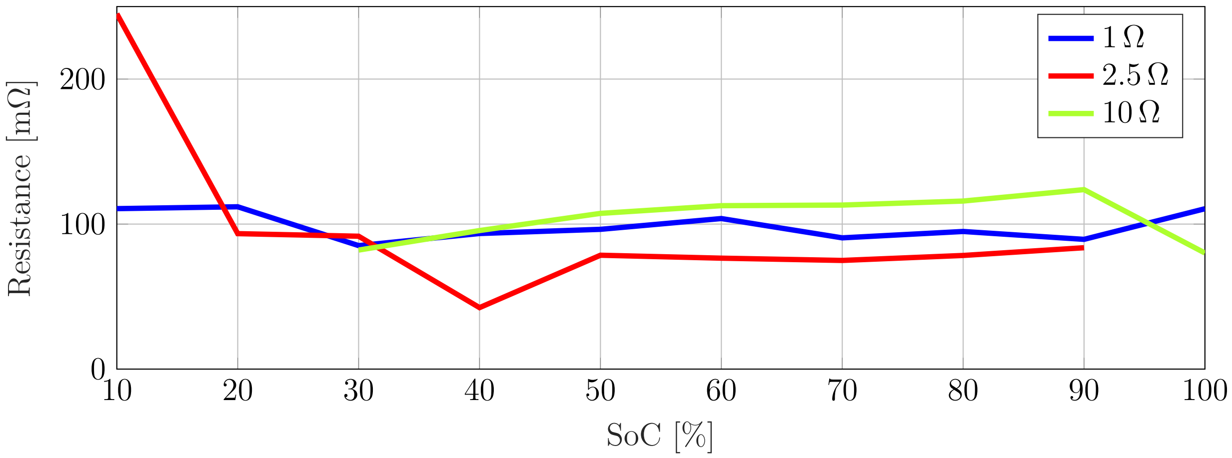

Figure 5.12: Extracted measurements of R_{int} for cell B

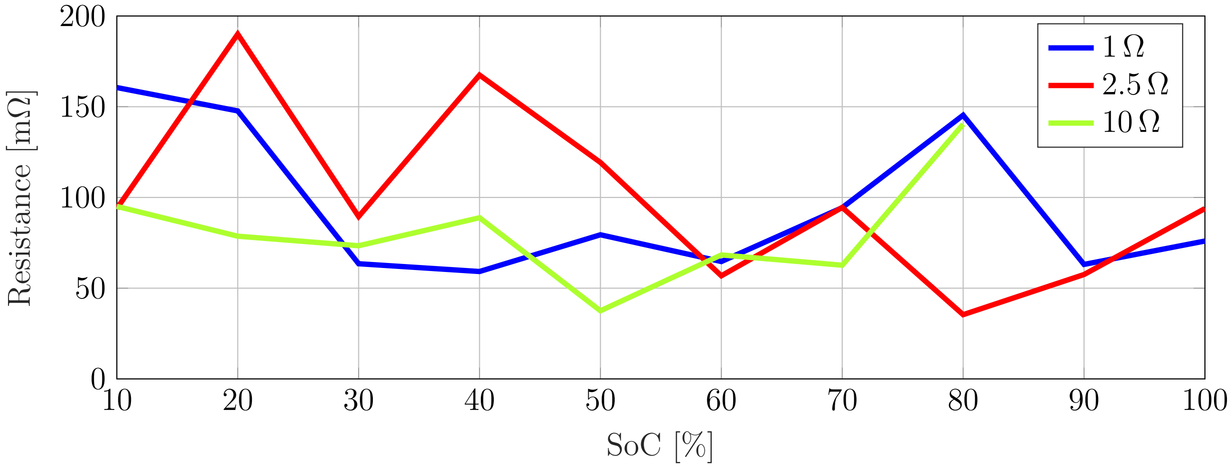

Figure 5.13: Extracted measurements of R_{int} for cell C

Chapter 6

Chemical compatibility inspection of a chip packaging foil system with a Lithium-ion battery electrolyte

The Smart-Lithium-ion battery (Smart-LiB) concept was presented in Chapter 3. A Cell Supervisory Circuit (CSC) was designed as PCB and fulfills the function of real-time monitoring of LiB cells.

It was concluded that a more efficient version of CSC should be as a monolithic design (electronic chip). Since the CSC is completely integrated inside the LiB cell, the packaging of the future chip should protect it from the harsh chemical environment which is the battery electrolyte. This is particularly relevant in the case of liquid electrolytes (Subsection 2.1.1.2). The inspection of the chemical compatibility of the chip packaging foil system with a lithium-ion battery electrolyte is therefore necessary [1].

The Chip Film Patch (CFP) technology [61] enables the embedding of thinned chips (down to 20 µm) in a predefined sequence of Benzocyclobutene and Polyimide layers. The technology is compatible with the standard CMOS process lines. After the the chip embedding and the realization of the metal interconnections, the obtained result is a thin carrier and packaging system.

This chapter reports on the chemical compatibility of this circuit packaging system as well as of the metal connections with the battery electrolyte. Test foils according to the CFP technology were designed, fabricated and introduced into the electrolyte for different test periods. Metal structures are produced on the test foils. These metal structures constitute an example of the metal interconnections to the embedded chip as well as the basis for resistive-based sensors. Conclusions regarding two process versions are met by

---

[1] This was conducted in cooperation with the research group “electrical energy systems” at the Institute for Photovoltaics (IPV) and was published in [120].

optically and electrically comparing the before and after status of the test foils.

6.1 The Chip Film Patch technology

Polymers are a widely used option for the packaging of electronic chips. The chip and accordingly its surface is passivated, laminated and protected. Since flexible electronics (flexible electronic components and systems) are gaining an increasingly important interest as an alternative to conventional silicon (Si) technology [121], the polymers used are accordingly required to answer to more complex, sometimes contradictory or hard to be combined requirements, e.g. robustness and bendability. The combination of two (or more) compatible polymers, which have complementary properties is a possible workaround. One of the polymers servers as an embedding and the other as an reinforcement polymer. Polymers which are fully compatible with the CMOS process lines are favorable [60].

The CFP technology uses stacks of Benzocyclobutene (BCB) and Polyimide (PI) as carrier and encapsulation system for thin electronic chips. When a chip is embedded, the BCB constitutes the embedding polymer. The embedding polymer fulfills several requirements: low dielectric constant, low losses, low moisture uptake and compatibility with the metal used for the interconnections. However, BCB features a low ductility. A system consisting exclusively of BCB layers is therefore fragile and easily prone to crack. The PI is therefore used as reinforcement to offer the system more flexibility and consequently more robustness and long-time consistent functionality [60].

The CFP production process consists of embedding and interconnection steps using metal lines. It is carried out using a fully CMOS- compatible process line on a wafer as carrier, from which it is then released. The final thickness of the complete foil system is adjustable and hence variable. It can range from 20 to 100 µm. For the purpose of inspecting the chemical compatibility between the CFP packaging system and the battery electrolyte, no active electronic chip was used, but only the foil system and the metal interconnections. In the following subsections, two process versions fabricated and tested in this work are presented: the low-Coefficient of Thermal Expansion process and the Two-polymer process.

6.1.1 The low-Coefficient of Thermal Expansion process

The low-Coefficient of Thermal Expansion (low-CTE) process is detailed in Figure 6.1 (not in scale) and is carried out following the next steps.

(a) Preparation of a handle wafer

A standard Si-Wafer with a diameter of 150 mm an a thickness 675 µm is used as carrier and therefore prepared for the process. the coating of an adhesion promoter (TI Prime) as shown in Figure 6.1a.

(b) PI coating
A total of 15 µm of the Polyimide PI2611 are coated as shown in Figure 6.1b. The PI thickness per coating step is 5 µm.

(c) BCB coating
A total of 3.5 µm of BCB is coated (Figure 6.1c).

(d) Metal sputtering
A 1 µm layer of the AlSiCu-Alloy is sputtered (Figure 6.1d).

(e) Lithography for AlSiCu structuring
The photoresist is applied and the metal is structured using a laser writer, delivering the designed metal structures (Figure 6.1e).

(f) AlSiCu structuring (dry etching), Figure 6.1f

(g) PI and BCB coating
Again, a 15 µm layer of the PI PI2611 and a 3.5 µm of BCB are coated (Figure 6.1g).

(h) Lithography for pad opening (Figure 6.1h).

(i) Etching of BCB and PI for pad opening
The pads are opened after lithography, where the polymers (BCB and PI) are etched. The opening of the pads allows the contacting and the measurements of the metal structures (Figure 6.1i).

6.1.2 The 2-polymer process

The 2-polymer process is conducted in a similar way to the low-CTE process. The following list presents the steps and the differences.

(a) Preparation of a handle wafer
A standard Si-wafer with a diameter of 150 mm and a thickness of 675 µm is used as carrier. 1 µm silicon oxide is formed on the wafer by wet thermal oxidation.

(b) Adhesion promoter (HMDS) and BCB coating (3.5 µm)

(c) Durimide coating (10 µm, Thickness per coating step 5 µm)

(d) BCB coating (3.5 µm)

(e) Metal evaporation: 1 µm Aluminium (Al)

(f) Lithography for Al structuring

(g) Al structuring (by dry etching)

(h) 1 µm Al evaporation

(i) Lithography for pad opening

(j) Etching of BCB and PI for pad opening

The metal Al and the alloy AlSiCu are good candidates for tests with the battery electrolyte since the containers of LiB electrolyte solutions as well as the housing of LiB cells is generally out of Al. Hence, a good compatibility between the metal type and the electrolyte is guaranteed.

(a) Preparation of the handle wafer

(b) PI coating

(c) BCB coating

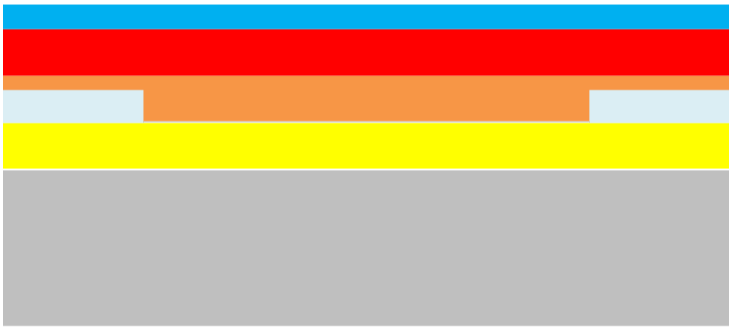

(d) Sputtering of AlSiCu

(e) Lithography for AlSiCu structuring

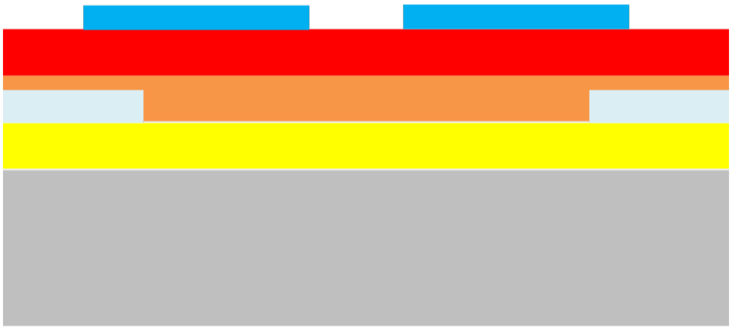

(f) AlSiCu structuring (dry etching)

(g) PI and BCB coating

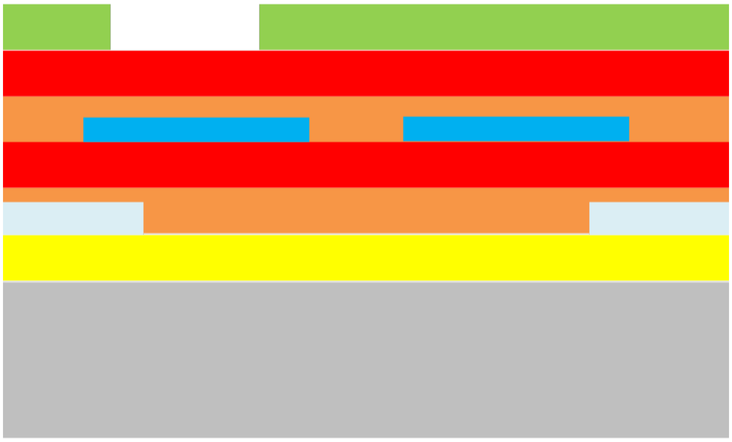

(h) Lithography for pad opening

(i) Etching of BCB and PI for pad opening

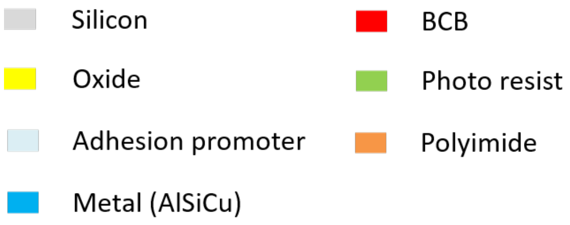

(j) Legend

Figure 6.1: Steps of the low-CTE process

6.2 Foil design

The test foils were designed and fabricated according to the low-CTE as well as the 2-polymer process. Figure 6.2 shows the design of a test foil. Each foil has the dimensions 25 mm × 40 mm.

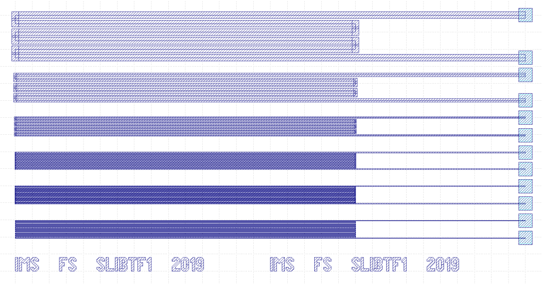

Figure 6.2: Design of a test foil

Therefore, a total of 16 test foils of CFP technology can be produced on a single standard wafer (Diameter of 150 mm) as shown in Figure 6.3.
Each foil contains 6 metal structures with the different widths. The interconnect metal width is scaled between 200 µm and 10 µm. Each metal structure is provided with metal pads to allow its contacting and measurement.
After their production, the foils are cut and released from the wafer using a scalpel or a

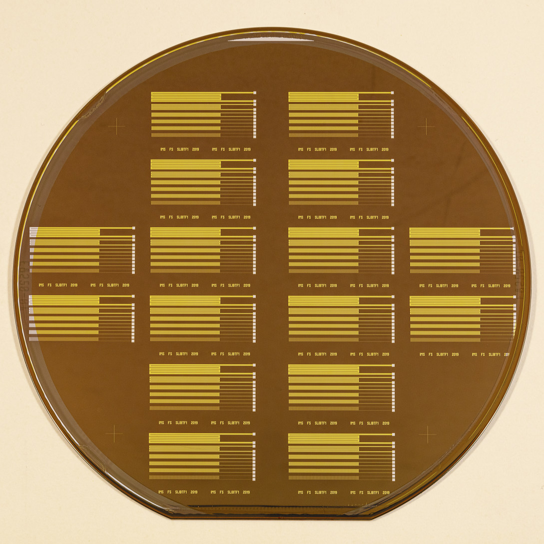

Figure 6.3: 16 test foils on a CFP wafer

laser cutter. This operation is delicate and the foils, especially the ones on the edge of the wafer, are easily damageable. A perfect yield of 100% of useable test foils is rare. In this experiment, one wafer of each process version was fabricated. The yield of usable test foils after their release was 14/16 (87.5%) is both cases. Figure 6.4 shows a zoomed view of a produced test foil.

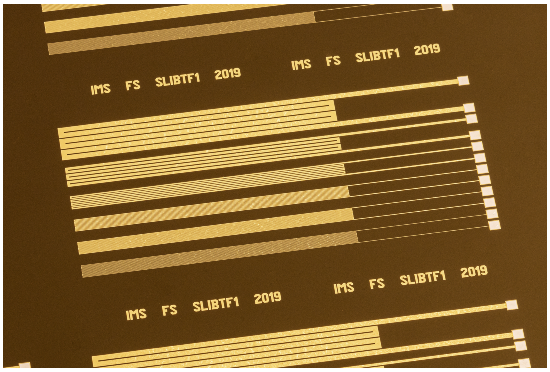

Figure 6.4: A zoomed view of a produced test foil

6.3 Pre-measurements

With the help of a manual prober and metal measurement needles, the metal structures of each foil are contacted at their pads and their electric resistance is measured. 4-wire measurements are conducted for all foils. Table 6.1 shows the averaged values of metal lines resistances depending on their width.

Table 6.1: Averaged resistance values of metal lines for both process versions

Metal line width (in µm)	Averaged resistance value (in Ω)	
	low-CTE process	2-polymer process
200	10,6	12,3
100	21,1	28,7
50	54,8	63,9
25	186,9	217,7
20	299,4	347,5
10	639	731,2

6.4 Test conditions

The testing of the compatibility of CFP system with the battery electrolyte is conducted using Al containers where the test foils are introduced and enclosed after being immersed with the electrolyte solution. The small containers are then stored in a Glove Box (Typ: LABstar MBraun [122]). The atmosphere inside the Glove Box consists of Argon with water and O_2 concentration <0,5 ppm.

Before coming into contact with the electrolyte, it has to be ensured that no traces of water still reside on the foils. Therefore, they are intrduced into a vacuum oven for 12 h at T = 80 °C. The test foils undergo the test for different time periodes: 1, 2, 3 and 6 weeks. A real-time measurement is unfortunately not possible. The test foils are then (at the end of the corresponding test period) extracted and measured. The before and after status is then compared. After the test and upon the extraction, the foils are washed in a Dimethyl Carbonate bath inside the Glove Box, to ensure that any residual Lithium salt is solved.

The used electrolyte is a Lithium hexafluorophosphate solution in Ethylene Carbonate (EC) and Dimethyl Carbonate (DMC), with 1.0 mol of $LiPF_6$ in EC/DMC [123].

6.5 Results

6.5.1 Optical examination

The optical inspection of the electrolyte in the aluminium containers after the test shows no signs of discoloration even after the longest test period (6 weeks). A yellowish discoloration of the otherwise transparent electrolyte solution is namely a sign of the presence of Hydrofluoric acid (HF) as a reaction result between H_2O (in case present) and $LiPF_6$. It can be concluded that the drying-out procedure with the vacuum oven was successful and should be carried on in future experiments. Additionally no signs of delamination or separation of the foils composite are seen.

The foils were however subject to a plastic mechanical deformation. Figures 6.5 and 6.6 show the test foils deformation of the low-CTE and the 2-polymer processes, respectively, according to the test period: 2, 3 and 6 weeks (right to left).

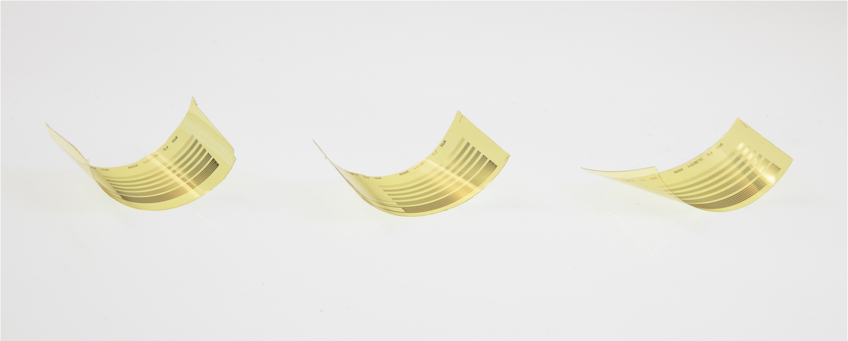

Figure 6.5: Test foils deformation of the low-CTE process

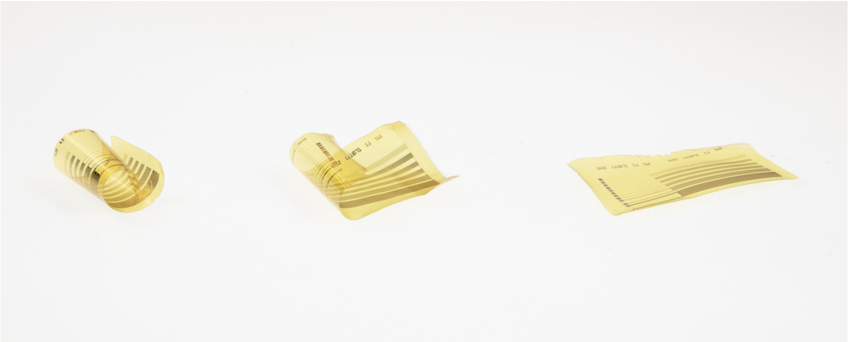

Figure 6.6: Test foils deformation of the 2-polymer process

As can be seen from Figures 6.5 and 6.6 and confirmed by the comparison of the 6-week result in Figure 6.7, the low-CTE process is distinctly more stable. In contrast, the test foils of the 2-polymer process are heavily deformed, which leads to challenges regarding handling and measurements. This is the first sign of the weak compatibility between the 2-polymer process and the battery electrolyte.

6.5.2 Electrical measurements

The electrical measurements of the test foils confirm the results of the optical examination. The foils of the low-CTE process, which were minimally deformed even after 6 weeks, show a stable resistance value when measuring their metal line structures. The conduction of electrical measurements of the resistance was possible in 7 out of 8 foils using the 4-wire-measurement method.

Figure 6.8 shows the averaged measured values of the resistance of all metal structures on the measured foils depending on the width of the metal structures and the test period.

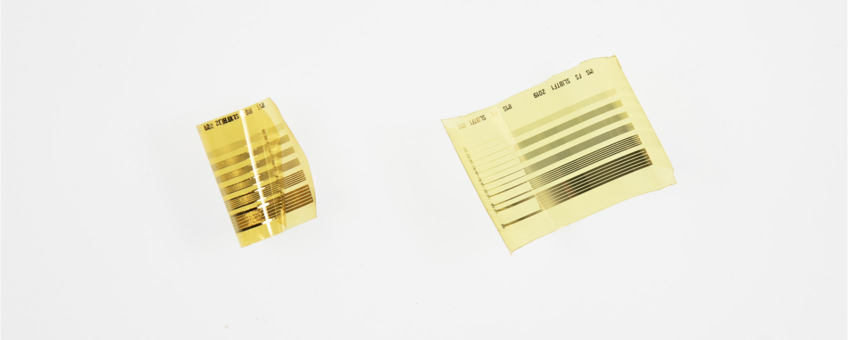

Figure 6.7: Comparison of the 6-week result for both processes (low-CTE process right, 2-polymer process left)

The resistance values are constant throughout the different periods and comparable with the pre-measurement values.

However, the test foils of the 2-polymer process had a plastic deformation which damaged the metal structures, so that electrical measurements in only 2 out of 8 foils were possible. These 2 foils had a test period of a single week. Table 6.2 show the averaged resistance values of the metal structures on these 2 foils, which have remained in the same order of magnitude compared to the pre-measurement. Because of the low number of undamaged test foils, no statistical evaluation can be done. The remaining foils (damaged, 6 out 8) showed resistance values in the MΩ-range, which indicates a rupture in the electric connection (OPEN-state) and a plastic damage of the metal lines.

It was not always possible during the experiments to avoid the direct contact of the open pads with the electrolyte solutions. The chosen metal is considered to be compliant with the chemical solution, since the solution is commercially delivered and stored in Al containers. Therefore, either Al or AlSiCu is chosen as base metal for the interconnections. However, it still cannot be excluded that the direct contact might have lead to an easier intrusion of the solution into the internal layers of the foil compound and a therefore to a higher moisture intake and to the damaging of the foils.

Table 6.2: Measured resistance values for the 2-polymer after 1 week

Metal line width (in µm)	Resistance value (in Ω)	
	pre-measurement	After 1 week
200	12	12
100	28	24
50	63	62
25	217	214
20	347	342
10	731	722

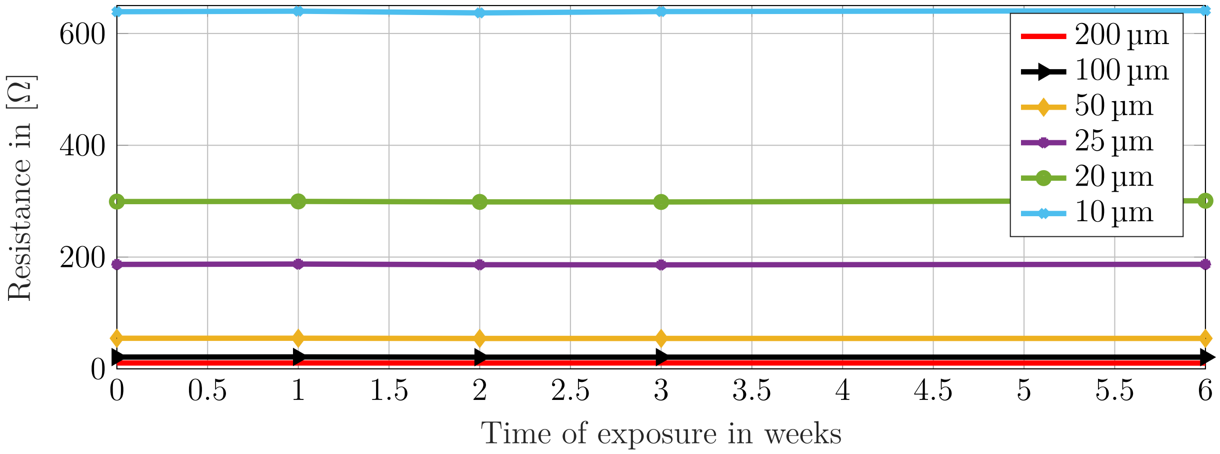

Figure 6.8: Resistance values comparison of different metal structures widths for the low-CTE process

6.6 Conclusions

The compatibility between a LiB electrolyte of the type 50:50 EC/DMC and 1.0 mol $LiPF_6$ and test foils fabricated according to the CFP technology was tested. Test foils were fabricated according to two different process versions and stored with the electrolyte solution in enclosed containers for different test periods. The test foils contain metal structures of different widths. The electrical resistance of these structures are measured before and after the experiments and compared. It was concluded that the process version low-CTE is more stable and has a better compatibility. The mechanical deformation of the tested foils was minimal and their electrical measurements were in the same range as the premasurement values.

Although these findings point into a clear direction, further investigations are therefore needed in order to have a more solid packaging system. A method should be developed to simulated an accelerated aging process. Otherwise, the measurement time would be too long (> months).

Next steps can also include the enclosing and exposure of the test foils to different temperature profiles, to imitate more realistic conditions. It is also important to test for longer periods or simulate an aging mechanism, again using temperature.

Another important aspect is to test foil systems with embedded active chips. The main goal being a complete integration of the CSC functionalities on a chip and its embedding in CFP foil system.

Chapter 7

Conclusions and Outlook

Lithium-ion batteries (LiB) are currently the preferred choice for use in Electric Vehicles and Hybrid Electric Vehicles thanks to their high energy and high power capabilities. Other available battery technologies are not competitive in technical and commercial terms. However, the LiB technology is still not considered safe. Several risky situations and abuse scenarios caused by external stimuli (all probable during application) can lead to considerable damages.

Several approaches at different design and use stages can be applied to tackle the matter of LiB cells safety. This work chooses to introduce smartness at cell level during the design, manufacturing, and application stages in order to increase the intrinsic safety of the cell by means of an integrated monitoring system, a Cell Supervisory Circuit (CSC), into the cell housing. A Smart-Lithium-ion battery (Smart-LiB) system is a Lithium-ion cell with a built-in CSC inside. Aside from the successful integration, the communication protocol used between the cells and the Battery Management System is another novelty of the work.

The Smart-LiB system, with its different hardware and software components, as well as a proof-of-concept were presented in Chapter 3. Chapters 4 and 5 propose enhancements of the sensors functionalities of the Smart-LiB system. Chapter 6 evaluates a packaging possibility for a future version of the Smart-LiB system.

In summary, a successful proof-of-concept for the Smart-Lithium-ion battery system was presented in this work. The concept, design and implementation steps were presented. Conclusions regarding successes and failures as well as outlooks and improvements implementation possibilities to the system are presented in this final chapter in a categorized manner.

7.1 Regarding communication

Conclusions

A main novelty of this work is the use of the Infrared optical communication protocol, which is, to the best of our knowledge, unreported in the literature so far. Not loading the battery and, therefore, the complete system with additional cabling in a construct where the weight of the whole Electric Vehicle plays an important role represents the main advantage of the technique. The metal housing of the battery and of the vehicle in general offers the advantage of additional reflections of the light signal and therefore of better transmission probabilities. In addition, the established IrDA communication protocol offers the advantage of using Original Equipment Manufacturer parts, which are already compatible with the standard and available on the market.

Outlook

The IR communication protocol used in this work would benefit from transmitting and receiver diodes with higher power capabilities, so that the optical transmission channels do not exclusively rely on the metallic battery module housing to support the reflection of the optical signals. In addition, opening a viewing window in the cell housing without causing leak tightness damages was one of the main challenges. Although this challenge was successfully solved, the possibility of implementing the IR emitting and photodiodes outside of the housing and merely connecting them to the CSC inside the cell should be explored.

7.2 Regarding system reliability

Conclusions

The encryption of data at battery cell level as well as the deterministic cell identification is possible and was implemented in the Smart-LiB system. Since the decryption mechanism is only available at the commanding unit (Part of the Battery Management System), this excludes the possibility of retrieving relevant information when data packages land in the hands of a third party. Currently, OEM EEPROM memory elements are used to save the formation data of the cell. They can save up to several days of measurement data.

Outlook

The functionality of the EEPROM memory elements can be extended to meet the industry standard by saving other cell manufacturing data, process parameters, cell identification model, as well as look-up tables, and first-level data analysis tools.

7.3 Regarding the algorithm and the system architecture

Conclusions

The CSC consists of a digital processing unit (a microprocessor), EEPROM memory elements, sensors and an IR communication interface. This CSC was successfully integrated in 2 chemically active test cells during the manufacturing phase. Data of the formation cycle were successfully recorded and extracted. The CSC communicates with an external commanding unit (part of the BMS) through the IR communication interface. Its algorithm is programmed to record formation data, read, and process sensor data as well as BMS commands.

Some of the algorithm drawbacks include the risk of data loss as well as inflexibility. In fact, the data logging mode restarts with every cycle of formation, mistakenly treating it as a new formation phase, which leads to data loss of the previous phases.

An interrupt mode is not available and makes therefore the algorithm inflexible. The algorithm is namely stuck in any given phase. It only leaves dependently on a previously set condition (e.g. reaching of a plateau). An interaction possibility with an external user is currently not implemented.

A sleep mode is also not activated. Since the CSC is supplied by the Lithium-ion cell itself, this leads to a continuous discharge of the cell. A deep enough discharge empties the cell and causes the restart of the recording of the formation process when it is charged again.

It was only possible to see these drawbacks in retrospect after implementation of the complete system and the analysis of the extracted data.

Outlook

The risk of data loss can be bypassed by implementing a simple flag of the last used memory case. The new measurement results (of the new formation cycles) should then be saved at the next available case instead of overwriting old data sets. The analysis of the extracted data can afterwards, based on the time stamp, determine whether some data sets are redundant.

Sleep and interruption modes are available at the microcontroller level. Therefore, by making use of these options, the integration of these user interference mechanisms as energy saving techniques in future algorithm versions can easily be implemented.

7.4 Regarding sensors and battery cell state

Conclusions

Sensors are necessary to the assessment of any battery cell state. Sensors of physical qunatities (voltage, temperature, pressure) as well as of battery-related quantities (State of Charge, State of Health). The proof-of-concept for the Smart-LiB system included Open Circuit Voltage and temperature sensors. The successfully recorded measurements of voltage and temperature values during the formation phase by the CSC were conform to the expected levels. Chapter 4 presents an alternative temperature sensor which can be positioned as a chip-on-foil. Chapter 5 reports on the design of a SoH sensor for LiB cells.

Outlook

The CMOS temperature sensor designed in this work (Chapter 4) has a similar accuracy to the commercially acquired Pt-100 used in the proof-of-concept (Chapter 3). A design effort can be invested in order to achieve a much higher accuracy. The trade-off faced will be between the practicability of the sensor form for integration as close as possible to the electrodes active area (chip in/on foil vs. resistor with cables) and the acceptable error tolerance of the temperature measurement.

More design effort needs to be put to improve the accuracy of the SoH sensor. Its further integration on-chip would additionally require a GaN or power CMOS technology node but would enhance the overall integrability of the monitoring system within even smaller cell housings.

Moreover, more sensors (of these and other physical quantities) are beneficial to the Smart-LiB system and for a more precise estimation of the battery state at different stages, e.g. a skin of temperature sensors as presented in Subsection 3.2.1.3, and a pressure sensor as in [124]. The necessary structures for the realization of such sensors were presented in Chapter 6.

7.5 Regarding packaging and system integration

Conclusions

Chapter 6 reported on an experiment investigating the compatibility of a packaging system (the CFP technique) with the battery electrolyte. One process version (the low-CTE process) showed a better resilience with the used electrolyte after 6 weeks. The mechanical deformation of the tested foils was namely minimal. In addition, the electrical measurements of the metal lines resistances were in the same range as the pre-measurement values.

Outlook

More tests with longer test periods as well as the exposure of the test foils to different temperature profiles are required for more conclusive comments about the compatibility of the foils with the electrolyte. A further improvement of the packaging technique can include a foil which has already been proven to be compatible and usable inside the LiB cell, namely the aluminum compound pouch foil used for partial sealing of pouch cells [47] (See Subsection 2.2.1).

7.6 Regarding mechanical handling and future system

Conclusions

After of the modification of the dimensions of the cell because the integration of the CSC, and although the welding process was effective, the yield of sealed battery cells was low (2 cells out of 23). This is due to the currently still necessary manual rework, which causes capacity loss and makes automation impossible. Despite a successful proof-of-concept, further tests to demonstrate the system feasibility with an automation plan are needed in order to be conclusive.

Outlook

The need to reduce the dimensions is therefore crucial for the Smart-LiB system. Integrating the functionalities available on the CSC on a chip solution enables a better mechanical handling and thermal management. Since the components can only be realized on different technology nodes (GaN or power CMOS for SoH, a II-VI or III-V semiconductor technology for IR communication), a flexible designed system of interconnected OTS elements and designed chips on a thin substrate can be realized.

7.7 Regarding reproducibility and manufacturability of the system

Conclusions

Although presenting a successful proof-of-concept, this work lacks an assessment of the reproducibility and the manufacturability of the Cell Supervisory Circuit and the Smart-LiB system. In fact, since the only two active cells with a functioning CSC were produced only thanks to a manual rework of the welding mechanism, no statement can be made regarding the complexity level of the reproducing these results under a semi- or fully automated process.

Outlook

For the CSC and the Smart-LiB system in general to be adopted as a product, the adaptation to all of the system components and assembly steps to an industry-friendly version are necessary. These include:

- the integration (to the most possible extent) of all (current and future) CSC components: Temperature, pressure and voltage sensors, and the communication interface. This will also lead to a size reduction and therefore to a reduction of the caused energy density losses.
- the automation of the assembly procedure of the complete circuit on its (flexible) PCB
- the choice of the packaging solution by either further testing and adaptation of the CFP technology, or the selection of a material that was already proven to be industrially fit and to protect from the agressive electrolyte, namely the aluminum compound pouch foil used for partial sealing of pouch cells [47] (See Subsection 2.2.1).
- the automation of the integration process of the CSC inside the housing of the cell, including the cabling step, as well as of the mechanical handling and welding procedure of the LiB cell.

These adaptations, correlated with a higher production volume are necessary for an investment. Otherwise, the additional costs caused by the CSC will not compensated for. In fact, the adaptations to accommodate for the Smart-LiB concept would be acceptable, from an industrial standard, if they cause a maximum of 1 € additionally per cell. The cells themselves (used in this work's demonstrator) cost around 50 €.

Currently, the costs of the CSC, as presented in Chapter 3, are between 10 and 15 €. This is not accounting for the additions from Chapters 4 to 6. This also does not account neither for the changes in the manufacturing process, nor for losses in the energy density of the cell caused by the insertion of the CSC. At these rates, the concept is simply not profitable.

Bibliography

[1] V. Handke, M. Knoll, W. Jörß, C. Kamburow, and T. Wehnert. *Energiespeicher - Stand und Perspektiven Themenfeld 3: Forschung und Entwicklung - Internationale Einordnung In: Oertel, D., Energiespeicher - Stand und Perspektiven*, pages 121–136. Büro für Technikfolgen-Abschätzung beim Deutschen Bundestag (TAB), TAB-Arbeitsbericht Nr. 123, Feb. 2008.

[2] R. van Noorden. The rechargeable revolution: A better battery. *Nature*, 507(7490):26–28, 2014.

[3] A. Thielmann, A. Sauer, R. Isenmann, M. Wietschel, and P. Plötz. Produkt-Roadmap Lithium-Ionen-Batterien 2030. ISI Karlsruhe, 2012. [Online] Last accessed: December 8, 2019.

[4] A. Thielmann, R. Isenmann, and M. Wietschel. Technologie-Roadmap Lithium-Ionen-Batterien 2030. ISI Karlsruhe, 2010. [Online] Last accessed: December 8, 2019.

[5] I. Buchmann. *Batteries in a portable world: A handbook on rechargeable batteries for non-engineers.* Cadex Electronics, Vancouver, 4. edition edition, 2016.

[6] Bundesministerium für Bildung und Forschung. Elektromobilität - das Auto neu denken: Hightech- Strategie. Bonn, 2013. [Online] Last accessed: December 9, 2019.

[7] Die Bundesregierung. Regierungsprogramm Elektromobilität. May 2011. [Online] Last accessed: December 14, 2019.

[8] Bundesministerium für Verkehr und digitale Infrastruktur. kompakt^2 Elektromobilität. Feb 2017. [Online] Last accessed: December 11, 2019.

[9] Wie Deutschland zum Leitanbieter für Elektromobilität werden kann - status quo – herausforderungen – offene frage. *acatech - Deutsche Akademie der Technikwissenschaften*, Vol. 6, 2010. [Online] Last accessed: December 11, 2019.

[10] Bundesministerium für Verkehr ,Bau und Stadtentwicklung. Elektromobilität – Deutschland als Leitmarkt und Leitanbieter. *Energie für Deutschland*, Jun. 2011. [Online] Last accessed: December 11, 2019.

[11] E. Rahimzei, K. Sann, and V. Moritz. Kompendium: Li-Ionen-Batterien, Grundlagen, Bewertungskriterien, Gesetze und Normen. *im BMWi Förderprogramm IKT für Elektromobilität II: Smart Car - Smart Grid - Smart Traffic*, 2012. [Online] Last accessed: December 14, 2019.

[12] P. Keil. *Aging of Lithium-Ion Batteries in Electric Vehicles.* Dissertation, Technische Universität München, München, 2017.

[13] Dr. Pavol Bauer, ir. A.E. Hoekstra, ir. G.R. Chandra Mouli, and Prof dr. ir. M. Wagemaker. *Electric Cars: Technology.* Lecture, TU Delft (Delft University of Technology) OpenCourseWare, 2018. [Online]. Last accessed: December 14, 2019.

[14] V. Srinivasan, D. Hafemeister, B. Levi, M. Levine, and P. Schwartz. Batteries for vehicular applications. In *AIP Conference Proceedings.* AIP, 2008.

[15] M. M. Kabir and D. E. Demirocak. Degradation mechanisms in Li-ion batteries: a state-of-the-art review. *International Journal of Energy Research*, 41(14):1963–1986, apr 2017.

[16] I. Tsiropoulos, D. Tarvydas, and N. Lebedeva. Li-ion batteries for mobility and stationary storage applications - Scenarios for costs and market growth. *Science for Policy report by the Joint Research Centre (JRC)*, 2018. [Online] Last accessed: September 10, 2020.

[17] Bundesministerium für Bildung und Forschung (BMBF), Nationale Plattform Elektromobilität (NPE). *Zweiter Bericht der Nationalen Plattform Elektromobilität.* Gemeinsame Geschäftsstelle Elektromobilität der Bundesregierung (GGEMO), 2011. [Online], Last accessed: December 16, 2019.

[18] Bundesministerium für Bildung und Forschung und Nationale Plattform Elektromobilität. *Fortschrittsbericht 2014 - Bilanz der Marktvorbereitung.* Gemeinsame Geschäftsstelle Elektromobilität der Bundesregierung, 2014. [Online], Last accessed: December 16, 2019.

[19] Bundesministerium für Bildung und Forschung (BMBF), Nationale Plattform Elektromobilität (NPE). *Fortschrittsbericht 2018 - Markthochlaufphase.* Gemeinsame Geschäftsstelle Elektromobilität der Bundesregierung (GGEMO), 2018. [Online], Last accessed: December 16, 2019.

[20] M. Kultgen and G. Zimmer. Monitoring-IC im Batteriemanagementsystem - Jede Zelle im Blick. *Elektronik Informationen*, Mai 2016. [Online] Last accessed: August 3, 2017.

[21] A. Otto, S. Rzepka, T. Mager, B. Michel, C. Lanciotti, T. Günther, and O. Kanoun. Battery Management Network for Fully Electrical Vehicles Featuring Smart Systems at Cell and Pack Level. In *Advanced Microsystems for Automotive Applications (AMAA)*, pages 3–14. Springer, 2012. [Online] Last accessed August 4, 2017.

[22] F. Saidani, F. X. Hutter, W. Selinger, Z. Yu, and J. N. Burghartz. A Lithium-ion battery demonstrator for HEV applications featuring a smart system at cell level. In *2017 IEEE International Systems Engineering Symposium (ISSE)*, pages 1–5, Oct 2017.

[23] Programm „IKT 2020 – Forschung für Innovationen“ des BMBF. IntLiIon: Intelligent Data Bus Concepts for Lithium-Ion Batteries in Electric and Hybrid Vehicles, 2013-2015. [Online] Last accessed April 19, 2020.

[24] I. Ouannes, P. Nickel, and K. Dostert. Cell-wise monitoring of Lithium-ion batteries for automotive traction applications by using power line communication: battery modeling and channel characterization. In *18th IEEE International Symposium on Power Line Communications and Its Applications (ISPLC)*, pages 24–29, March 2014.

[25] I. Ouannes, P. Nickel, J. Bernius, and K. Dostert. Physical Layer Performance Analysis of Power Line Communication (PLC) applied for Cell-Wise Monitoring of Automotive Lithium-Ion Batteries. In *18th International OFDM Workshop 2014 (InOWo'14)*, pages 1–8, Aug 2014.

[26] I. Ouannes, P. Nickel, O. Opalko, and K. Dostert. Monitoring of Lithium-Ion Batteries in Electric/Hybrid Vehicles using Power Line Communication. In *AmE 2015 - Automotive meets Electronics, 6. GMM-Fachtagung*. VDE-Verl., Berlin, Feb 2015.

[27] SMART-LIC Consortium CORDIS (European Comission). Smart and Compact Battery Management System Module for Integration into Lithium-Ion Cell for Fully Electric Vehicles, 2012. [Online] Last accessed April 19, 2020.

[28] F. Schreiner, G. Pelz, M. Rose, Ö. Karaca, G. Ruhl, K. Elian, J. Kirscher, and W. Maurer. Schlussbericht des Infineon Projektes "Sensorik, Simulation und Digitaler Batteriepass für sichere Lithium-Ionen Batterien" im Rahmen des Verbundvorhabens SafeBatt "Aktive und passive Maßnahmen für eigensichere Lithium-Ionen Batterien" : Berichtszeitraum: 01.07.2012-31.12.2015.

[29] Bundesministerium für Bildung und Forschung (BMBF), Nationale Plattform Elektromobilität (NPE). *Fortschrittsbericht der Nationalen Plattform Elektromobilität (Dritter Bericht).* Gemeinsame Geschäftsstelle Elektromobilität der Bundesregierung (GGEMO), 2012. [Online], Last accessed: December 16, 2019.

[30] W. Maurer, M. Rose, D. Hoffmann, and A. Reinfeld. Monitoring and Improving the Safety Behavior of Lithium-Ion Battery Cells by Advanced Sensor-, Test-, and Simulation Capabilities. In *Advanced Automotive Battery Conference (AABC Europe)*, 2015.

[31] E. Worthman. Recharging the Battery. *Semiconductor Engineering*, August 2015. [Online] Last accessed: April 25, 2017.

[32] F. Saidani, F. X. Hutter, W. Selinger, S. Roessler, W. Braunwarth, and J. Burghartz. An integrated electronic circuit for decentralized monitoring of Lithium-ion battery cells. In *MikroSystemTechnik 2017; Congress*, pages 1–4, Oct 2017.

[33] Jun Liu, Zhenan Bao, Yi Cui, Eric J. Dufek, John B. Goodenough, Peter Khalifah, Qiuyan Li, Bor Yann Liaw, Ping Liu, Arumugam Manthiram, Y. Shirley Meng, Venkat R. Subramanian, Michael F. Toney, Vilayanur V. Viswanathan, M. Stanley Whittingham, Jie Xiao, Wu Xu, Jihui Yang, Xiao-Qing Yang, and Ji-Guang Zhang. Pathways for practical high-energy long-cycling Lithium metal batteries. *Nature Energy*, 4(3):180–186, feb 2019.

[34] U. Tröltzsch, O. Kanoun, and H.-R. Tränkler. Characterizing aging effects of Lithium ion batteries by impedance spectroscopy. *Electrochimica Acta*, 51(8):1664–1672, 2006.

[35] N. Kheirabadi and A. Shafiekhani. Graphene/Li-ion battery. *Journal of Applied Physics*, 112(12):124323, 2012.

[36] The European Association for Advanced Rechargeable Batteries. Safety of Lithium-ion batteries. *RECHARGE Advanced Rechargeable Batteries & Lithium Batteries Association*, 2013. [Online] Last accessed: December 21, 2019.

[37] H. Heimes, A. Kampker, A. vom Hemdt, C. Schön, S. Michaelis, and E. Rahimzei. *Produktion einer All-Solid-State-Batteriezelle.* PEM der RWTH Aachen University, Aachen, 1. Auflage edition, 2018.

[38] Theil, S. *Elektrolytalterung in Lithium-Ionen-Batterien.* Dissertation, Universität Ulm, Zentrum für Sonnenenergie- und Wasserstoff-Forschung, 2016.

[39] F. Saidani, F. X. Hutter, R.-G. Scurtu, W. Braunwarth, and J. N. Burghartz. Lithium-ion battery models: a comparative study and a model-based powerline communication. In *Advances in Radio Science*, pages 83–91. Copernicus GmbH, 2017.

[40] N. P. Lebedeva and L. Boon-Brett. Considerations on the Chemical Toxicity of Contemporary Li-Ion Battery Electrolytes and Their Components. *Journal of The Electrochemical Society*, 163(6):A821–A830, 2016.

[41] M.-T. von Srbik, M. Marinescu, R. F. Martinez-Botas, and G. J. Offera. A physically meaningful equivalent circuit network model of a Lithium-ion battery accounting for local electrochemical and thermal behaviour, variable double layer capacitance and degradation. *Journal of Power Sources*, 325:171–184, 2016.

[42] L. Kong, C. Li, J. Jiang, and M. Pecht. Li-Ion Battery Fire Hazards and Safety Strategies. *Energies*, 11(9):2191, 2018.

[43] J. P. Schmidt. *Verfahren zur Charakterisierung und Modellierung von Lithium-Ionen Zellen*, volume 25 of *Schriften des Instituts für Werkstoffe der Elektrotechnik, Karlsruher Institut für Technologie.* KIT Scientific Publishing, Karlsruhe, 2013.

[44] R. Rao, S. Vrudhula, and D. N. Rakhmatov. Battery modeling for energy-aware system design. *Computer*, 36(12):77–87, 2003.

[45] R. Schröder, M. Aydemir, and G. Seliger. Comparatively Assessing different Shapes of Lithium-ion Battery Cells. *Procedia Manufacturing*, 8:104–111, 2017.

[46] H. Heimes, A. Kampker, A. vom Hemdt, C. Schön, S. Michaelis, and E. Rahimzei. *Produktionsprozess einer Lithium-Ionen-Batteriezelle.* PEM der RWTH Aachen University, Aachen, 3. Auflage, revidierte Ausgabe edition, 2018.

[47] A. Schmidt, G. Topalov, and B. Oberschachtsiek. Entwicklung von Lithium-Ionen-Zellen für kleine Nutzfahrzeuge. *Zentrum für BrennstoffzellenTechnik (The fuel cell research center), Ministerium für Wirtschaft, Energie, Industrie, Mittelstand und Handwerk des Landes Nordrhein-Westfalen*, March 2016. [Online] Last accessed: December 24, 2019.

[48] A. Wang, S. Kadam, H. Li, S. Shi, and Y. Qi. Review on modeling of the anode solid electrolyte interphase (SEI) for Lithium-ion batteries. *npj Computational Materials*, 4(1):15, 2018.

[49] H. Heimes, A. Kampker, S. Wessel, M. Kehrer, S. Michaelis, and E. Rahimzei. *Montageprozess eines Batteriemoduls und -packs*. PEM der RWTH Aachen University, Aachen, 3. Auflage, revidierte Ausgabe edition, 2018.

[50] H. Rahimi Eichi, U. Ojha, F. Baronti, and M.-Y. Chow. Battery Management System: An Overview of Its Application in the Smart Grid and Electric Vehicles. *Industrial Electronics Magazine, IEEE*, 7:4–16, 06 2013.

[51] E. Cabrera-Castillo, F. Niedermeier, and A. Jossen. Calculation of the state of safety (SOS) for lithium ion batteries. *Journal of Power Sources*, 324:509–520, Aug. 2016.

[52] D. H. Doughty and C. C. Crafts. FreedomCAR : electrical energy storage system abuse test manual for electric and hybrid electric vehicle applications. *Office of Scientific and Technical Information (OSTI)*, 2006.

[53] J. Vetter, P. Novák, M. R. Wagner, C. Veit, K.-C. Möller, J. O. Besenhard, M. Winter, M. Wohlfahrt-Mehrens, C. Vogler, and A. Hammouche. Ageing mechanisms in Lithium-ion batteries. *Journal of Power Sources*, 147(1-2):269–281, 2005.

[54] K. B. Hatzell, A. Sharma, and H. K. Fathy. A survey of long-term health modeling, estimation, and control of Lithium-ion batteries: Challenges and opportunities. In *2012 American Control Conference (ACC)*, pages 584–591, June 2012.

[55] J. Meng, G. Luo, M. Ricco, M. Swierczynski, D.-I. Stroe, and R. Teodorescu. Overview of Lithium-Ion Battery Modeling Methods for State-of-Charge Estimation in Electrical Vehicles. *Applied Sciences*, 8(5):659, 2018.

[56] J. Yu. State-of-Health Monitoring and Prediction of Lithium-Ion Battery Using Probabilistic Indication and State-Space Model. *IEEE Transactions on Instrumentation and Measurement*, 64(11):2937–2949, Nov 2015.

[57] T. Wu, M. Wang, Q. Xiao, and X. Wang. The SOC Estimation of Power Li-Ion Battery Based on ANFIS Model. *Smart Grid and Renewable Energy*, 3(1):51–55, 2012.

[58] P. L. Moss, G. Au, E. J. Plichta, and J. P. Zheng. An electrical circuit for modeling the dynamic response of li-ion polymer batteries. *Journal of The Electrochemical Society*, 155(12):A986, 2008.

[59] J. N. Burghartz, E. Angelopoulos, W. Appel, S. Endler, S. Ferwana, C. Harendt, H. Hassan, M.-U.and Rempp, H. Richter, and M. Zimmermann. Ultra-thin chips for flexible electronics. In *IEEE International Conference of Electron Devices and Solid-state Circuits*, pages 1–2, June 2013.

[60] Hassan, M.-U. *Ultra-Thin Chip embedding and interconnect technology for System-in-Foil applications.* Dissertation, Universität Stuttgart, 2017.

[61] M. Hassan, C. Schomburg, C. Harendt, E. Penteker, and J. N. Burghartz. Assembly and embedding of ultra-thin chips in polymers. In *Eurpoean Microelectronics Packaging Conference (EMPC)*, pages 1–6, Sep. 2013.

[62] Simscape Toolbox. *MATLAB Version 9.7 (R2019b), Simscape Version 4.7 (R2019b).* The MathWorks Inc., Natick, Massachusetts, 2019.

[63] J. R. Belt. Battery Test Manual For Plug-In Hybrid Electric Vehicles, Dec 2010.

[64] Sauerteig, D. *Implementierung und Parametrierung eines physikalischen Simulationsmodells einer Lithium-Ionen Zelle zur Analyse elektrochemisch-mechanischer Wechselwirkungen.* Dissertation, Technische Universität Ilmenau, 2018.

[65] S. Goutam, J.-M. Timmermans, N. Omar, P. Van den Bossche, and J. Van Mierlo. Comparative Study of Surface Temperature Behavior of Commercial Li-Ion Pouch Cells of Different Chemistries and Capacities by Infrared Thermography. *Energies*, 8(8):1–18, August 2015.

[66] Intel Corporation. The Automotive-Grade Device Handbook. August 2019.

[67] J. Kunkelmann. Untersuchung des Brandverhaltens von Lithium-Ionen- und Lithium-Metall-Batterien in verschiedenen Anwendungen und Ableitung einsatztaktischer Empfehlungen. Technical report, Forschungsstelle für Brandschutztechnik, Karlsruhe, 2015.

[68] M. Murnane and A. Ghazel. A Closer Look at State of Charge (SOC) and State of Health (SOH) Estimation Techniques for Batteries. *Analog Devices*, 2017.

[69] Shehani Attanayaka, J.P. Karunadasa, and K T M U Hemapala. Estimation of State of Charge for Lithium-ion batteries - A Review. *AIMS Energy*, 7(2):186–210, 2019.

[70] Bohlen, O. S. *Impedance-based battery monitoring.* Dissertation, RWTH Aachen, 2008.

[71] Zong-You Hou, Pang-Yen Lou, and C. Wang. State of Charge, State of Health, and State of Function monitoring for EV BMS. In *2017 IEEE International Conference on Consumer Electronics (ICCE)*, pages 310–311, Jan 2017.

[72] Microchip Technology Inc. *PIC24FV16KM204 FAMILY, General Purpose, 16-Bit Flash Microcontrollers with XLP Technology Data Sheet*, 2013. Document Number: DS30003030B.

[73] MCC. *The MPLAB® Code Configurator graphical programming environment, integrated within the MPLAB X Integrated Development Environment.* Microchip Technology Inc.

[74] Burr-Brown products from Texas Instruments. *OPA237, OPA2237, OPA4237, Single-Supply Operational Amplifiers MicroAmplifier. Series.* SBOS057A - OCTOBER 1996 - REVISED FEBRUARY 2007.

[75] O. Opalko, D. Alonso, and K. Dostert. Measurements on Rogowski coils as coupling elements for power line communication in traction Lithium-ion batteries. In *2015 IEEE International Symposium on Power Line Communications and Its Applications (ISPLC)*, pages 29–34, 2015.

[76] O. Opalko, D. Alonso, and K. Dostert. Modeling of the power-line channel in automotive Li-ion batteries with Rogowski coils as coupling elements. In *2016 International Symposium on Power Line Communications and its Applications (ISPLC)*, pages 224–229. IEEE, 2016.

[77] Baker, Bonnie C. *Wireless Communication Using the IrDA Standard Protocol.* Microchip Technology, Inc., 2003. Analog Design Note ADN006.

[78] I. Miller, M. Beale, B. J. Donoghue, K. W. Lindstrom, and S. Williams. The IrDA Standards for High-Speed Infrared Communications. *Hewlett-Packard journal*, Feb 1998.

[79] Innovative Sensor Technology. *400°C Typenreihe Platinmesswiderstände mit Drahtanschlüssen.* Document reference DTP400-D2.2.indd.

[80] Bruce Trump. *Analog linearization of resistance temperature detectors.* Texas Instruments Incorporated, 2011.

[81] B. Fry and C. Reas. *Processing 3.* The Processing Foundation, Natick, Massachusetts, 2012-2016.

[82] J. Anders. *Integrated Interface Circuits.* Lecture, Universität Ulm, 2015.

[83] B. Razavi. The Bandgap Reference [A Circuit for All Seasons]. *IEEE Solid-State Circuits Magazine*, 8(3):9–12, 2016.

[84] K. Souri. *Energy-Efficient Smart Temperature Sensors in CMOS Technology.* Dissertation, Technische Universiteit Delft, 2016.

[85] E. Fred Schubert. *Light-Emitting Diodes.* Cambridge University Press, 2 edition, 2006.

[86] Michiel A. P. Pertijs, A. Bakker, and Johan H. Huijsing. A high-accuracy temperature sensor with second-order curvature correction and digital bus interface. *The 2001 IEEE International Symposium on Circuits and Systems (ISCAS)*, 1:368–371 vol. 1, 2001.

[87] P. Malcovati, F. Maloberti, C. Fiocchi, and M. Pruzzi. Curvature-compensated BiCMOS bandgap with 1-V supply voltage. *IEEE Journal of Solid-State Circuits*, 36(7):1076–1081, July 2001.

[88] X-FAB, Mixed Signal Foundry Experts. *XH018, 0.18 Micron Modular Analog Mixed HV Technology.* document release: 12.13.

[89] G.-M. Sung, Y.-T. Lai, and C.-L. Lu. CMOS Bandgap Reference and Current Reference with Simplified Start-Up Circuit. volume 2, December 2012.

[90] S. Hongprasit, W. Sa-Ngiamvibool, and A. Aurasopon. Design of bandgap core and startup circuits for all cmos bandgap voltage reference. *Przeglad Elektrotechniczny*, 88:277–280, 01 2012.

[91] H. Shrimali and V. Liberali. The start-up circuit for a low voltage bandgap reference. In *21st IEEE International Conference on Electronics, Circuits and Systems (ICECS)*, pages 92–95, Dec 2014.

[92] Aries Electronics, Bristol, PA 19007-6810 USA. *Series 55 Universal Zero-Insertion-Force DIP Test Socket.* Rev. 2.0.

[93] Vötsch Industrietechnik, Balingen-Frommern, Germany. *Temperature Test Chamber VT4002, VT4004, VT4007 Operating instructions*, 1996.

[94] Maxim Integrated. *DS18B20 Programmable Resolution 1-Wire Digital Thermometer*, 2019. 19-7487; Rev 6.

[95] LAUDA DR. R. WOBSER GMBH & CO. KG, Lauda-Koenigshofen, Germany. *Operating instructions PROLINE Low-temperature Thermostats with SmartCool System*, Aug. 2007. YACE0072/21.08.07.

[96] BASF SE. *GLYSANTIN G30 pink, ID Nr. 30279144/SDS-GEN-DE/DE*, Jan 2017. Version 3.4.

[97] P. Keil and A. Jossen. Aufbau und Parametrierung von Batteriemodellen. In *19. DESIGN & ELEKTRONIK - Entwicklerforum Batterien & Ladekonzepte*, 2012. [Online] Last accessed: August 2, 2017.

[98] J. L. Jespersen, A. E. Tønnesen, K. Nørregaard, L. Overgaard, and F. Elefsen. Capacity Measurements of Li-Ion Batteries using AC Impedance Spectroscopy. *World Electric Vehicle Journal*, 3(1):127–133, 2009.

[99] Haifeng Dai, Bo Jiang, and Xuezhe Wei. Impedance Characterization and Modeling of Lithium-Ion Batteries Considering the Internal Temperature Gradient. *Energies*, 11(1):220, 2018.

[100] Bio-Logic Science Instruments, Seyssinet-Pariset, FRANCE. *How to measure the internal resistance of a battery using EIS ?*, Jan. 2017. EC-Lab Application Note Nr. 62.

[101] W. Waag, S. Käbitz, and D. U. Sauer. Experimental investigation of the Lithium-ion battery impedance characteristic at various conditions and aging states and its influence on the application. *Applied Energy*, 102:885–897, 2013.

[102] Gamry Instruments, Inc. *Application Note: Basics of Electrochemical Impedance Spectroscopy*, 2016. Rev. 1.0 11/9/2016.

[103] H.-G. Schweiger, O. Obeidi, O. Komesker, A. Raschke, M. Schiemann, C. Zehner, M. Gehnen, M. Keller, and P. Birke. Comparison of several methods for determining the internal resistance of Lithium ion cells. *Sensors (Basel, Switzerland)*, 10(6):5604–5625, 2010.

[104] T. Grandjean, J. Groenewald, A. McGordon, W. Widanage, and J. Marco. Accelerated Internal Resistance Measurements of Lithium-Ion Cells to Support Future End-of-Life Strategies for Electric Vehicles. *Batteries*, 4(4):49, 2018.

[105] A. Mangler, O. Kanoun, T. Günther, and T. Kuther. Wie sich der Alterungszustand von Akkus schnell bestimmen lässt, 2017. [Online] Last accessed June 22, 2020.

[106] M. Nawito, H. Richter, and J. N. Burghartz. Compact wide-range sinusoidal signal generator for in vivo impedance spectroscopy. In *2015 Conference on Design of Circuits and Integrated Systems (DCIS)*, pages 1–5, Nov 2015.

[107] Tröltzsch, U. *Modellbasierte Zustandsdiagnose von Gerätebatterien.* Dissertation, Univ. der Bundeswehr München, 2008.

[108] L. W. Yao and J. A. Aziz. Modeling of Lithium Ion battery with nonlinear transfer resistance. In *2011 IEEE Applied Power Electronics Colloquium (IAPEC)*, pages 104–109, April 2011.

[109] Test Specification for Li-Ion Battery Systems: Test Specification for Li-Ion Battery Systems for HEVs. Standard, Verband der Automobilindustrie (VDA), 2008.

[110] ISO 12405-2 - Electrically propelled road vehicles - Test specification for Lithium-ion traction battery packs and systems. Standard, International Organization for Standardization (ISO), 2012.

[111] Ruiz, V. and Di Persio, F. *Standards for the performance and durability assessment of electric vehicle batteries: Possible performance criteria for an Ecodesign Regulation*, volume 29371 of *EUR, Scientific and technical research series.* Publications Office of the European Union, Luxembourg, 2018.

[112] Nationale Plattform Elektromobilität (NPE). *The German Standardization Roadmap for Electromobility.* , Jan. 2012. Version 2, [Online], Last accessed: April 10, 2020.

[113] J. P. Christopherson. Battery Test Manual For Electric Vehicles, Jun 2015.

[114] Keystone Electronics. *THM Battery Holder 18650*, 2010. Drawing Nr. 1043.

[115] Vishay Foil Resistors. *Bulk Metal Foil Technology Precision Foil Power Surface Mount Resistors in TO-220 Configuration with TCR of ± ppm/°C, Tolerance of to ±0.01 % and Power Rating to 8W*, March 2010. Document Number: 63050.

[116] Transphorm Inc. *650V Cascode GaN FET in TO-247 - TP65H035WS*, June 2018. Version tp65h035w.1.

[117] IPC-2152 - Standard for Determining Current-Carrying Capacity in Printed Board Design released. Standard 1, Association Connecting Electronics Industries/ Institute for Printed Circuits (IPC), 2010.

[118] Texas Instruments. *Characteristics of Rechargeable Batteries*, 2011. Literature Number: SNVA533.

[119] Alfredo H. Saab and Shasta Thomas. Simplified Li+ Battery-Charger Testing. *Maxim's Engineering Journal*, 64:16–19, Dec 2008.

[120] F. Saidani, S. Ferwana, Z. Yu, A. U. Schmid, K. P. Birke, and J. N. Burghartz. Untersuchung der Kompatibilität eines folienbasierten ChipPackaging- Systems mit

einem Lithium-Ionen-Batterieelektrolyt. In *Elektronische Baugruppen und Leiterplatten - EBL 2020*. VDE-Verlag, 2020.

[121] M.-U. Hassan, J. Keck, H. Klauk, J. Kostelnik, Y. Mahsereci, S. Sailer, A. Schreivogel, T. Zaki, and J. N. Burghartz. Combining organic and printed electronics in Hybrid System in Foil (HySiF) based smart skin for robotic applications. In *European Microelectronics Packaging Conference (EMPC)*, pages 1–6, Sep. 2015.

[122] M. Braun Inertgas-Systeme GmbH. *LABstar INERT GAS GLOVEBOX WORKSTATION*, October 2019. BR04/V8/2019-10.

[123] BASF CORPORATION. *Safety Data Sheet Selectilyte LP40, 30566641/SDS-GEN-US/EN*, May 2016. Version 6.0.

[124] Vishay Precision Group – Micro-Measurements. *Precision Strain Gages and Sensors* . Document reference VMM-DB0103-1011.

[125] Kirchev, A. Chapter 20 - Battery Management and Battery Diagnostics. In Patrick T. Moseley and Jürgen Garche, editor, *Electrochemical Energy Storage for Renewable Sources and Grid Balancing*, pages 411 – 435. Elsevier, Amsterdam, 2015.

[126] P. Haan, R. Bianchetti, S. Rosser, and H. Frantz. *Szenarien der Elektromobilität in Deutschland. EBP-Hintergrundbericht.* EBP Schweiz AG, Zollikon, EBP Deutschland GmbH, Berlin, 20. April 2018.

Acknowledgments

I would like to acknowledge all those who supported me during my doctoral journey and contributed to the success of this work.

First of all, I deeply thank Prof. Dr.-Ing. Joachim Burghartz, director of IMS CHIPS, for giving me the opportunity to conduct the work at the institute in this research topic, and for his supervision and support.

I also thank Prof. Dr.-Ing. Kai Peter Birke, director of the Subject Field Electrical Energy Storage Systems at the Institute for Photovoltaics (IPV) for agreeing to be the co-examiner and for the technical support and fruitful discussions throughout the years of this work, as well as for enabling the technical collaboration with IMS CHIPS.

Also, many thanks to Mr. Franz X. Hutter, who has taught me a lot, to Dr. Zili Yu, for her mentoring and close supervision, and to Dr. Tarek Zaki, my supervisor during the early months of this work.

This work was partially funded by the Ministerium für Finanzen und Wirtschaft Baden-Württemberg within the framework of the research project "Smart-LiB". I acknowledge the financial support, as well as the technical support and collaboration of the project partners at the Zentrum für Sonnenenergie- und Wasserstoff-Forschung Baden-Württemberg (ZSW-BW).

Furthermore, I would like to thank all my colleagues at IMS CHIPS, for technical and operational assistance, or simply for making the workdays more enjoyable. I would like to especially name Dr. Muhammed Al-Shahed, Dr. Mourad Elsobky, Dr. Moustafa Nawito, Dr. Saleh Ferwana, Ir. Cor Scherjon, Dr. Christian Burwick, Dr. Harald Richter, Mr. Thomas Deuble, Mr. Wilhelm Selinger (may he rest in peace), Ms. Susanne Kehl, Ms. Astrid Hamald, Mr. Alexander Frank, Dr. Mahadi-Ul Hassan, and Dr. Yigit Mahsereci. I also thank Dr. Alexander Uwe Schmid from IPV for his valuable contribution to the electrolyte tests.

Finally, I owe my greatest gratitude to my family and friends.

Thank you to my parents and my sister. Their unconditional love and continuous support is the main reason I keep going forward. This work is dedicated to them.

Thank you to Meriem, my best friend throughout the years.

A deep thank you to my husband, Dr. Mohammed Alomari, who had to deal with a fair share of the ups and downs of my doctoral journey and nevertheless stood by me, with unfailing patience, wisdom and love, through every single one of them.

Fida Saidani
October 2021